SLAC-R-543
UC-414

SAW-TOOTH INSTABILITY STUDIES AT THE STANFORD LINEAR COLLIDER DAMPING RINGS[*]

Boris V. Podobedov

Stanford Linear Accelerator Center
Stanford University, Stanford, CA 94309

SLAC-Report-543
December 1999

Prepared for the Department of Energy
under contract number DE-AC03-76SF00515

---

[*] Ph.D. thesis, Stanford University, Stanford, CA

Abstract

Saw-tooth instability occurs during high current operation in the Stanford Linear Collider (SLC) damping rings. This instability is single bunch, and it can be cast as a longitudinal microwave instability. It is caused by the beam interaction with short range wakefields in the ring vacuum chamber. The saw-tooth instability manifests itself in the periodic blowup in quadrupole or higher moments in the longitudinal beam distribution.

Most of our instability studies have been experimental. Since the measurements of coherent particle motion within a short ultrarelativistic beam are largely unconventional we had to develop some original diagnostics. These includes, for example, the down-conversion of the high frequency (~10 GHz) broad-band beam position monitor (BPM) signals. We have also employed a state-of-the-art Hamamatsu streak camera that is capable of resolving the longitudinal beam distribution with sub-picosecond accuracy.

As a result of our streak camera experiments we have quantitatively described the phase space of unstable bunches. We have found the radial structure of the instability mode and established that it only displaces a few percent of the beam particles. In another series of experiments we have correlated the instability signals from the beams before the extraction from the damping rings with their trajectories in the linac downstream. This showed that the instability results in a significant transverse beam jitter in the linac which compromises the damping ring performance as an injector. In addition, we have studied the instability behavior under the broad range of stored beam parameters using both passive observation and driven excitation. These measurements revealed unexpected beam behavior significantly above the instability threshold. Finally, we performed several low current experiments to estimate the damping ring vacuum chamber impedance.

We also present some analytical results regarding the instability and compare them to the observations. In particular, these include the explanation of unequal sidebands in the spectrum of the BPM signal from unstable bunches. In addition, we have obtained several results regarding the instability onset criteria and proposed a new method of estimating the instability threshold based on the steady-state solution of the Fokker-Planck equation.

Acknowledgements

The research goals of this thesis could not have been accomplished without valuable contributions from many people. First of all I should like to thank my research adviser professor Robert Siemann whose intuition and gentle guidance were really the core for successful completion of every experiment. Bob has enormously contributed to my professional growth by introducing me to the fascinating subject of experimental beam physics. He converted me from someone with rather remote ideas on how to operate an oscilloscope to a person who is not afraid of taking on the most challenging experimental projects.

I am also extremely grateful to Sam Heifets who spent endless hours discussing with me the theoretical aspects of the saw-tooth instability, the problem that turned out to be unusually stubborn to explain.

I also appreciate the help from many people from Accelerator Research Departments A and B, and Accelerator Department at SLAC. I especially would like to thank Nan Phinney and Marc Ross for support of my experiments even when they were quite perpendicular to the most imminent SLC needs. In addition, Franz-Josef Decker, Patrick Krejcik, Doug McCormick, and Michiko Minty have been always interested in my research and have helped me to learn some of the aspects of the SLC hardware maze.

Along with my adviser Professors Alex Chao and Helmut Wiedemann have read my thesis and provided many valuable comments. I very much appreciate their contribution.

I also want to thank my fellow graduate students and postdocs for making my life at SLAC and Stanford much more interesting and productive. Special thanks are due to Robert Holtzapple who taught me how to operate the streak camera and to Dennis Palmer who has helped me in many different ways. I am also grateful to David Pritzkau who has patiently tolerated me as an

officemate for years and who was always there when I struggled with my English prose.

Finally I would like to thank my parents who have influenced my decision to become a physicist and my wife Svetlana who has unconditionally supported me throughout all these years. I am also grateful to Cheryl and Moira Goldie since without them I would have never applied to Stanford.

Contents

List of Tables

List of Figures

Chapter 1

Introduction

1.0 Storage rings

The subject of this thesis is particle dynamics in storage rings. A storage ring is a device used to hold a large number of relativistically moving charged particles for a relatively long time maintaining their energy constant. Conceptually, a storage ring is a donut-shaped vacuum pipe surrounded by magnets that bend particle trajectories around the pipe. Another set of magnets - so called quadrupoles, produce additional fields to focus particles in the direction transverse to their motion. Stored charge constantly loses its energy due to synchrotron radiation and some other processes. To make up for this loss, energy is supplied to the particles through the so-called RF cavities that produce electric field in the longitudinal direction. Another effect of RF cavities is that they force particles to bunch longitudinally. Therefore, in the coordinate frame comoving with the bunch a combination of quadrupoles and RF cavities provides focusing in all three spatial coordinates. This is why in that coordinate frame particle motion is similar to a 3D harmonic oscillator. The three frequencies of this oscillator normalized to the revolution frequency are usually called the tunes.

When a charged particle follows a fixed radius bend its radiation energy loss scales as the fourth power of the Lorentz factor $\gamma = E/mc^2$. This is why the dynamics of light particles like electrons and positrons (for which γ factor of a thousand and more is routinely achieved) is significantly affected by radiation. This is usually not the case for proton and other heavy particle storage rings. In other words, there is a major difference in storage ring dynamics for light and heavy particles which largely comes from the effects of synchrotron radiation. In this thesis we will only concentrate on electron and positron storage rings.

Electron storage rings have many diverse applications, and their number is still growing. Nevertheless one can talk about three major application areas. First, there are collider rings that hold counterpropagating beams (usually e+ and e-) and are used for high energy physics needs. This field studies fundamental laws of nature by observing the products of particle collisions. Second, there are light sources that utilize the synchrotron radiation emitted by electrons. Finally, there are preconditioners, like damping rings, accumulators etc. that temporarily store beams until they achieve certain properties before reinjecting them into another machine.

No matter what the purpose of a storage ring is, it is fair to say that beam intensity, beam quality and beam stability ultimately define the ring performance. Beam intensity is proportional to the total charge stored. The meaning of beam quality depends on the application, but generally it is inversely related to the total phase space volume occupied by a beam. Finally, beam stability characterizes how well given beam parameters can be maintained. For example, for collider rings the performance is characterized by the so-called luminosity which defines useful event rate for a given event cross section. It is well known that after the so-called beam-beam intensity limit is reached the luminosity is proportional to the ratio of the number of particles per bunch to the vertical amplitude oscillation function β^* in the interaction point. Furthermore, although β^* inversely depends on the focusing quadrupole strength in the interaction region, it cannot be made arbitrarily small. One of the lower limits is $\beta^* \approx \sigma$, where σ is the rms bunch length. Therefore, to achieve maximum luminosity one has to either increase the amount of charge in each bunch or reduce its length. Similarly, for the light source applications the brightness of the synchrotron radiation is proportional to the beam charge and inversely proportional to its transverse phase space volume. In addition, many user experiments require very short light pulse duration which directly translates into requirement for small bunch length. And, of course, for all applications beams must remain stable, so that their size and trajectory do not change in uncontrolled fashion.

To achieve higher performance considerable effort has been spent to increase intensity and reduce the beam size in storage rings. It is intuitively clear that one cannot infinitely increase particle phase-space density. Apart from engineering issues, for example radiation destroying the inner surface of the vacuum chamber, people encounter new physics problems. At certain space charge density particle interactions with either themselves or their environment causes beams to go unstable. They break into oscillations or blow up in size which often leads to rapid beam loss on the walls of the vacuum chamber. This is where the subject of beam dynamics enters into accelerator physics.

2.0 Beam dynamics and collective effects in storage rings

Beam behavior in storage rings is extremely diverse and this subject has accumulated considerable literature (e.g. [1]- [4], [30]). Below we will offer a simplistic classification of beam dynamics effects with the purpose of better defining the scope of this thesis.

Most beam dynamics effects could be divided into single particle (or incoherent) and collective phenomena. Incoherent effects can be explained by considering particle motion in external fields. One example is the so-called dynamic aperture effect where focusing nonlinearity limits the maximum amplitude of bounded motion for a single particle. This effect often shortens the beam lifetime in storage rings. Some of the incoherent effects lead to instabilities when a certain amplitude characteristic of the process grows exponentially with time. For example, beams usually become unstable if one of their transverse tunes or the longitudinal tune approaches an integer number. This is because sharp transitions of vacuum chamber as well as numerous end fields create a periodic force on a beam causing parametric instability.

In this thesis we will not consider incoherent phenomena but rather concentrate on collective effects. These effects cannot be described as a motion in external fields. Alternatively, in this case beam behavior is largely determined by the interaction between the beam particles. This interaction may be either direct or through third party, for example the residual ions in the vacuum chamber. Usually particles in a bunch are loosely correlated in position. This means that the motion of each particle is not strongly affected by its nearest neighbors (like it would be in a neutral gas) but rather it is governed by a large portion of the overall beam charge. Therefore, particles can move coherently i.e. their motion is correlated on a macroscopic level. This coherent motion may become unstable at certain conditions which are always intensity dependent. Such behavior of beams in storage rings is similar to that of plasmas in external fields. Similar to plasma physics a large variety of collective phenomena, usually deteriorating performance, was discovered in storage rings. The most dangerous of them are fast collective instabilities which may lead to the total beam loss during several revolutions if the beam intensity exceeds some threshold value.

Over the years there has been significant progress towards understanding, diagnosing and curing of coherent beam effects in storage rings. For example, the phenomenon to which M. Sands refers in 1970 as "... strange bunch-lengthening effect observed in many storage rings - which is, as yet, not understood" [1] is now known as "potential well distortion" and described in accelerator physics textbooks (e.g. [3], [4]). On the other hand, the general problem posed by collective effects is far from complete solution. This is in part due to constant push for higher intensities and shift to new parameter regimes and partly because of extreme complexity of collective beam physics.

Indeed, particles in a stored beam compose an open system - they can have energy and matter exchange with the environment. The behavior of such systems is described by non-equilibrium thermodynamics, which is still an actively developing field. It is known that open systems can have certain stable configurations that exhibit some spatial or temporal order and are different from the thermodynamic equilibrium. This generally requires that the systems are nonlinear and have some sort of a feedback mechanism. Both of these are true in a storage ring where large amplitude motion is nonlinear, and the feedback mechanism is created through the particle interaction with environment by means of wake forces. These forces make a stored beam system even more interesting for physicists because in the ultrarelativistic case they invalidate Newton's third law causing the system to become non-Hamiltonian.

The diagnostics of collective effects in storage rings also presents a challenge. Typical longitudinal beam size is on the order of a centimeter, and the transverse dimensions are several orders of magnitude smaller. The only way to nondestructively measure the bunch shape is to analyze the electromagnetic radiation emitted by the beam. This could be synchrotron radiation, electromagnetic waves induced on the walls of the vacuum chamber or, perhaps, the scattering of externally applied laser light. Beam sizes define the lower frequency limit of the detecting apparatus to be in the microwave range for the longitudinal to somewhere into the optical regime for the transverse. Detecting coherent oscillations in such a system generally means resolving certain time varying structure within a bunch. This puts even tougher conditions on electronics generally requiring fast (ps) data acquisition.

In present thesis we will focus solely on longitudinal effects largely ignoring the transverse beam dynamics. As it will be shown in Chapter 2 separate consideration of transverse and longitudinal motion is often appropriate.

One way to get around single beam collective effects is to split the bunch into many smaller ones. Many modern rings are utilizing this principle. For example, the SLAC PEP-II asymmetric B-factory is running with 1658 bunches in both electron and positron rings. The bunch spacing there is

1.26 m which is considerably longer than the rms bunch length of 1 cm and makes single bunch collective effects less important. Of course, at practically interesting intensities instead of dealing with single bunch phenomena people have to deal with bunch to bunch interactions. These interactions are also a collective effect; however, they are described by somewhat different physics than single bunch effects, and they will not be considered in this thesis. We should note that studying single beam collective effects is still important since it establishes the ultimate factors limiting the intensity. For instance, one of the future luminosity upgrades for the B-factory calls for running with beam currents a factor of three higher than the single bunch longitudinal instability threshold [5]. Clearly, thorough understanding of how to overcome this instability will be required. Another reason to study single bunch collective effects is that they still govern beam physics at some older storage rings, for example, in the damping rings of the Stanford Linear Collider.

3.0 Stanford Linear Collider

Experimental data for this thesis were taken in the Stanford Linear Collider (SLC), specifically in the electron and positron damping rings (NDR and SDR respectively)

The SLC was built for the purposes of high energy physics namely to test the predictions of the Standard Model of elementary particles and forces between them. More specifically, people study different aspects of the model analyzing the decay scenarios of Z^0 bosons. The Z^0 resonance occurs at 93 GeV, and to create this particle the SLC collides head-on electron and positron bunches of about half this energy. To achieve such energy electron and positron bunches are accelerated by RF electric fields in the same two mile long linear accelerator. Subsequently, they are separated into the arcs and then brought into collision in the interaction region which is surrounded by the SLD detector.

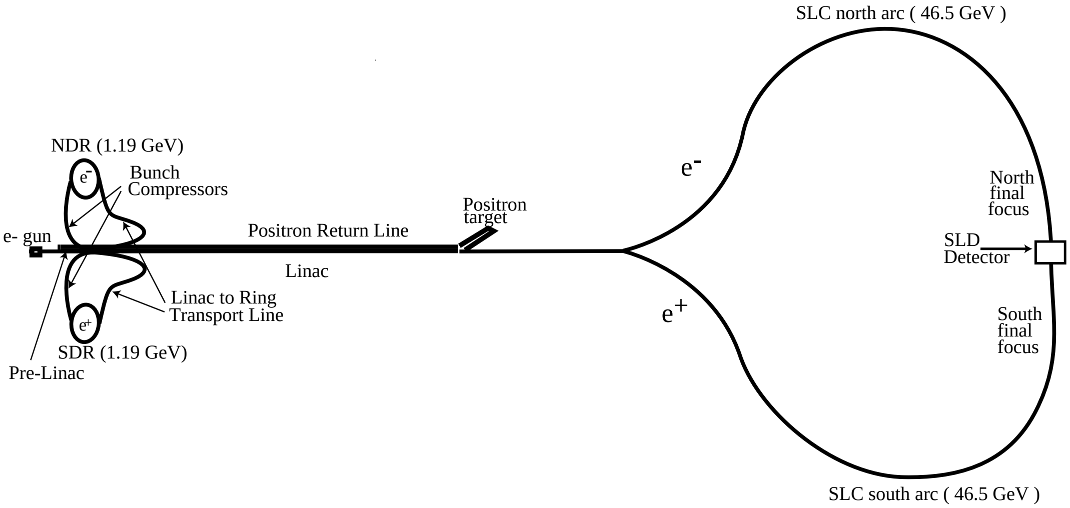

FIGURE 1. The layout of the Stanford Linear Collider (from [6]).

The layout of the facility is shown in Figure 1. Main components of the SLC are: 1) an electron gun to produce polarized electrons, 2) the preaccelerator - linear accelerator section to bring the energy to 1.19 GeV, 3) two damping rings - to increase the beam brightness, 4) the main linac - to accelerate electron and positron bunches to 46.5 GeV, 5) the positron target - to produce positrons, 6) the positron return line - to return positrons to the preaccelerator, 7) the arcs to bring copropogating beams into a head-on collision, 8) the final focus magnet system - to squeeze the bunches before the collision, 9) interaction region - this is where two bunches collide, 10) the SLD detector - to detect the collision products.

Nominal repetition rate of the SLC is 120 Hz. This is the rate electron bunches are produced by the gun and also the collision rate at the interaction region. The gun produces polarized electron bunches in pairs. One member of the pair (the production bunch) finally collides with a positron bunch. The other electron bunch is called the scavenger, and it is used to produce positrons at the target. The total charge in each bunch is roughly 6 nC which is about 4×10^{10} particles. To accelerate these bunches the SLC uses room temperature RF accelerating technology and operates at S-band frequency of

2856 MHz. The damping rings operate on the fourth subharmonic of this frequency. Both damping rings store two bunches each, and the injection cycle is defined by the repetition rate to be roughly 8.5 ms.

The SLC is a large and complex machine. To achieve design luminosity the SLC has to deliver high quality beams to the interaction region operating at the rate of 120 Hz. This would not be possible without a sophisticated control system. This system assembles large amounts of data from numerous diagnostic devices that measure beam characteristics (beam position monitors, wire scanners, ionization chambers etc.) as well as environmental parameters (for example, pressure and temperature sensors). Some of these data is analyzed on-line and used in feedback loops to optimize the luminosity. Other portions of data are archived for possible further analysis. The SLC control system is based on ALPHA cpu computer which uses VMS operating system and runs the main control program called SCP. For machine physics experiments this program is a major source of information on current beam parameters and machine conditions.

A complete set of SLC parameters can be found in [7]. Detailed discussion of the damping ring parameters as well as some aspects of the control system will take place in Chapter 3 of present thesis.

4.0 Scope of this thesis

In this thesis we will present experimental results on longitudinal particle dynamics in the SLC damping rings. For the most part we were interested in diagnostics and explanation of the high current phenomena called the sawtooth instability which can be classified as a single bunch longitudinal instability. We will also present the results of several low current experiments that were primarily carried out to characterize the damping ring vacuum chamber impedance and the RF system. Knowing these two factors is crucial for explaining the instability phenomenon. Some experimental results on how the instability affects performance of the SLC will also be presented. Finally, we will describe some theoretical models of the phenomena and compare them to the experimental results.

The rest of this thesis is organized as follows. Chapter 2 offers some background on single bunch collective effects including the saw-tooth instability observed in the SLC damping rings. Chapter 3 describes experimental apparatus and techniques (including some specifically developed for this thesis) that were used for this study. Original results are presented in Chapters 4 and 5 of the thesis. Chapter 4 describes experimental results while Chapter 5 is devoted to the theoretical side as well as to the interpretation of the experiments. Finally, summary and conclusions are offered in Chapter 6.

The experimental part of this thesis (Chapters 3 and 4) uses MKS units while CGS units are used elsewhere. If the units are not specified they should be assumed in CGS system. Also, to simplify the formulas normalized variables will be used extensively in Chapters 2 and 5. For example, the bunch length will be measured in units of natural bunch length. This will be further explained when needed.

Chapter 2

Single bunch longitudinal dynamics in storage rings

1.0 Single particle motion

This section includes a mainly qualitative description of the fundamentals of the single particle motion in storage rings. In our consideration we loosely follow [1].

1.1 Coordinate system

Storage rings are usually designed utilizing a concept of a closed orbit. It states that there exists a particle trajectory which closes on itself after one revolution. Furthermore, if a nominal energy particle is put on this trajectory at the right phase with respect to the ring RF system it will stay there indefinitely without on average loosing or gaining any energy. This particle is often called the synchronous particle. Its energy and revolution period will be referred to as E_0 and T_0. We will assume below that the closed orbit lies entirely in the horizontal plane which is true for most rings and simplifies the analysis of the kinematics.

It is convenient to introduce a coordinate system with respect to the synchronous particle. Longitudinal coordinate z is then defined so that a particle in front of a synchronous one has positive z. It should be noted that about half the accelerator physicists use the opposite sign convention, however, the consequences of this are rather trivial.

1.2 Small amplitude synchrotron oscillations

A particle with the energy slightly higher than nominal $E = E_0(1 + \delta)$, $\delta > 0$ will generally follow a trajectory different from a closed orbit. The period of this trajectory (which may be defined as the average value between the two consecutive passes through some azimuthal position in the ring) will be longer than T_0 because the magnets bend this particle's trajectory less. In the non-relativistic case this effect is offset by the $T \sim E^{1/2}$ dependence, which, however, becomes negligible when the velocity approaches c and weakly depends on the energy. To quantify this energy dependent orbit lengthening $\Delta L = \Delta L(\gamma)$ the momentum compaction parameter α is introduced so that

$$\frac{\Delta L}{cT_0} = (\alpha - \gamma^{-2})\delta. \qquad (2.1)$$

Momentum compaction factor is related to the ring optics and is usually a positive number on the order of ν_x^{-2}, where ν_x is the horizontal betatron tune. This typically makes the γ^{-2} term above negligible for the ultrarelativistic case of interest.

To compensate for the energy loss due to the synchrotron radiation beam particles are supplied with energy from RF cavities. For the synchronous particle the energy loss per turn U_0 equals the energy gain from the RF $e\hat{V}\cos(\varphi_0) = U_0$. Here we assumed a single RF cavity with a harmonically varying voltage with amplitude $\hat{V}$; φ_0 is called the synchronous phase. For an off-energy particle, which arrives at the cavity at a different phase, the above equation transforms to

$$\Delta\delta = \frac{e\hat{V}}{E_0}\cos\left(\varphi_0 - \omega_{RF}\frac{\Delta z}{c}\right), \qquad (2.2)$$

where ω_{RF} is the RF frequency. By definition of the closed orbit the synchronous particle must always come at the same phase φ_0 to the RF cavity. Therefore, the revolution frequency $\omega_0 \equiv 2\pi / T_0$ has to be a subharmonic of the RF frequency $\omega_0 = \omega_{RF} / h$, where integer number h is called the harmonic number.

Usually z and δ change on the time scale much longer than the revolution period. Hence, changes over the revolution period can be expressed in terms of the time derivatives of these quantities. Now, assuming small oscillations in z compared to the RF wavelength, we arrive to the equations of motion

$$\dot{z} = -\alpha \delta c, \tag{2.3}$$

$$\dot{\delta} = \frac{\omega_{s0}^2}{\alpha c} z, \tag{2.4}$$

where dot denotes the derivative with respect to time and the (zero current) synchrotron frequency has been introduced as

$$\omega_{s0} \equiv \omega_0 \sqrt{\frac{e h \alpha \hat{V} \sin(\varphi_0)}{2\pi E_0}}. \tag{2.5}$$

EQ 2.3 and EQ 2.4 describe pure harmonic motion where an off-energy particle oscillates in energy and position with respect to the synchronous particle. These oscillations continue forever because the system described by EQ 2.3 and EQ 2.4 is conservative. This is, of course, an approximation resulting from the fact that two important synchrotron radiation effects were neglected. These effects are the radiation power dependence on the particle energy and quantum excitation.

1.3 Radiation effects

An electron following a fixed radius curve radiates away energy in the form of the synchrotron radiation. The radiation power P_γ is given by (e.g. [1])

$$P_\gamma \equiv P_\gamma(E) = \frac{c C_\gamma}{2\pi} \frac{E^4}{R^2}, \tag{2.6}$$

where $C_\gamma \approx 8.85 \times 10^{-5}$ m×GeV^{-3}, E is the energy and R is the bend radius. EQ 2.4 was derived neglecting this energy loss dependence on particle energy. Accounting for it adds another term to the right hand side of EQ 2.2, namely $\frac{1}{E_0}(P_\gamma(E) - P_\gamma(E_0)) \approx \tilde{\gamma}_d \delta$ where $\tilde{\gamma}_d \equiv \langle \frac{\partial}{\partial E} P_\gamma(E) \rangle_{turn} \approx \frac{U_0}{E_0 T_0}$. Of course, a more rigorous derivation should account for variable magnetic field strength along the particle trajectory. Therefore, the damping constant $\tilde{\gamma}_d$ should include some integral measures of this field. Indeed, a more accurate expression for the damping constant reads [1]

$$\tilde{\gamma}_d = \frac{C_\gamma E_0^3}{4\pi T_0}(2I_2 + I_4), \tag{2.7}$$

where $I_2 \equiv \oint R(s)^{-2} ds$ and $I_4 \equiv \oint [1 + 2K(s)R(s)^2]\eta(s)R(s)^{-3} ds$. The integrals are taken around the closed orbit, $K(s)$ is proportional to the gradient of the magnetic field and $\eta(s)$ is the so-called horizontal dispersion function also related to the magnetic field strength along the trajectory. Usually the radiation damping is much slower than synchrotron oscillations $\tilde{\gamma}_d \ll \omega_{s0}$. Radiation damping term modifies EQ 2.4 to the form $\dot{\delta} = \frac{\omega_{s0}^2}{\alpha c} z - \tilde{\gamma}_d \delta$ therefore leading to gradual damping of synchrotron oscillations.

Radiation damping comes from purely classical properties of the synchrotron radiation. Quantum nature of the synchrotron radiation leads to another important effect called radiation excitation. Formally, this effect has not showed up so far because it was assumed above that radiation is being emitted continuously. This is not quite true. According to quantum physics radiative emission occurs in discrete quanta of energy $\hbar\omega$, where ω is the photon frequency. The frequency distribution of the synchrotron radiation is well known (e.g. [1])

$$\tilde{P}(\omega) = \frac{9\sqrt{3}}{8\pi}\frac{P_\gamma}{\omega_c^2}\omega\int_{\omega/\omega_c} K_{5/3}(\xi)\,d\xi, \tag{2.8}$$

where the critical frequency is defined as $\omega_c \equiv \frac{3}{2}c\gamma^3/R$ and $K_{5/3}$ is a modified Bessel function of the order $5/3$. Note that according to EQ 2.8 synchrotron radiation spectrum is peaked around ω_c and rapidly falls off for $\omega > \omega_c$. Also, in the ultrarelativistic case the critical frequency tends to be many orders of magnitude higher than the revolution frequency since the former scales as γ^3.

The moments of time when each photon is emitted are purely random and the emission can be considered instantaneous. Therefore, synchrotron radiation acts as a white noise source added to the system. This source creates the energy fluctuations with a standard deviation

$$\overline{\frac{d}{dt}\langle(\Delta E)^2\rangle} = \int(\bar{h}\omega)^2 P(\omega)\,d\omega = \frac{55}{24\sqrt{3}}\bar{h}\omega_c P_\gamma. \tag{2.9}$$

Hence, our system initially described by energy conserving equations EQ 2.3 and EQ 2.4 now includes a damping term and a white noise source $\xi(t)$ $\langle\tilde{\xi}(t)\rangle_t = 0$, $\langle\tilde{\xi}(t)\tilde{\xi}(t')\rangle_t = 2\delta(t-t')$, so that

$$\dot{z} = -\alpha\delta c \tag{2.10}$$

$$\dot{\delta} = \frac{\omega_{s0}^2}{\alpha c}z - \tilde{\gamma}_d\delta + \sqrt{D}\tilde{\xi}(t). \tag{2.11}$$

According to EQ 2.9 the diffusion coefficient D is given by

$$D \equiv \sqrt{\tilde{\gamma}_d\omega_{s0}}\delta_0 \tag{2.12}$$

Coupled first order differential equations with noise sources (as EQ 2.10 and EQ 2.11) are often called the Langevine equations and there are standard ways to analyze them (e.g. [21], [23]). What is commonly done is to introduce a particle distribution function in z and δ and transform this system to a Fokker-Planck equation. This equation will be discussed in detail in Section 3.0 of present chapter. For now let us simplify EQ 2.10 and EQ 2.11

further by introducing unitless variables. It is clear that the characteristic energy spread as well as the spread in z are defined by the balance of the radiation damping and quantum excitation. Simple dimensional analysis (or, amazingly Einstein's formula for Brownian motion and even Nyquist's theorem from electric circuits theory) gives this characteristic (natural) energy spread as

$$\delta_0 \equiv D/\tilde{\gamma}_d \tag{2.13}$$

related to the natural bunch length σ_0 as follows

$$\frac{\omega_{s0}\sigma_0}{c} \equiv |\alpha|\delta_0 . \tag{2.14}$$

Hence, it is convenient to introduce unitless variables that make the Langevine equations especially simple. If we choose

$$\tau \equiv \omega_{s0}t, \quad x \equiv \frac{z}{\sigma_0}, \quad p \equiv -\frac{\delta}{\delta_0}, \tag{2.15}$$

and redefine the damping constant $\gamma_d \equiv \omega_{s0}\tilde{\gamma}_d$ then

$$\dot{x} = p, \tag{2.16}$$

$$\dot{p} = -x - \gamma_d p + \sqrt{\gamma_d}\xi(\tau) \quad , \tag{2.17}$$

where the noise source $\xi(\tau)$ satisfies the relations

$$\langle\xi(\tau)\rangle_\tau = 0 \text{ and } \langle\xi(\tau)\xi(\tau')\rangle_\tau = 2\delta(\tau-\tau'). \tag{2.18}$$

1.4 RF bucket size and the validity of linear RF approximation

Conservative part of the system EQ 2.16-EQ 2.17 can be described by a Hamiltonian

$$H(x, p) = \frac{p^2}{2} + \frac{x^2}{2}, \tag{2.19}$$

which is, of course, the Hamiltonian for a harmonic oscillator with unit frequency. As long as we are interested in small oscillations and time intervals much shorter than the damping time this simple Hamiltonian correctly describes the longitudinal motion of a beam.

Whether oscillations for a given particle are small depends on its initial conditions i.e. how far in phase space it was placed with respect to the synchronous particle. Small oscillation approximation often breaks down at the stage of beam injection when particles may fill a considerable portion of the phase space. The figure of merit here is the so-called RF bucket size - the maximum phase space area where particles are still held by the RF. Bucket dimensions can be easily obtained from EQ 2.1 and EQ 2.2. The maximum energy spread is given by

$$\delta_{max}^2 = 2\frac{\alpha U_0}{\pi h E_0}(\tan(\varphi_0) - \varphi_0) \tag{2.20}$$

while the bunch length is limited by

$$l_{max} < 2\varphi_0 \frac{C}{\pi h}. \tag{2.21}$$

On the other hand, away from injection the small amplitude (or linear RF) approximation is usually a very good one for synchrotron oscillations in electron storage rings. Radiation damping keeps the bulk of the beam within several σ_0 in coordinate and within several δ_0 in momentum around the center of the RF bucket. Normally natural bunch length and natural energy spread are both much smaller than the values given by EQ 2.20 and EQ 2.21. Hence, the majority of beam particles are contained within a very small area near the center of the RF bucket where they execute almost perfect harmonic oscillations. Of course, even very small RF nonlinearity brings in qualitatively new effects not present in pure harmonic motion, for instance, frequency dependence on the amplitude. It turns out, however, that there are much stronger factors that make the restoring force on the particle in the RF bucket so nonlinear that the RF nonlinearity becomes negligible. These factors are related to the interaction between the particles and the vacuum chamber and they are usually considered based on the concepts of wakefield and impedance.

2.0 Wakefields and impedances

2.1 The concepts of wakefield and impedance

2.1.1 Interactions between particles in a bunch; Resistive wall example

When categorizing the forces between the beam particles the direct Coulomb interaction is the first one that comes to mind. However, further consideration shows that in the ultrarelativistic case of interest the Coulomb forces are negligible. The transverse force scales as γ^{-2} due to the cancellation of electric and magnetic field components, and the longitudinal force has the same scaling due to the Lorentz contraction. This argues that electrons in the ultrarelativistic beam travelling in free space do not interact significantly.

Another simple consideration, valid for the travel in arbitrary surrounding, is often called the causality argument. It requires that the front particles in a beam do not feel any effect of the trailing ones. This assumes that all particles travel at the speed of light, but it holds quite well for typical electron storage ring energies. On the other hand, the trailing particles may, in principle, be affected by the front ones and this indeed takes place due to the presence of the vacuum chamber.

Generally, Maxwell's equations with appropriate boundary conditions can be solved for the force acting on any beam particle as it traverses the vacuum chamber. Unfortunately, for realistic 3D chamber geometries this solution is practically impossible to calculate numerically let alone to find analytically. There are several important cases, however, that allow exact analytic solution for the force and thus provide a valuable insight to the general problem. These are the cases of two conducting planes, a pillbox cavity, and a smooth pipe with circular cross section and finite conductivity. Solutions to these problems are described in detail elsewhere (e.g. [3], [17], [18]).

For illustration, we will reproduce one of the results of [18] where the Maxwell's equations for the smooth conducting pipe were solved in cylindrical coordinates. It was assumed that the pipe walls were thick enough so that the field leakage was negligible. According to [18] the test charge q_1 travelling a distance x behind the charge q_0 experiences the force

$$F(x) = -\frac{16 q_1 q_0}{b^2}\left(\frac{1}{3}e^{\chi x}\cos(\sqrt{3}x\chi) - \frac{\sqrt{2}}{\pi}\int_0 \frac{z^2 e^{z^2 \chi x}}{z^6 + 8}dz\right), \tag{2.22}$$

which assumes that both charges are travelling on axis and χ is given by

$$\chi \equiv \frac{\sigma_0}{b}\left(\frac{2\pi\bar{\sigma}b}{c}\right)^{1/3}, \tag{2.23}$$

where b is the pipe radius and $\bar{\sigma}$ is the conductivity. Note, that at small x the force is finite and decelerating corresponding to the expected loss of energy by a beam in resistive environment. At large distances $|x| \geq (b^{1/2}\delta_{skin})^{2/3}/\sigma_0$ the force rolls off as $|x|^{-3/2}$. This characteristic length can be understood since the fields induced within the metal extend about one skin depth into the pipe and roughly the same distance behind the test charge. The skin depth δ_{skin} should be taken at the characteristic frequency of the pipe $\omega_{pipe} \sim c/b$.

2.1.2 Wake functions

In the resistive wall example the particle interaction is due to the electromagnetic fields left behind by the front charge in the skin layer of the pipe. Of course, the skin layer is not the only place for those fields to be left. They can get excited as well by any variation in the cross section of the vacuum chamber as illustrated in Figure 2.

In this case the force calculations are more complicated, because, in contrast to the resistive wall, there is no translational symmetry. This makes the force on a test charge dependent not only on the relative position of this charge within a bunch but also on its instantaneous position. However, it is

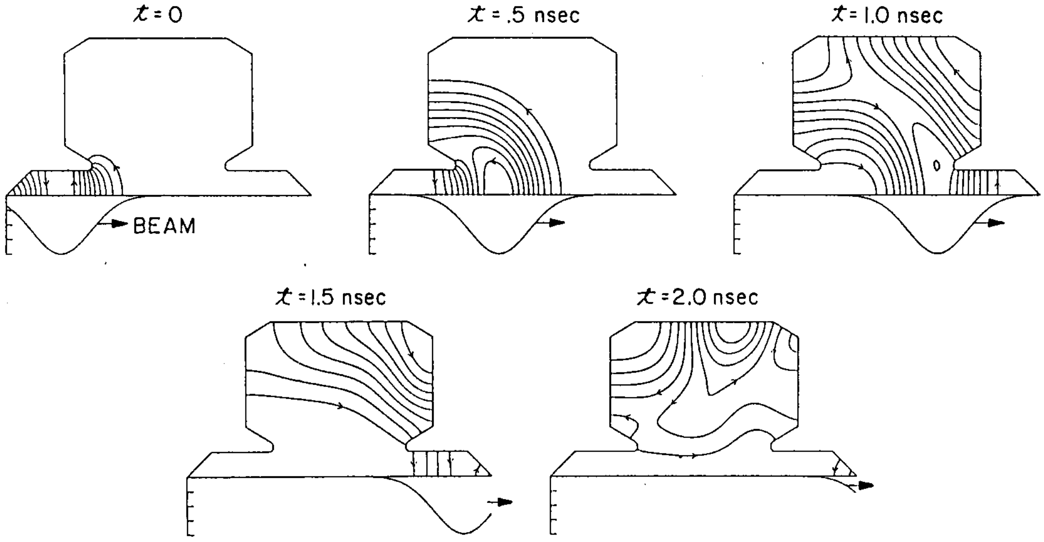

FIGURE 2. Simulation of the wakefield lines from a Gaussian bunch traveling through a LEP RF cavity (from [19]).

intuitively clear that only the average effect of this force matters for beam dynamics (at least for the time scales of interest). This allows simplification of the analysis by introducing wake functions that account precisely for the average force experienced by a particle.

In the longitudinal case the wake function of a cylindrically symmetric vacuum chamber component can be defined (see e.g. [3] for $m=0$) as the average force experienced by a test charge q_1 as it follows distance x behind the driving charge q_0

$$W^{\delta}(x) \equiv \frac{\sigma_0}{q_1 q_0} \int_{-L/(2\sigma_0)}^{L/(2\sigma_0)} F(x, x')\,dx' . \tag{2.24}$$

In this equation L is the length of the component and x' is the longitudinal position with respect to some fixed point in the ring. Both charges are assumed to travel on axis and have δ-function charge density distribution. Note, that applying the causality argument we get that for any wake function

$$W^{\delta}(x) = 0 \text{ , for } x > 0 . \tag{2.25}$$

A simple definition EQ 2.24 utilizes the fact that the integral over the electromagnetic force is independent of the transverse displacement of the test charge in the ultrarelativistic limit (e.g. [16]). In principle, the force also depends on the transverse offset of the driving charge which is ignored in EQ 2.24. However, in most cases the transverse displacement of beams in storage rings is small compared to the beam pipe radius which makes the longitudinal effects related to this displacement negligible. If these effects do become important, as well as for the case of axially asymmetric structures, more general definitions should be used in place of EQ 2.24 (see e.g. [3], [17]). As seen from EQ 2.24 wake functions have units of cm^{-1} in CGS or Ω/s in MKS. Traditionally, when MKS system is used wake functions are measured in equivalent units of V/pC.

With the above remarks, the wake function definition EQ 2.24 is independent of the beam properties and therefore a wake function $W^{\delta}(x)$ characterizes the vacuum chamber component alone. Furthermore, since this definition utilizes a δ-function excitation (charge q_0) it is similar to a Green's function. To find the response of a vacuum chamber component to a finite beam distribution one has to convolute $W^{\delta}(x)$ with the longitudinal beam density $\rho(x)$ (normalized to 1)

$$W^{\rho}(x) \equiv \int_{x} W^{\delta}(x - x')\rho(x')dx' . \tag{2.26}$$

Function $W^{\rho}(x)$ defined in this manner is sometimes called a wake potential or a total wake for the distribution $\rho(x)$.

Utilizing the definitions EQ 2.24 and EQ 2.26 allows the introduction of a wake function for the whole ring as a sum over all the components of the vacuum chamber. If one now understands the wake functions $W^{\delta}(x)$ and $W^{\rho}(x)$ in this sense, it is possible to write the wake-related beam energy loss per turn in the ring as

$$\Delta E_W = e^2 N \int \rho(x')dx' \int_{x'} \rho(x) W^{\delta}(x'-x)dx \equiv e^2 N \int W^{\rho}(x)\rho(x)dx . \tag{2.27}$$

At high intensities this energy loss significantly affects collective beam dynamics. Measurable effects related to this loss will be described later in the chapter.

2.1.3 Single particle Hamiltonian in the presence of wakes

If electrons in a stored beam interact through the wake forces their single particle Hamiltonian EQ 2.19 gets modified to

$$H(x, p, \rho) = \frac{p^2}{2} + \frac{x^2}{2} + U_W(x, \rho), \tag{2.28}$$

where the wake contribution is obtained by integrating the force produced by all the particles in front. The integration of EQ 2.24 yields

$$U_W(x, \rho) = \lambda\sigma_0 \int_x dx'' \int_{x''} dx' \rho(x') W^{\delta}(x''-x') = \lambda \int_x dx' \rho(x') S(x-x'), \tag{2.29}$$

where $\lambda \equiv \frac{N r_0}{\alpha\gamma C \delta_0^2}$ is intensity related parameter, r_0 is the classical electron radius and $S(x)$ is the dimensionless integrated wake defined as

$$S(x) \equiv \sigma_0 \int_x W^{\delta}(x')dx' . \tag{2.30}$$

It is important to note that although one can write the single particle Hamiltonian EQ 2.28, the whole N-particle system is not Hamiltonian if the causality is assumed in the usual form of EQ 2.25. Indeed, for the simplest case $N=2$ the equations of motion for two particles are

$$\dot{x}_{1,2} = p_{1,2}, \tag{2.31}$$

$$\dot{p}_{1,2} = -x_{1,2} - \Theta(x_{2,1} - x_{1,2})\Phi(|x_{2,1} - x_{1,2}|), \tag{2.32}$$

where the first term in right hand side of EQ 2.32 corresponds to the force from the RF potential in agreement with EQ 2.17, $\Theta(x)$ is the step function, and $\Phi(x)$ is some unknown force. It is easy to see that there exists no Hamiltonian $H(x_1,p_1, x_2,p_2)$ that implies these causal forces acting between the particles

$$\dot{p}_{1,2} \neq -\frac{\partial}{\partial x_{1,2}}(H(x_1, p_1, x_2, p_2)). \tag{2.33}$$

The reason for Hamiltonian mechanics and the third Newton's law to break down for such a simple system can be explained as follows. By assuming causality in the form of EQ 2.25 we allow both particles to emit electromagnetic radiation, but only the trailing one to receive it. Since this radiation is not considered a part of the system the two particle Hamiltonian no longer exists. Of course, as soon as we relax the ultrarelativistic requirement $v=c$ this problem goes away provided we wait long enough for the radiation from the trailing particle to reach the front one. In other words the absence of Hamiltonian properties has to do with the time scale of the problem we are interested in. Strictly speaking, in order to apply causality all the time we have to introduce, for example, some absorptive walls, so that the radiation emitted forward by the trailing particle vanishes there.

2.1.4 Impedances

Wakefields describe the interaction between particles and the vacuum chamber in the time domain. It is also useful to consider the same interaction in the frequency domain. Specifically, the energy loss by a test charge in a vacuum chamber component can be viewed as a result of some effective decelerating voltage experienced by this charge. Similarly to electrical circuits this voltage may be related to the current I carried by the test charge as

$$V_\omega \equiv -I_\omega Z(\omega), \tag{2.34}$$

where $Z(\omega)$ is the impedance, subscript ω defines the Fourier component, and the minus sign accounts for the fact that the voltage V is retarding. Since the current carried by a test charge is just a δ-function its Fourier transform is a constant. Therefore, utilizing EQ 2.24 we conclude that the impedance $Z(\omega)$ and the corresponding wake function $W^{\delta}(x)$ are related by Fourier transforms

$$Z(\omega) = \frac{\sigma_0}{c}\int W^{\delta}(x)e^{-i\omega x\sigma_0/c}dx, \tag{2.35}$$

$$W^{\delta}(x) = \frac{1}{2\pi}\int Z(\omega)e^{i\omega x\sigma_0/c}d\omega. \tag{2.36}$$

Similarly to the wake function the impedance for the whole ring is just a sum over all the components which goes along with the intuition that they present themselves in series to the beam current.

As is clear from the last two equations the interaction between the beam particles may be equivalently described in terms of wake functions or impedances. Usually the choice between the two is made depending on whether a particular problem is better treated in the time or frequency domain. It is worth mentioning, that while approximate analytic methods exist for calculating both $Z(\omega)$ and $W^{\delta}(x)$, the most precise numerical techniques integrate Maxwell's equations in the time domain. On the other hand, experimentally available methods usually measure impedance components and therefore, work in frequency domain.

Finally, we rewrite the equation for the energy loss EQ 2.27 in the frequency domain. It is easy to obtain for the Fourier transformed beam density $\tilde{\rho}(\omega)$ that

$$\Delta E_W = \frac{e^2 N}{2\pi}\int Z(\omega)|\tilde{\rho}(\omega)|^2 d\omega. \tag{2.37}$$

It will be shown shortly that due to the symmetric properties of impedance only the real part of $Z(\omega)$ contributes to this energy loss.

2.2 Some properties of wakefields and impedances

In spite of seemingly unrestrictive definitions EQ 2.24 and EQ 2.34 wake functions and impedances possess a whole array of properties that follow from the principles of causality, energy conservation, and others. Detailed discussion of these properties can be found elsewhere (see e.g. [3], [17]). Below is the list of a few essential properties that will be used later in this thesis. These include symmetric properties of the impedance as well as the scaling laws at low and high frequencies.

First of all, since a wake function is a real quantity it follows from the properties of the Fourier transform that

$$Z(-\omega) = Z^{*}(\omega), \tag{2.38}$$

which implies that the real and imaginary parts of impedance are even and odd functions of ω respectively.

Second, from the causality property EQ 2.25 it can be shown that the real and imaginary parts of impedance are not independent but are related through the Hilbert transforms

$$Re(Z(\omega)) = \frac{1}{\pi}\mathrm{P.V.}\int\frac{Im(Z(\omega'))}{\omega'-\omega}d\omega', \tag{2.39}$$

$$Im(Z(\omega)) = -\frac{1}{\pi}\mathrm{P.V.}\int\frac{Re(Z(\omega'))}{\omega'-\omega}d\omega', \tag{2.40}$$

where P.V. denotes the principal value of the integral.

Finally, most asymptotic properties of impedances (and hence wake functions) can be found from simple physical considerations. At $\omega=0$ the definition of a closed orbit (no losses) implies that the real part of impedance should vanish

$$\lim_{\omega\to 0} Re(Z(\omega)) = 0. \tag{2.41}$$

Neglecting for a moment the resistive wall contribution to the impedance we conclude that at low frequencies the impedance is dominated by the largest components of the vacuum chamber that present inductive-like impedance to the beam current. Therefore, we conclude that

$$\lim_{\omega \to 0}\left(\frac{Im(Z(\omega))}{\omega}\right) = const < 0 \text{ (no resistive wall)}. \tag{2.42}$$

However, at the lowest frequencies the dominant contribution to the impedance comes from the resistive wall. Applying the Fourier transform to EQ 2.22 (which is when divided by $q_1 q_0/\sigma_0$ becomes the resistive wall wake function per unit length) results in the low frequency impedance behavior (see e.g. [3], [17])

$$\frac{Z(\omega)}{L} \approx \frac{|\omega|^{1/2}}{bc\sqrt{2\pi\sigma}}(1 - i\,\mathrm{sgn}(\omega)) \quad \text{(low frequencies, resistive wall only)}. \tag{2.43}$$

High frequency impedance behavior is not as transparent. It is clear that extremely short bunches are not affected by the vacuum chamber and therefore the impedance has to roll off at high frequencies. Sometimes it is assumed that at $\omega >> c/\sigma_0$ the longitudinal impedance scales as $\omega^{-1/2}$. This dependence can be obtained from the so-called diffraction model (e.g. [3]) as well as from other analytic methods or numerical calculations. Most of them, however, have limited applicability which is the reason why the topic of high frequency impedance scaling is still being debated in the literature (see references cited in [17]). Fortunately, for this thesis the subject of high frequency impedance scaling has largely academic interest.

2.3 Major impedance components of a storage ring vacuum chamber

A cartoon drawing of a typical storage ring impedance is shown in Figure 3. It shows that an impedance can be categorized into two major parts. At lower frequencies the impedance has mostly isolated narrow-band components. These are, first of all, the fundamental and higher order modes of accelerating cavities. Narrow-band impedance also includes resonator-like contributions from other vacuum chamber components that have a cross-sec-

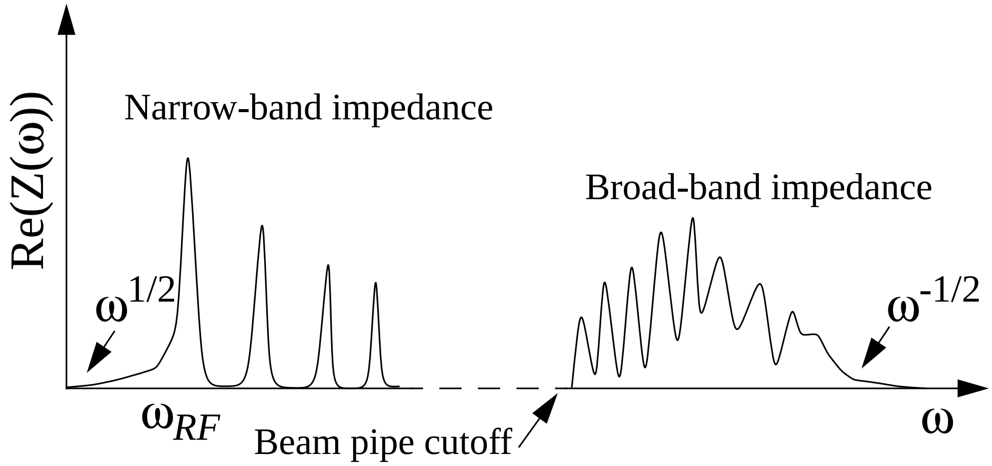

FIGURE 3. Sketch of a storage ring impedance. Lower frequency scaling shown is due to the resistive wall component. The upper limit is as given by the diffraction model.

tion larger than that of a beam pipe, i.e idler cavities, bellows, quadrupole masks etc. Above the beam pipe cutoff frequency the picture becomes more complicated. Various smaller components, like beam position monitors, vacuum chamber transitions, vacuum ports, and others produce wide resonances that merge together, so that it is often impossible to distinguish the contribution of a particular element. This part is usually called a broad-band impedance.

The resistive wall contribution, that varies smoothly with frequency, could be cast as a part of a broad-band impedance. However, since it often makes appreciable contribution at low frequencies (where narrow-band components prevail) it is usually considered separately. As said above, the resistive wall defines the low frequency $\omega^{1/2}$ impedance scaling. It reaches maximum at the frequency of $\omega_{rw} \sim c\chi/\sigma_0$ and falls down rapidly after that.

Narrow-band impedance corresponds to the long range wake or interactions over distances comparable to the ring circumference. For example, various cavity resonances often have quality factors of $Q \geq 10^4$ exceeding the ring harmonic number by orders of magnitude. Therefore, once initiated by a bunch, the ringing of such a mode would last over many turns. As mentioned in the introduction, the collective phenomena associated with multi-bunch or multi-turn behavior fall outside the scope of this thesis. Therefore, only the broad-band impedance (starting from the frequencies on the order of c/σ) that contributes to the coherent single bunch phenomena is relevant for further consideration.

2.4 Other quantities related to wakefields and impedances

In principle, a knowledge of an impedance $Z(\omega)$ or a wake function $W^{\delta}(x)$ for a storage ring allows quantitative description of the interaction between the beam and the vacuum chamber. Unfortunately, neither one of these functions is ever known exactly and even their approximate computation is usually involved. Similarly, it is impossible to measure these functions experimentally. At best limited frequency range measurements for isolated components or parameter measurements for some models of $Z(\omega)$ are feasible. This is why several constants related to $Z(\omega)$ are often used to approximately describe the beam-chamber interaction as well as for comparison with experimentally measured quantities. The two constants most widely used for these purposes are introduced below. It should be noted that knowing these constants allows making order of magnitude estimates only. More detailed description of longitudinal beam dynamics usually requires some parametric and/or numerical models of wake functions and impedances.

2.4.1 *Z/n*

As it was noted prior to EQ 2.42 the low frequency impedance is usually inductive and is proportional to frequency. The limit of

$$\frac{Z}{n} \equiv \lim_{\omega \to 0}\left(\frac{\omega_0 Z(\omega)}{\omega}\right) \tag{2.44}$$

is therefore a constant and it is often referred to as simply Z/n (where it is assumed that $n=\omega/\omega_0$). This constant is a measure of the impedance per unit length at very low frequencies. However, as said above, the interaction between the beam and the vacuum chamber at frequencies this low is not important for the phenomena studied in this thesis, specifically, coherent single bunch longitudinal instabilities induced by short range wakefields. More appropriate figures of merit are the ring impedance at the characteristic frequency of a beam c/σ_0 or Z/n weighted with the bunch spectrum. The latter is sometimes called the "effective Z/n" and denoted as $(Z/n)_{eff}$. The estimate of this quantity is often found in the beam dynamics section of conceptual design reports for storage rings.

2.4.2 Loss factor

The loss factor is the quantity characterizing the beam energy loss per turn due to wakefields. Since this energy loss is proportional to the beam charge eN it is convenient to define the loss factor k as

$$k \equiv \frac{\Delta E_W}{e^2 N} = \int W^{\rho}(x)\rho(x)dx, \tag{2.45}$$

where the last equality utilizes EQ 2.27. It also shows that loss factors and wake functions share the same units.

Note, that the wake related energy loss depends on the bunch shape $\rho(x)$. Therefore, in contrast to Z/n, the loss factor characterizes both the vacuum chamber and beam properties. Further discussion of measurable effects related to the loss factor will take place later in this chapter.

2.5 Some impedance models

Before describing particular models we introduce the dimensionless intensity parameter

$$I \equiv \lambda A \equiv \frac{N r_0}{\alpha\gamma C\delta_0^2} A, \tag{2.46}$$

where A is a numerical factor of the integrated wake (this definition is not mathematically sound but will become clear from the examples below). Introducing this parameter is convenient because the wakefields enter into the single particle Hamiltonian EQ 2.28 linearly and multiplied by λ, which allows combining A and λ into a single intensity parameter I. It is this parameter that enters into various characteristics of single particle and collective motion like, for example, incoherent and coherent frequency shifts. Consequently, since the factor A is taken out from the integrated wake we have to renormalize the latter by

$$S(x) \to S(x)/A\,. \tag{2.47}$$

Throughout the rest of this thesis the integrated wake $S(x)$ will be assumed normalized as given by EQ 2.46 and EQ 2.47.

2.5.1 Resonator and the broad-band resonator models

As mentioned in Section 2.1.1 it is possible to calculate the force on the particle as it travels through the pillbox cavity. This force can be integrated to obtain the wake function. This case is important since accelerating cavities and some other storage ring components can be modeled as pillboxes. Unfortunately, this calculation is rather involved [17], and part of the difficulties comes from the fact that the particles generally excite many resonant modes of the cavity. However, if it is assumed that only one mode (usually the fundamental) gets excited then the calculations of $W^{\delta}(x)$ become simple. The wake function found in this case is usually referred to as the wakefield of a resonator.

The most intuitive (but somewhat hand waiving) way to find $W^{\delta}(x)$ is to first calculate the impedance $Z(\omega)$ and then Fourier transform it. After inspecting the EM fields in a pillbox cavity one can write its impedance as a parallel combination of inductive and capacitive components (corresponding to H and E fields respectively) plus a real shunt impedance R_s that accounts for the wall losses

$$\frac{1}{Z(\omega)} = \frac{i}{\omega L} - i\omega C + \frac{1}{R_s}\,. \tag{2.48}$$

This can be rewritten in terms of the quality factor $Q \equiv R_s\sqrt{C/L}$ and the resonant frequency $\omega_R \equiv \sqrt{CL}^{-1}$ as

$$Z(\omega) = \frac{R_s}{1 + iQ(\omega_R/\omega - \omega/\omega_R)}. \tag{2.49}$$

Performing inverse Fourier transform (EQ 2.36) one can obtain the resonator wake function

$$W^{\delta}(x < 0) = \frac{\mu c R_s}{Q}\exp\left(\frac{\mu x}{2Q}\right)\left(\cos(\mu\varsigma x) + \frac{1}{2\varsigma Q}\sin(\mu\varsigma x)\right), \tag{2.50}$$

where two dimensionless parameters are introduced as

$\mu \equiv \frac{\omega_R\sigma_0}{c}$, $\varsigma \equiv \frac{\sqrt{4Q^2 - 1}}{2Q}$, and Q is assumed to exceed 1/2.

Finally, the integrated wake and the intensity parameter for the resonator can be written as

$$S_{res}(x < 0) = -\exp\left(\frac{\mu x}{2Q}\right)\sin(\mu\varsigma x), \tag{2.51}$$

$$I_{res} = \lambda\frac{cR_s}{\varsigma Q}. \tag{2.52}$$

It was speculated by many authors that the resonator model at low values of Q approximates rather well the broad-band impedance region sketched in the right half of Figure 3. When $Q \sim 1$ (often $Q = 1$ is used) the impedance EQ 2.49 is called the broad-band resonator model. Since this model is flexible and allows analytic calculations of many beam dynamics related quantities it is often used in the single bunch stability analysis. It should be noted, however, that this model must be used with caution at high frequencies where it has incorrect asymptotic behavior.

2.5.2 Inductive and resistive impedances

At low frequencies the resonator model EQ 2.49 becomes essentially inductive

$$Z(\omega) = -i\omega L\,. \tag{2.53}$$

The wake functions and the intensity parameter that correspond to this impedance are

$$W^{\delta}(x) = -\frac{L}{\sigma_0 c^2}\frac{\partial}{\partial x}\delta(x), \tag{2.54}$$

$$S(x) = \delta(x), \tag{2.55}$$

$$I_L = \frac{\lambda L c^2}{\sigma_0}. \tag{2.56}$$

Note, that the factor c^2 disappears from the formulas above if we measure inductance L in nH and σ_0 in cm.

Similarly, for intermediate frequencies on the order of ω_R the resonator impedance becomes strongly resistive and can be approximately modeled as

$$Z(\omega) = R, \tag{2.57}$$

or, equivalently,

$$W^{\delta}(x) = \frac{Rc}{\sigma_0}\delta(x), \tag{2.58}$$

$$S(x) = \Theta(x), \tag{2.59}$$

$$I_R = \lambda R c. \tag{2.60}$$

The δ-functions that appear in these two models often significantly simplify many beam dynamics calculations. For example, it becomes straightforward for these models to find the single particle Hamiltonian given by EQ 2.28. The drawback of both models is their limited flexibility and application range. Indeed, *S(x)* for these models does not have any parametric dependence and both models break down at high frequencies. On top of that, the resistive model does not apply at low frequencies where $Re(Z(\omega))$ should converge to zero. Throughout the rest of this thesis we will use these two models mostly for illustration purposes.

3.0 Beam dynamics from kinetic equations

3.1 Vlasov and Fokker-Planck equations

Electron bunches in storage rings typically hold N~10^8-10^{12} particles that interact with each other through the wakefields. It is impossible and largely useless to describe the individual motion of every electron. However, we may expect that there are statistical laws that define some average characteristics of the whole bunch. As routinely done in statistical physics a macroscopic system is described in terms of distribution functions. Usually the n-particle distribution function $f^{(n)}$ is defined to give the probability for n particles to occupy a certain element of their $2n$-dimensional phase space independent of the location of all the other N-n particles. It is possible to write general kinetic equations which describe the time evolution of all n-particle distribution functions [21]. These equations (often called BBK or BBGYK equations) are coupled so that the equation for $f^{(n)}$ includes the $(n+1)$-particle distribution function $f^{(n+1)}$. This extremely large system of coupled equations is not too useful by itself; however, significant simplifications arise in two important cases i) the interaction between the particles is weak compared to their thermal energy T and ii) an arbitrary interaction but small density of particles. In both cases functions $f^{(n)}$ factorize into the products of the lower order distribution functions $f^{(n-1)}$, which corresponds to neglecting n-particle correlation in position. Often it is sufficient to consider only the lowest order 2-particle correlation, so that the kinetic equation can be written in terms of the single particle distribution function $f \equiv f^{(1)}$, and the interaction is characterized in terms of $f^{(2)}$, which is in turn can be represented as some functional of f.

When the interaction between the particles is small a kinetic equation linear in interaction strength can be written as [21]

$$\frac{\partial f}{\partial t} + \{H(x, p, f), f\} = 0 \tag{2.61}$$

$$H(x, p, f) = \frac{p^2}{2} + \langle\text{potential energy}\rangle = \frac{p^2}{2} + \int U(x - x')dx' \int f(x', p', t)dp', \tag{2.62}$$

where $\{g, f\} \equiv \frac{\partial g}{\partial p} \cdot \frac{\partial f}{\partial x} - \frac{\partial g}{\partial x} \cdot \frac{\partial f}{\partial p}$ denotes the Poisson bracket, H and U are the single particle Hamiltonian and its potential energy. Equation EQ 2.61 together with the self-consistent Hamiltonian EQ 2.62 is called the Vlasov equation named after A. Vlasov, who first derived it for collisionless plasma [22].

The Vlasov equation is time inverse invariant. One can easily see that because EQ 2.61 is formally equivalent to the Liouville equation which follows from time reversible classical mechanics. Therefore, the Vlasov equation cannot describe the evolution to thermodynamic equilibrium. As we know from kinetic theory time inverse asymmetry comes from collision processes which are non-deterministic and thus lead to the entropy growth. Formally collision processes are described by adding the so-called collision integrals to the right hand side of EQ 2.61 (one could say that collision integrals proportional to $\langle U \rangle / T$ to the second power and higher were omitted there). If a system has more than one sort of particles then EQ 2.61 must be written for every component and the collision integrals between this component and all the others have to be included. Often, however, one sort of collisions dominates. For example, as mentioned above for ultra-relativistic electron bunches the Coulomb scattering is usually negligible. Therefore, only one type of collisions is important. These are “electron-photon collisions” or simply radiation.

Langevine equations EQ 2.16 and EQ 2.17 properly account for the radiation effects and are equivalent to the equation for the distribution function *f(x,p,τ)*

$$\frac{\partial f}{\partial \tau} + \{H(x, p, f), f\} = \gamma_d\left(\frac{\partial^2 f}{\partial p^2} + \frac{\partial}{\partial p} p f\right) \tag{2.63}$$

which is simply the Vlasov equation EQ 2.61 with the radiation terms added to the right hand side. Note, that we are now using the natural units introduced in EQ 2.15.

EQ 2.63 belongs to the class of Fokker-Planck equations (e.g. [23]). Similar equations (not necessarily with a self-consistent Hamiltonian) describe a variety of effects in physics, biology and other sciences. General feature of these phenomena is a presence of a stochastic force or noise.

The Fokker-Planck equation EQ 2.63 is nonlinear because the Hamiltonian depends on the distribution function. It is this nonlinearity that makes the general solution impossible even in one dimensional case. When there is more then one dimension the situation is even more complex. For example, in 2D case, when the diffusion is allowed only in one coordinate, as in EQ 2.63, it is impossible to say how many solutions with different long time asymptotic behavior exist [23]. Another way to look at this is that behavior of the systems described by the Fokker-Planck equation may be very diverse depending of the parameters and initial conditions.

3.2 Haissinski solution

A steady state solution of the Fokker-Planck equation EQ 2.63 with the Hamiltonian EQ 2.28 was first considered by J. Haissinski [24]. Since any function of the Hamiltonian $f = f(H)$ matches the left hand side of EQ 2.63 it is a steady state solution of the Vlasov equation. The right hand side of EQ 2.63, however, requires this distribution function to have a Gaussian momentum dependence. Therefore, a steady-state solution of the Fokker-Planck equation is given by

$$f_H = \frac{1}{Z_H}\exp(-H_H(x, p, f_H)), \tag{2.64}$$

where Z_H is the normalizing constant. We will also call this the Haissinski solution which explains the H subscript above.

EQ 2.64 is a nonlinear integral equation. It can be treated analytically only for a few model wake functions. However, EQ 2.64 is a lot easier to solve numerically than the Fokker-Planck equation EQ 2.63. And, more important, it contains an essential qualitative result. The steady state distribution function can be factorized; it is always Gaussian in momentum with an intensity independent rms value of $\sigma_p^2=1$. Therefore, as a stored charge grows, only the coordinate-dependent part of the distribution function changes and deviates more and more from the low intensity Gaussian shape. This corresponds to an increase of the wake potential contribution to the Hamiltonian EQ 2.28. This phenomenon is called the potential well distortion and will be considered in more detail in Section 4.1.

3.3 Stability analysis based on the linearized Vlasov equation

The Haissinski solution describes stored bunches in thermodynamic equilibrium with synchrotron radiation. The characteristic time scale of getting to this equilibrium is given by the damping time $\tau_d=1/\gamma_d$. Does it mean that every beam stored several damping times ends up with the Haissinski distribution? The general answer is no. First of all, for some wake functions the solution of EQ 2.64 does not exist for arbitrary intensities. Second, even when the Haissinski solution formally exists, for it to be physically realizable it has to be stable. To find whether it is the case the stability of the Fokker-Planck equation with respect to the Haissinski solution has to be studied. Often, however, instabilities develop on the time scale much faster than the damping time. In this case radiation may be neglected and the simpler Vlasov equation is used to describe the fast dynamics.

Stability analysis of the Vlasov equation was first developed in plasma physics (see e.g. [25]) and was later applied to storage rings by several Russian authors (see references cited in [26]) and also by F. Sacherer [27]. Since the latter work was better known in the U.S. this approach is sometimes called the Sacherer formalism. Another commonly used name is mode coupling theory. In the simplest form this method is outlined below and a more detailed derivation is given in Appendix B.

A distribution function is represented in the form $f = f_0 + f_1$, where the perturbation is considered small $f_1 << f_0$. Substituting this to EQ 2.61 gives the linearized Vlasov equation

$$\frac{\partial f_1}{\partial \tau} + \{H(x, p, \rho_0), f_1\} + \{H(x, p, f_1), f_0\} = 0 \tag{2.65}$$

where the Hamiltonians are defined by EQ 2.28 and EQ 2.29. It is often convenient to switch to action-angle variables J, φ, defined so that the Hamiltonian of the unperturbed solution depends only on action $H(x, p, \rho_0) \equiv H(J)$. This gives the linearized Vlasov equation in the following form

$$\frac{\partial f_1}{\partial \tau} + \omega(J)\frac{\partial f_1}{\partial \varphi} = \frac{d\rho_0}{dJ}\frac{\partial}{\partial \varphi}U_W(x(J, \varphi), f_1), \tag{2.66}$$

where $U_W(x(J, \varphi), f_1) = I\int f_1(J', \varphi', \tau)S(x(J, \varphi) - x(J', \varphi'))dJ'd\varphi'$ and $\omega(J) \equiv \frac{dH}{dJ}$.

Usually harmonically varying solutions

$$f_1(J, \varphi, \tau) = \sum_m \tilde{f}_m(J)\exp(i\Omega\tau - im\varphi) \tag{2.67}$$

of EQ 2.66 are sought. Each term in the sum above is called the azimuthal mode with periodicity m. In case several solutions exist for the same m they are called radial modes of a given azimuthal harmonic. Substituting EQ 2.67 into EQ 2.66 transforms it to the dispersion relation

$$i(\Omega - m\omega(J))\tilde{f}_m = \tag{2.68}$$
$$I\frac{d\rho_0}{dJ}\frac{\partial}{\partial\varphi}\left(\int\sum_m \tilde{f}_m(J')e^{i\Omega\tau - im\varphi'}S(x(J,\varphi) - x(J',\varphi'))dJ'd\varphi'\right)$$

which in principle makes it possible to find all collective frequencies Ω as well as the radial structure of collective modes. We may expect that at low current all the Ω's will be real corresponding to a stable situation. However, at some intensity value the first two of collective frequencies become complex $\Omega = Re(\Omega) \pm i\gamma$; the corresponding collective modes are said to couple. This is the threshold of instability (neglecting radiation damping). Note that we use the same symbol γ for the growth rate of unstable modes as we used earlier for the relativistic factor. This should not create any confusion, since after being absorbed into the definition of intensity EQ 2.46 the relativistic factor will no longer appear in this thesis.

Once the exponentially growing solutions appear the linearized Vlasov equation cannot be used since the linear approximation breaks down. What happens beyond the threshold is still an active research topic. It will be introduced in the last section of this chapter and then the essential portion of this thesis will be devoted to experimental and theoretical aspects of this subject. But prior to that we will briefly describe some effects that take place below the threshold.

4.0 Subthreshold phenomena

4.1 Potential well distortion

The Haissinski solution has a Gaussian momentum dependence which can be integrated out to obtain the particle line density $\rho_H(x)$ and the potential $U_H(x)$

$$\rho_H(x) = \frac{1}{Z_H}\exp(-U_H(x)), \tag{2.69}$$

$$U_H(x) = \frac{x^2}{2} + I\int\rho_H(x')S(x-x')dx'. \tag{2.70}$$

In principle, these equations can be solved numerically for any wake function. For illustration purposes we will use two model wake functions for a purely inductive and a purely resistive impedances given by EQ 2.55 and EQ 2.59. In the first case the Haissinski solution leads to an algebraic equation for $\rho_H(x)$ which can be solved by iterations. For the resistive impedance EQ 2.69 and EQ 2.70 allow analytic solution which reads [28]

$$\rho_{H_R}(x) = \frac{\sqrt{2/\pi}\exp(-x^2/2)}{I_R(\coth(I_R/2) - \mathrm{erf}(x/\sqrt{2}))}, \tag{2.71}$$

$$U_{H_R}(x) = \frac{x^2}{2} + \log\left(\frac{1-\tanh(I_R/2)\mathrm{erf}(x/\sqrt{2})}{1-\tanh(I_R/2)}\right). \tag{2.72}$$

Solutions for several intensities for both wake functions are plotted in Figure 4. It shows that inductive impedance maintains the potential well and the bunch shape symmetric with respect to $x=0$; the bunch centroid does not move. Meanwhile, as the intensity increases the bunch (and the well) becomes longer (wider), and deviates from the zero current Gaussian (parabolic) shape.

The situation is quite different for the case of resistive impedance. The main intensity related effect is the bunch becoming skewed. It leans forward to compensate for the energy loss due to the real impedance. There is still some bunch lengthening but it is rather weak. It is easy to show that in the

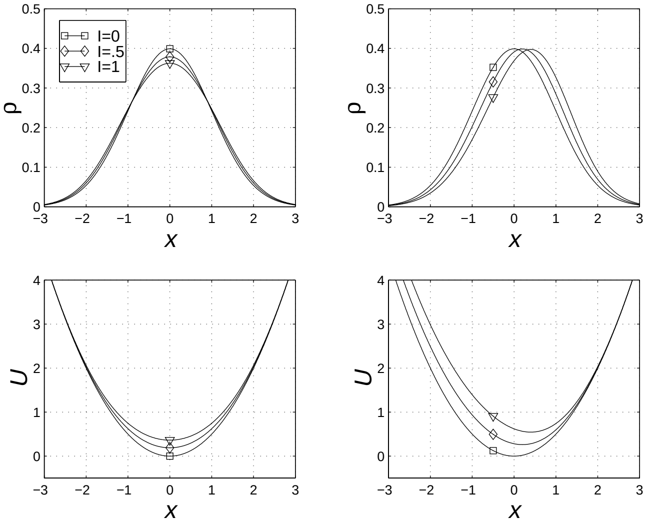

FIGURE 4. Haissinski solution for inductive (left) and resistive impedances. Same legend applies to all subplots.

limit of low intensities the change in the bunch length scales quadratically with current in contrast to a linear dependence for the inductive case.

Impedances of real-life vacuum chambers are different from the models above. They may have complicated frequency dependence. However, the qualitative features of the potential well distortion effect remain the same. It is still true that the real (resistive) part of impedance brings in centroid shift and bunch shape asymmetry, while the reactive part is responsible for the change in bunch length. The latter is usually positive, i.e. bunches become longer as intensity grows. This is because the impedances of the common vacuum chamber components are inductive when the bunches are not extremely short. It is possible to add some capacitive elements to the vacuum chamber in order to reduce or reverse the bunch lengthening. This has been proven experimentally [29] but it had limited practical value, since the gains were taken away by turbulent bunch lengthening above the instability threshold.

4.2 Shift and spread in the synchrotron frequency

As current increases the potential well changes according to the Haissinski solution and the wake potential distorts the low current parabolic RF potential well. This, in turn, significantly modifies the single particle motion by making the particle oscillation frequency amplitude dependent, as it is illustrated in Figure 5 for inductive and resistive impedances.

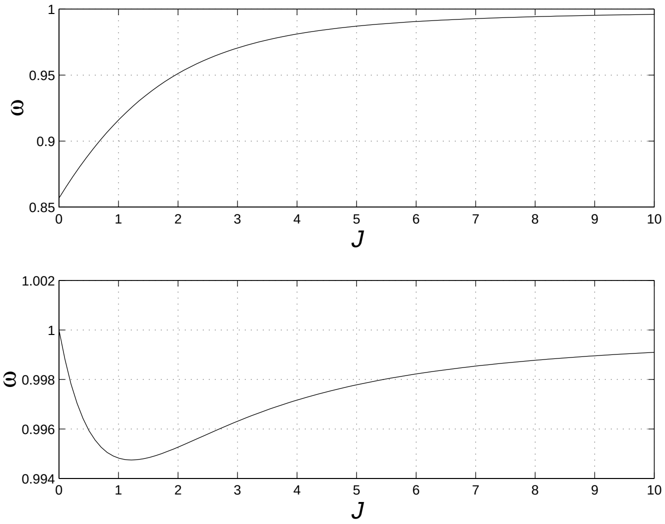

FIGURE 5. Frequency dependence on amplitude for inductive (top) and resistive impedances at unit intensity $I_L = I_R = 1$.

Since the particles are distributed over amplitudes, with the distribution given by the Haissinski solution, this leads to the frequency spread among different particles. This spread

$$\Delta\omega = \sqrt{\int \rho_H(J)(\omega(J) - \langle\omega\rangle)^2 dJ} \tag{2.73}$$

as well as the average frequency

$$\langle\omega\rangle = \int \rho_H(J)\omega(J)dJ \tag{2.74}$$

are intensity dependent and in the limit of low intensity $\langle\omega\rangle \to 1$, $\Delta\omega \to 0$. This is illustrated in Figure 6. It shows that the inductive impedance brings in significant frequency shift and frequency spread which are both proportional to the intensity. In contrast, for the resistive impedance, the intensity dependence is quadratic; the frequency spread and shift are small.

The wake contribution generally changes the quadratic RF term in the total potential, so that even the low amplitude particles have frequencies dif-

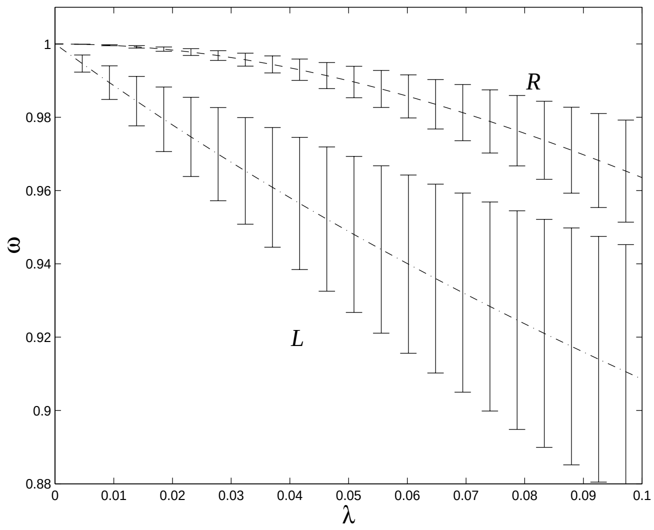

FIGURE 6. Frequency shift due to potential well distortion for inductive and resistive impedances (*L*= 10 nH, *R*=1 kΩ). Broken lines correspond to the average frequency (EQ 2.74) and bars represent rms frequency spread (EQ 2.73).

ferent from 1. Resistive impedance, however, is an exception. Therefore, it can be considered as "more nonlinear" than most other impedances since it brings higher harmonics to the particle motion without much affecting the fundamental.

4.3 Synchronous phase shift

As it was noted before the real part of impedance causes a bunch to shift with respect to the RF bucket. For example, for a purely resistive impedance this shift can be found from EQ 2.71 as $\Delta x = \int x\rho_{H_R}(x)dx$. The intensity dependence of Δx is plotted in Figure 7. The shift is approximately linear up to rather high intensity values. Of course, for a typical vacuum chamber we expect this dependence to roll off much faster due to the bunch lengthening brought by the inductive component of the impedance.

The bunch centroid shift is a measurable quantity. It is often quoted in degrees of RF phase and is called the synchronous phase shift. For a given RF voltage the slope of the synchronous phase shift with respect to the intensity is the integrated measure of the real part of the impedance.

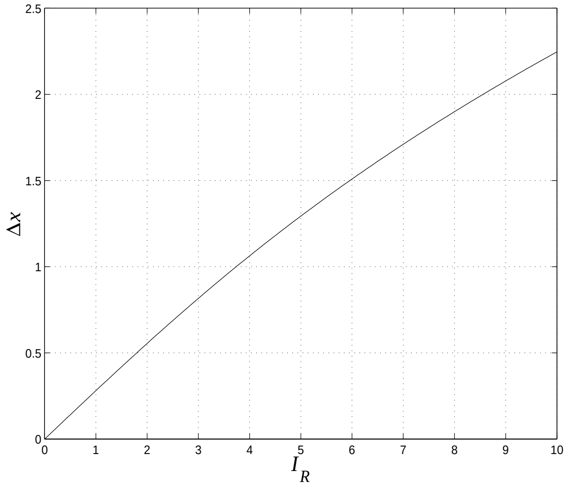

FIGURE 7. Beam centroid shift with intensity for resistive impedance.

Another related quantity is the loss factor defined in EQ 2.45. The energy balance of the stored beam can be written utilizing the loss factor k as

$$eV_{RF}\cos(\varphi_0 + \Delta\varphi) = U_0 + ke^2N, \qquad (2.75)$$

where U_0 is the synchrotron radiation energy loss per turn, φ_0 is the zero current synchronous phase, and $\Delta\varphi$ is the synchronous phase shift. When the latter is small we get for the loss factor

$$k = -\frac{\Delta\varphi}{eN}V_{RF}\sin\varphi_0. \qquad (2.76)$$

It follows from EQ 2.37 and EQ 2.45 that for a given longitudinal beam density the loss factor is related to the integrated wakefield or to the real part of the impedance $Z(\omega)$ as

$$k = \int W^{\rho}(x)\rho(x)dx = \frac{1}{2\pi}\int Re(Z(\omega))|\tilde{\rho}(\omega)|^2 d\omega. \qquad (2.77)$$

For short Gaussian bunches the ω dependence of Z can be neglected above so that we get for the real part of the impedance

$$R = \frac{2\sqrt{\pi}\sigma_0 k}{c}. \qquad (2.78)$$

Note that eliminating the loss factor from EQ 2.76 and EQ 2.78 gives the $\frac{1}{2\sqrt{\pi}}$ zero intensity slope seen in Figure 7.

Similar to the slope of the synchronous phase the loss factor is constant at low intensity and usually rolls down at higher currents due to the bunch lengthening.

5.0 Microwave and saw-tooth instabilities

5.1 General remarks

As we mentioned before there is solid experimental evidence that above some intensity threshold the Haissinski solution becomes unstable. Above this threshold the energy spread starts to grow with intensity and also the bunch lengthens beyond the values expected from the potential well distortion. This effect is sometimes called the anomalous or turbulent bunch lengthening and it often becomes a limiting factor of the machine performance. Another widely observed effect is the appearance of the synchrotron frequency sidebands to the high frequency revolution harmonics of the beam position monitor (BPM) signal spectrum. This suggests that the beam particles exercise some coherent motion. The frequency of the signal observed is usually in the microwave region corresponding to a typical centimeter scale bunch length. This is why the phenomenon is loosely called a microwave instability.

Although the above effects have been observed on almost every electron (and many proton) machine the detailed features of the microwave instability were different. This applies to the threshold relation to the ring parameters, scaling laws above the threshold, detailed behavior of the BPM signals etc. It is conceivable that part of the difference comes from the spread in the machine parameters and that different physical phenomena play a role in each case. It is especially true if we compare storage rings from different design generations. For older machines, build without thorough understanding of the impedance effects on beam stability, it was common, for example, to observe a total beam loss on the time scale of several turns due to microwave instability. On the other hand, for modern rings, where the impedance budget is an integral part of the design, the effects of the microwave instability can be mild enough to allow the operation above the threshold.

As far as the theoretical explanation of the phenomena it was summarized by B. Zotter [30]: "There is no satisfactory explanation for the existence of a "turbulent" threshold and the region above it, where anomalous bunch lengthening and bunch widening (increase of energy spread) occur simultaneously. Several empirical models yield the results in good agreement with observation over a limited range of parameters, usually for longer bunch lengths where the impedance is mainly inductive. Computer simulation can yield satisfactory results also for shorter bunches, but has rarely been applied to existing machines. Unfortunately, it also does not give insight into the physical processes involved."

5.2 Some theoretical findings on the longitudinal microwave instability

As it is common for a developing field there is still no widespread terminology to describe the effects associated with the microwave instability and the very definition of this instability varies greatly among different authors. The same phenomenon can be referred to as the microwave instability, slow microwave instability, mode coupling, etc. Throughout the rest of this thesis we will follow the terminology of [3] except we will use a broader definition of the microwave instability as any single bunch instability that produces microwave frequency signals corresponding to coherent particle motion. The relation of this instability to other collective instabilities in storage rings is shown in Figure 8. This figure also shows a possible classification of the regimes of microwave instability based on the relation of the growth rate to the synchrotron frequency and radiation damping rate. The four bottom items in the tree shown in Figure 8 will be explained later.

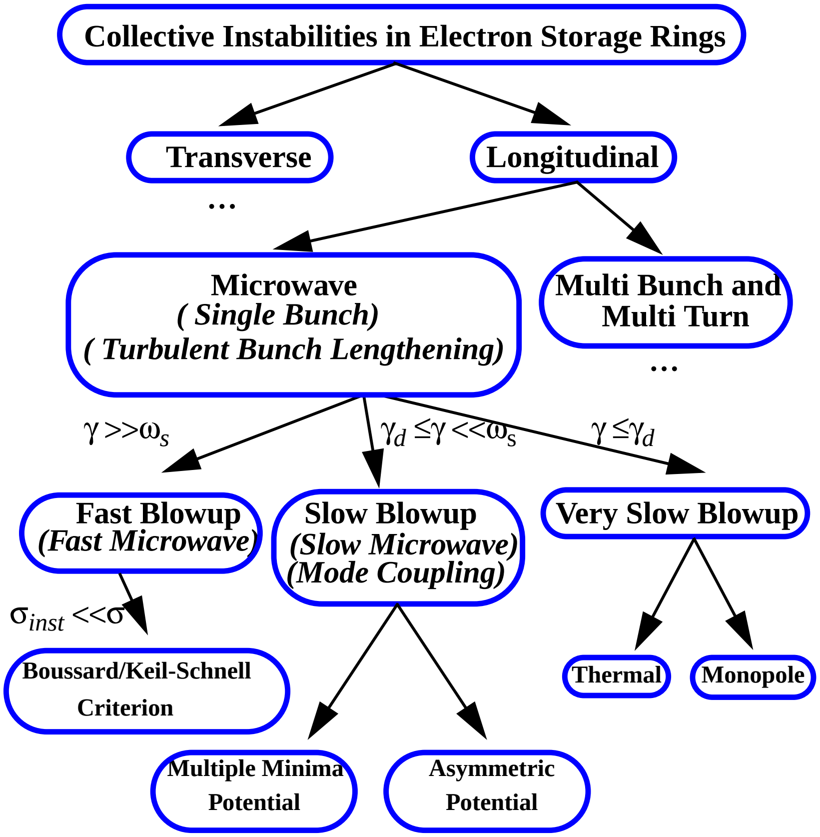

FIGURE 8. Collective instabilities in electron storage rings. Alternative definitions used in literature are shown in italics. Ellipsis denotes omitted hierarchy and σ_{inst} stands for the characteristic perturbation size due to the instability.

In the rest of this section we will describe several theoretical findings related to the microwave instability. Realizing that complete coverage is impossible we will only touch upon some facts relevant to the rest of this thesis referring to the review material in [3] and [30] for further information.

5.2.1 Boussard criterion vs. mode coupling theory

The Boussard criterion is the most widely known criterion for the microwave instability. It limits the maximum bunch intensity λ_{max} by

$$\lambda_{max}\sqrt{\frac{2}{\pi}}\frac{C}{Z_0\sigma_0}\left|\frac{Z}{n}\right|_{eff} \leq 1 \tag{2.79}$$

This criterion is applicable when the instability growth rate is much higher than the synchrotron frequency $\gamma>>1$ and the characteristic scale of the perturbation due to the instability is shorter than the bunch length. It was conjectured by D. Boussard [34] from the analytically obtained Keil-Schnell criterion for unbunched beams [35]. Boussard's argument was that a perturbation with a wavelength much shorter than the bunch length sees the bunch as a coasting beam. Later several authors derived the Boussard criterion analytically (e.g. [36], [37]) using different approaches.

Although the Vlasov equation can be a basis for the derivation of the Boussard criterion [36] one cannot talk about individual modes when $\gamma>>1$. Therefore, the physics of the Boussard's threshold is completely different from the mode coupling threshold that follows from the dispersion relation of the linearized Vlasov equation. Since $\gamma<<1$ regime applies to the phenomena in the SLC damping rings as well as to many other modern electron storage rings we will concentrate on this regime and will not use the Boussard criterion.

5.2.2 Finding the threshold

For realistic impedances little can be done analytically to find the instability threshold. Many people have worked on this problem which basically amounts to solving EQ 2.68 using different simplifying assumptions. The common one was using some model distribution for $\rho_0(J)$ instead of a self-consistent Haissinski solution. This may be valid for proton machines, however, in electron storage rings it can lead to incorrect results as it was first shown by K. Oide and K. Yokoya [38].

These authors have developed a method to numerically solve the dispersion equation EQ 2.68 by transforming it to a matrix eigenvalue problem for a real matrix M. They found that the potential well distortion greatly affects the threshold value and therefore it has to be properly accounted for. Also, they showed that M can be made symmetric when both conditions hold i) $\rho_0(J)$ is monotonic and ii) the potential well is symmetric $U(x)=U(-x)$. Since every symmetric matrix has real eigenvalues the latter case is stable. This is consistent with the bunch being stable at low intensities when it has a Maxwell-Boltzmann distribution.

Although solving the linearized Vlasov equation numerically is a reliable method to predict the instability threshold it almost seems like unnecessary work. Indeed, this method is complicated and provides much more information than just the threshold value. When this extra information is not needed it would be convenient to have some analytical expression for the threshold. It is conceivable that such an expression could be derived from the Haissinski solution which is much easier to obtain than to solve the linearized Vlasov equation. Unfortunately, so far nobody was able to derive such a criterion analytically. However, several empirical criteria have been proposed. They state that the instability appears as soon as somewhere within a bunch...

- second minimum appears in the potential $U(x)$ (G. Besnier [39]),
- $\omega(J)=0$ (P. Wilson [40]),
- $\omega(J)\leq 1/2$ (azimuthal mode coupling, R.Baartman and M. D'yachkov [41]),
- $d\omega(J)/dJ=0$ (radial mode coupling, K. Oide [42]).

The discussion of these criteria will be postponed until Chapter 5.

5.2.3 Meller-Schonfeld theory

The obvious limitation of the linearized Vlasov equation is that it is not applicable to the non-linear regime of instability. In plasma physics this is dealt with by the so-called quasi-linear theory where the feedback of an unstable mode onto $\rho_0(J)$ is taken into account. Mathematically it is done by adding a term proportional to $\left|\tilde{f}_m(J)\right|^2$ to the Vlasov equation for $\rho_0(J)$. It is well known (e.g. [43]) that quasi-linear interaction leads to the creation of a plateau on the $\rho_0(J)$ located around the resonant region where $\omega(J)\approx\Omega/m$ and particles resonantly interact with the unstable mode. Note, that in classical quasi-linear plasma theory it is assumed that an unstable mode is actually a continuum of waves with random phases.

A conceptually similar approach to the longitudinal microwave instability was proposed by R. Meller [44] who used the technique developed by J. Schonfeld [45] for the case of transverse beam dynamics. R. Meller showed that there is another solution to the Fokker-Planck equation EQ 2.63 which is different from the Haissinski solution. This solution is periodic in time, and it is stationary in some rotating coordinate frame. The physics of this solution is that a finite amplitude azimuthal mode $\tilde{f}_m(J)\exp(i\Omega\tau - im\varphi)$ causes a periodic perturbation to the potential well which in turn creates *m* times *n* resonant islands in the bunch phase space. Here *n* is the number of roots of the equation $\omega(J) = \Omega/m$ which gives the radial location of the islands $J_{res}^{(1)}, \ldots, J_{res}^{(n)}$ that are equally spaced in azimuth. In order to obtain the resonant solution one requires these islands to be just the size enough to support themselves through the modulation of the total potential. If a thermal equilibrium is also assumed one obtains the resonant solution which can be written for a single resonance in the form [44]

$$\rho_M(r) = \frac{1}{Z_M}\exp(-H_H(J(r)) + \sigma(r)), \tag{2.80}$$

where *r* is the action coordinate inside a resonant island and $\sigma(r)$ is a (complicated) function that is zero outside the island and corrects the Haissinski solution inside the island to make it essentially flat. This solution no longer can be factorized in *x*-*p* variables, that makes the energy spread grow with intensity.

Another idea of R. Meller was to analyze beam stability from a thermodynamic point of view. He constructed the free energy for the bunch treating the synchrotron radiation as a heat bath. He showed that at some intensity the resonant solution may become energetically favorable over the Haissinski solution causing the bunch distribution to switch. In reference [44] such a switch is also called a thermal instability. According to [44] this instability can be viewed as a phase transition during which the time displacement symmetry breaks for the system of beam particles. Indeed, the single particle

Hamiltonian EQ 2.28 does not have any explicit time dependence. On the other hand, at $\tau \to \infty$ along with the steady state Haissinski solution the Fokker-Planck equation EQ 2.63 allows time dependent (limit cycle) resonant solution. Hence switching to the latter the system looses time displacement symmetry.

5.2.4 Beam dynamics above the threshold

Meller's approach describes a possible final state of a bunch above the threshold but it does not tell how the bunch gets there. Amazingly, very little is known about the dynamics above the threshold. We will mention several papers here.

Y. Chin and K. Yokoya considered a quasi-stationary approach [46] where a beam distribution was assumed Gaussian with a time-dependent rms value. They showed that an overshoot phenomena is possible when the bunch length grows due to the instability but then it comes down somewhat and levels off.

S. Heifets considered the relaxation oscillations between the Haissinski and the resonant solutions [47] and speculated that this could be a mechanism for the saw-tooth instability discussed below.

G. Stupakov with co-authors applied some analytical techniques from plasma physics to describe the nonlinear stage of beam evolution by approximately solving the Fokker-Planck equation [48]. The authors showed that the bunch behavior can be qualitatively different depending on the beam parameters and the impedance. For example, the bunch may simply reach a steady state, or it may overshoot, or it may slowly oscillate around some level. The authors also claim that it is essential to consider the Fokker-Planck rather than the Vlasov equation otherwise the dynamics becomes trivial. Unfortunately, the method of [48] only works in the vicinity of the threshold.

Finally, there are several papers that use particle tracking to study the dynamics above the threshold. Generally, there is a major computational difficulty when the time scale of the phenomena is much longer than the synchrotron period. However, as computers become more powerful it is possible to track a high number of particles long enough to obtain solid result. For example, R. Baartman and M. D'yachkov [49] considered the behavior of electron bunches in the case of a resonator wake creating a double well potential *U(x)*. They observed the "saw-tooth" like oscillations of the bunch size.

K. Bane and K. Oide used particle tracking to study beam dynamics for the SLC damping rings [50]. They used a realistic wakefield calculated numerically for a 1 mm rms Gaussian bunch [51]. They observed the growth and saturation of a quadrupole mode above some threshold. At even higher values there was some slow erratic modulation of the energy spread.

5.3 SLC damping ring saw-tooth instability

5.3.1 Old saw-tooth instability

A dramatic encounter with the microwave instability occurred at the SLC damping rings several years ago. As the intensity in the rings was raised as a part of 1992/1993 luminosity upgrade people observed a threshold of about 3×10^{10} particles per bunch above which beams exhibited characteristic saw-tooth behavior.

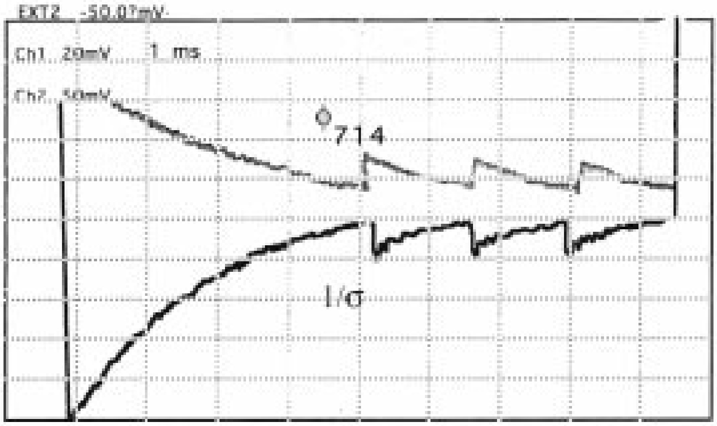

FIGURE 9. Typical data from the "old saw-tooth" instability (from [31]). One SLC injection cycle is displayed. Signals proportional to the beam phase and inverse bunch length are shown on the upper and lower traces respectively.

A few ms after the injection the bunch length (as seen by a BPM peak-detector circuit) was sharply rising on a μs scale and then it was relaxing back with a time constant of about 1 ms (Figure 9). This process would repeat periodically until extraction. Similar saw-tooth behavior was reported for the synchronous phase of a stored bunch. SLC operation above this threshold was not successful due to extreme beam jitter in the linac significantly degrading the luminosity. The source of the jitter was obvious - since the phase of instability was random with respect to extraction every bunch was launched differently into the linac; another contribution could have been coming from unequal transport properties for bunches of different shapes.

To further study the phenomenon some frequency domain measurements were performed. It was found that when the instability was present a BPM signal spectrum showed strong sextupole sidebands to the revolution harmonic. Other harmonics (dipole, quadrupole, etc.) were also observed. An attempt to raise the current even further has revealed a second threshold of about 4×10^{10} ppb above where the instability would go into a “continuous mode” where instead of saw-tooth oscillations bunches would blow up and then saturate at some level. The instability was found to get weaker and even go away with the decrease of accelerating voltage. The latter, however, had to be held at around 1 MV throughout most of the store to provide good beam capture and adequate bunch length. Some attempts have been made to fix the damaging influence of the instability by modulating the voltage within a store. The success of this, however, was limited.

Simulations were performed and they explained the instability as azimuthal mode coupling (although to our opinion the experimental evidence to support that was inconclusive) due to very strong inductive wakefields in the vacuum chamber [32]. A decision was made to overcome the instability by refurbishing the chamber and replacing or eliminating many inductive elements. A two million dollar upgrade project went ahead and new identical vacuum chambers were installed in both damping rings for the 1994 run [33].

Compared to the old chambers the new ones had smoother transitions, synchrotron radiation masks combined with bellows, the flex joints and kicker magnet bellows eliminated etc. Also new high frequency lower impedance BPMs were installed. The total inductance was calculated to be reduced from 33 nH to 6 nH, which however only approximately accounts for some of the hard to characterize elements of the vacuum chamber. Simulations have been performed for a new vacuum chamber and the instability threshold was predicted to move up to 5-6$\times10^{10}$ ppb. However, in reality it went down to 1.5-2$\times10^{10}$ and people have observed "new saw-tooth" instability.

5.3.2 New saw-tooth instability and motivation for the thesis

Fortunately, the instability was not as strong and it was possible to run the SLC with the instability present. Towards the end of 1994/1995 run damping rings were running with bunches of 4.5$\times10^{10}$ ppb. The behavior of the instability has changed somewhat from the old one. Instead of being mainly a sextupole mode the instability switched to a quadrupole mode. It still had a transient nature but the saw-tooth behavior changed to sine-like modulation on the ms time scale. This could no longer be seen on the peak detector circuit but was rather observed with the spectrum analyzer used as a receiver set to a quadrupole sideband frequency [33]. Instability was still very sensitive to the accelerating voltage, and it was possible to see the "continuous" mode at some combination of values for the accelerating voltage and the charge stored. Wire scanner measurements have shown an increase of the energy spread above the instability threshold. Bunch length measurements have been made with a streak camera, but they did not reveal any evidence of the instability other than a bunch lengthening. Thus, it was unclear what the quadrupole sidebands to the revolution harmonics really meant. In addition, it was no longer possible to identify the instability as the source of jitter for the SLC, and yet some jitter was still seen downstream of the damping rings. Therefore, the questions still remained open about the instability

- Why was it still there and what was the physics of it?
- What was it really doing to the beam?
- What was the effect (if any) of the instability on the SLC performance?

The research work that lead to this thesis was largely aimed to answer these questions. The last two of them are experimental and the hope was that answering them would help with the first question as well. It was obvious that to proceed further experimentally one had to use new hardware or find a better way of utilizing existing ones. This is the subject of the next chapter.

Chapter 3

Experimental apparatus and techniques

1.0 Accelerator physics aspects of the SLC damping rings

1.1 Damping ring parameters and basics of operation

1.1.1 Purpose and parameters

As it was briefly discussed in the introduction the SLC has two damping rings used to increase the brightness of electron (NDR) and positron (SDR) beams. Both rings operate at a beam energy of 1.19 GeV and are almost identical in the design of their vacuum chambers and most other components. Main parameters for both rings are shown in Table 1.

Parameter	**Symbol**	**Value**
Energy	E_0	1.19 GeV
Typical Population per Bunch	N	4.5×10^{10}
Orbit Circumference	C	35.27 m
Revolution Frequency	f_0, $\omega_0/2\pi$	8.5 MHz
Bending Radius	R	2.037 m
Bending Field	B_0	1.948 T
Approximate Horizontal, Vertical Tunes	$\nu_{x,y}$	8.23, 3.43
Approximate Quadrupole Gradients (F, D)		6.2, 7.3 kG/cm
Momentum Compaction	α	0.015
RF Frequency	f_{RF}	714.000 MHz
Harmonic Number	h	84
Typical RF Voltage	V_{RF}	800 kV
Zero Current Synchrotron Frequency	f_{s0}, $\omega_{s0}/2\pi$	102 kHz

TABLE 1. SLC damping ring parameters.

Parameter	**Symbol**	**Value**
RF Cavity Properties		
Loaded Shunt Impedance	R_s	2.5 MΩ
Loaded Quality Factor	Q	6860
Coupling	β	2.5
Approximate Injected Transverse Emittances (e+, e-)	ε_{inj}	2×10^{-3} m, 10^{-4} m
Fractional Injected Energy Spread	δ_{inj}	$\sim10^{-2}$
Injected Bunch Length	σ_{inj}	~3 ps
Radiation Integrals (Soft Edge Model [9])	I_2	2.805 m^{-1}
	I_3	1.3595 m^{-2}
	I_4	-0.027 m^{-1}, -0.421 m^{-1}
Energy Loss/turn from Synchrotron Radiation	U_0	79.2 KeV
Horizontal Partition Number (SDR, NDR)	J_x	1.01, 1.15
Energy Damping Time (J_x = 1.01, 1.15)	τ_d, γ_d^{-1}	1.78 ms, 1.91 ms
Horizontal Damping Time (J_x = 1.01, 1.15)	τ_x	3.50 ms, 3.07 ms
Vertical Damping Time	τ_y	3.53 ms
Fractional Equilibrium Energy Spread (J_x = 1.01, 1.15)	δ_0	7.12×10^{-4}, 7.39×10^{-4}
Zero Current Bunch Length (f_{s0} = 102 kHz; J_x = 1.01, 1.15)	σ_0	16.7, 17.3 ps
Horizontal Emittance (Zero Coupling, J_x = 1.01, 1.15)	$\gamma\varepsilon_x$	2.99×10^{-5} m, 2.63×10^{-5} m
Approximate Vertical Emittance (10% coupling)	$\gamma\varepsilon_y$	3×10^{-6} m

TABLE 1. SLC damping ring parameters.

One can see that the SLC damping rings provide roughly a factor of 4 reduction in the transverse emittance for the electrons and factor of 70 reduction for positrons. During high current operation beam energy spread and bunch length at extraction are roughly 30% higher [6] than the zero current quantities given in Table 1. Therefore during the store longitudinal emittance shrinks roughly a factor of 1.5 and the bunch length coming out is much larger than it was at injection. This is not surprising because the preaccelerator as well as the rest of the linac consists of S-band accelerating sections that require rather short bunches. In fact, short incoming bunches $\sigma_{inj} << \alpha\delta_{inj}c/\omega_{s0}$ are grossly mismatched to the RF bucket. This causes them to filament and blow up their longitudinal emittance roughly factor of 40 during the first few synchrotron periods. Later, the emittance gradually shrinks due to the radiation damping, and the bunch length becomes on the order of σ_0. To match extracted beams back to the S-band linac the SLC employs a bunch compressor after each damping ring that trades-off an increase in the beam energy spread for shorter bunch length. In the compressors beams effectively go through a 90° phase space rotation that results in the final bunch length of about 2 ps.

Note, that according to Table 1 the rings differ only in their damping partition numbers and related quantities. Originally, both rings had the same horizontal partition number J_x=1.01. During one of the performance upgrades the electron damping ring magnetic circumference was stretched to raise the value of J_x to 1.15. It allowed a decrease of the horizontal damping time and equilibrium emittance at the expense of the corresponding longitudinal quantities. This illustrates an important point that the SLC damping rings are mainly needed for transverse damping. In the longitudinal direction the damping is not crucial, especially since the compressors provide additional flexibility. The only important requirement for the longitudinal parameters of extracted beams is stability. Unfortunately, this is exactly where rings fail to a certain extent, since, as mentioned in Chapter 2, stored beams become longitudinally unstable at less than half the nominal current.

Much more could be said about damping ring design, operations and beam dynamics. Due to the constraints of this thesis the transverse and spin dynamics description as well as various engineering issues will be omitted. Below we will only discuss the ring components that directly relate to the longitudinal dynamics and/or diagnostics. Descriptions of other important and often technically challenging components like kickers, septum, spin rotators etc. can be found in [7], [8]. These references also describe various beam physics issues not limited to longitudinal dynamics.

1.1.2 Timing system features

Electron and positron rings mainly differ in the timing of operation. The store time in the SDR is 16.6 ms compared to 8.3 ms in the NDR. A longer store in the SDR is needed because positron bunches transported from the target have poorer transverse emittance then the electron bunches produced by the gun. The exact factor of two difference in store times is due to the fact that both rings nominally run with two bunches. However, out of those four bunches, each positron bunch but only every other electron bunch end up at the interaction region.

Another timing difference between the two rings is that two electron bunches are injected in NDR on the same turn, while in SDR each subsequent positron bunch is injected in the middle of the store of the previous one. Furthermore, in the NDR the production bunch goes first in and out of the ring. It is followed by a scavenger bunch separated by 39 empty RF buckets. Since the ring harmonic number equals 84 this means that electron bunches are not exactly opposite to each other but rather displaced by two buckets. SDR, on the other hand, has two bunches separated by 41 empty RF buckets and circulating exactly opposite to each other. This makes SDR BPM signals somewhat easier to interpret than those at NDR.

The description above is simplistic. It only briefly talks about the most common “colliding” mode out of many other possible configurations of the SLC timing system. Many experiments that will be described later in this thesis were done while in those less standard configurations. Some of them are 1) stored beam (or two beams) - injection/extraction kickers off and beam is stored for a requested period of time, usually 1 to 20 minutes; 2) long stores - similar to the nominal operation, except the injection rate is 60 Hz, hence the store time in SDR is 33.2 ms; 3) various other combinations of reduced duty factor but nominal store time in either ring, i.e. 1, 10, 30, or 60 Hz running, so that for substantial amount of time a ring stays without beams.

1.1.3 RF system

With the exception of the numerous feedback loops, the damping ring RF systems are rather simple. Each ring is powered by a 50 kW klystron operating CW at the frequency of f_{RF}=714 MHz. The klystron power is split in half to go into two 2-cell RF cavities installed roughly opposite to each other. The cavities were designed to handle total accelerating voltage up to 1 MV. The lower limit is, of course, zero, but in practice it is impossible to have a good capture of incoming beam when the gap voltage is below 600 kV. Nominal operating voltage is around 800 kV, and it is usually adjusted to optimize the transmission through the ring and RTL (ring-to-linac) section or even further downstream.

Several damping ring feedbacks will be referred to in later discussion. These are 1) amplitude loop, which adjusts the total accelerating voltage amplitude in both cavities, 2) two tuner feedback loops (one at each cavity) that control the cavity match to the incoming RF power, 3) S-band feedback loop to synchronize the ring RF phase to the injected and extracted beam phases (defined by the corresponding linac sections), 4) direct feedback loop that effectively adjusts the cavity shunt impedance and is used to minimize transient beam loading effects at injection and extraction. Detailed description of these and other feedback loops as well as other aspects of the SLC damping ring RF system can be found in [7] and [8].

1.2 Damping ring wake function and related quantities

The wake function for the new SLC damping ring vacuum chamber was calculated [50] using the time-domain parts of the MAFIA family of computer programs. A short Gaussian bunch with rms length σ_d=1 mm was taken as a driving bunch. In the simulations it was run through all the structures that make up the vacuum chamber. Electromagnetic fields left by the driving bunch in those structures were calculated and then properly averaged to obtain a wake function. Such a calculation gives, of course, a total wake for the driving beam $W^{\rho_d}(x)$ rather than the causal wake function $W^{\delta}(x)$. To approximately find the latter the authors of [50] proposed flipping the front part of $W^{\rho_d}(x)$ and adding it to the back. The causal wake function $W^{\delta}_{DR}(x)$ obtained in this manner as well as $W^{\rho_d}(x)$ are shown in Figure 10.

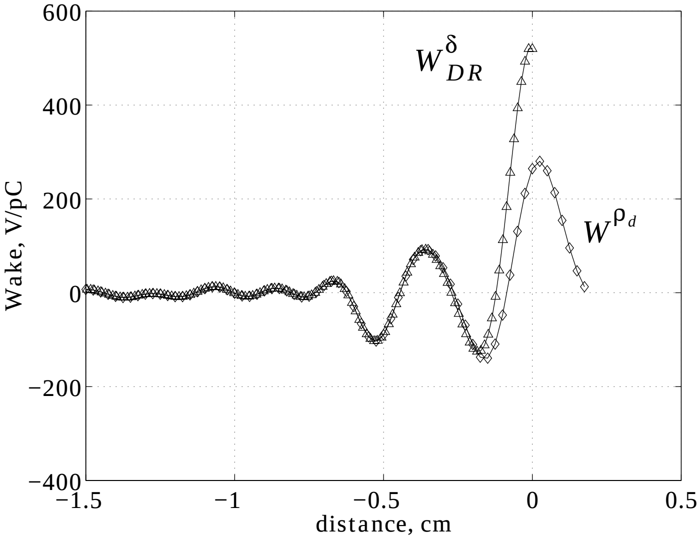

FIGURE 10. Calculated damping ring wake functions (from [50]).

It is clear that both wake functions should only be considered approximate. Some uncertainty comes from a finite σ_d, while other uncertainties are due to approximations made from modelling difficult vacuum chamber objects (see [50], [51]). In addition, there is no solid basis for the flipping procedure. In particular, the authors of [50] mention that this calculated wake is likely to have uncertainty in corresponding inductance value on the order of several nH. Another problem with this wake function is evident from Figure 10. The area under $W^{\delta}_{DR}(x)$ is positive and according to EQ 2.35 this implies non-zero *Re(Z(0))* or losses at DC.

In spite of all these problems we side with the authors of [50] that using this wake function is useful to model the damping ring current dependent behavior.

1.2.1 Equivalent resistance

As mentioned in Section 5.3.1 of Chapter 2 the new damping ring vacuum chamber has a largely resistive impedance since it was purposely designed by eliminating grossly inductive objects from the old chamber. The resistive character of the impedance can be seen by comparing the Haissinski distribution for $W^{\delta}_{DR}(x)$ with the analytic solution corresponding to a pure resistance R_e. Fitting the resistance value we obtained the best agreement between the beam densities (in the least squared sense) for R_e=926 Ω at N=10^{10} ppb. As seen from Figure 11 the distributions are quite similar. Varying the value of N within the range of 5×10^9-2×10^{10} ppb changes the value of R_e by less than 1%.

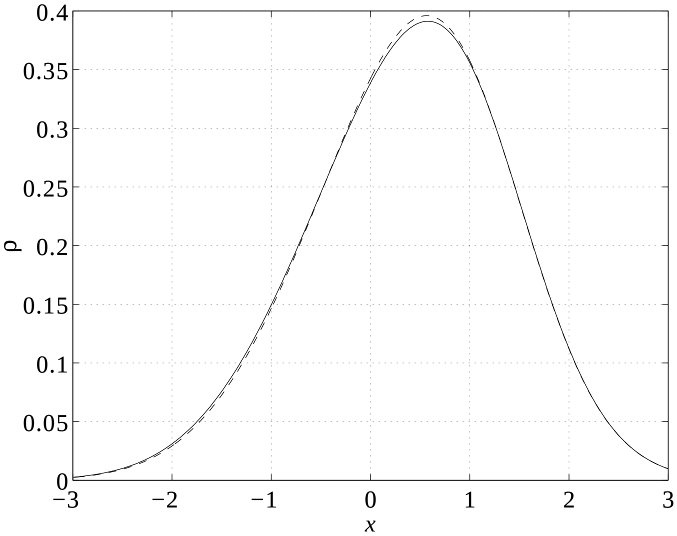

FIGURE 11. Haissinski solutions for damping ring wake function (solid) and for a pure resistive wake function (dash).

1.2.2 Loss factor calculation

References [50] and [51] do not quote the value for the loss factor k. Although it can be estimated from the equivalent resistance, a more reliable estimate is obtained directly from $W^{\rho_d}(x)$ by a Fourier transform. From the definition of total wake EQ 2.26 the Fourier transform of a total wake produced by a bunch with a density $\rho_0(x)$ is related to the same quantity for the driving bunch as

$$F[W^{\rho_0}(x)] = F[W^{\delta}(x)]F[\rho_0(x)] = F[W^{\rho_d}(x)]\frac{F[\rho_0(x)]}{F[\rho_d(x)]}. \tag{3.1}$$

For Gaussian bunches the last ratio is also a Gaussian, and when substituted in the definition of the loss factor EQ 2.45 it gives

$$k = \int F^{-1}\left[F[W^{\rho_d}(x)]\exp\left(\frac{\omega^2({\sigma_0}^2 - {\sigma_d}^2)}{2\sigma_0^2}\right)\right]\frac{\exp(-x^2/2)}{\sqrt{2\pi}}dx. \tag{3.2}$$

Given $W^{\rho_d}(x)$ all the integrations and Fourier transforms in EQ 3.2 can be performed numerically. At nominal RF voltage V_{RF}=800 kV this yields the value for the loss factor of 15.3 V/pC.

1.2.3 Frequency shift/spread for the damping ring wake

Given the wake function subthreshold beam dynamics quantities can be calculated. For further reference we present in Figure 12 the intensity dependence of the incoherent frequency shift and spread. These calculations were performed similar to those in Section 4.2 of Chapter 2 except we used $W_{DR}^{\delta}(x)$ as a wake function.

Non-zero frequency shift slope at zero current indicates that there is some inductive component in the impedance corresponding to the damping ring wake. According to Figure 12 the synchrotron frequency f_s changes by about 3.6 kHz in the range of currents 1×10^{10}-2×10^{10} ppb which assumes the value of f_{s0} from Table 1. However, due to the approximate character of $W_{DR}^{\delta}(x)$ this number for the frequency shift is approximate since even a few nH of inductance may appreciably affect it.

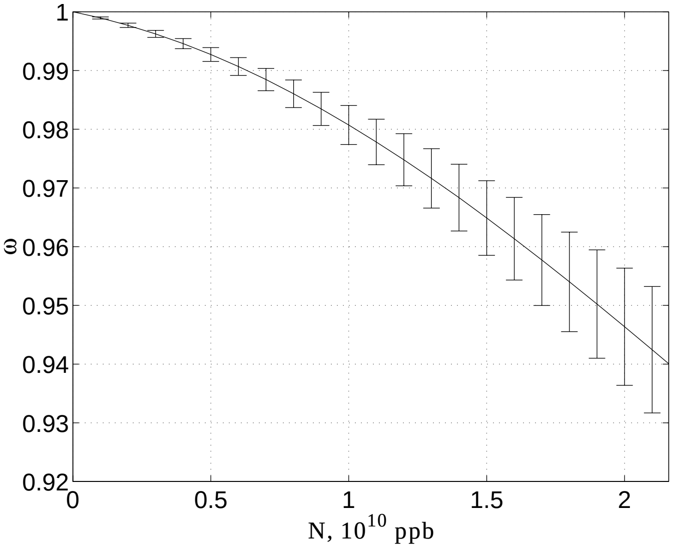

FIGURE 12. Frequency shift due to potential wake distortion calculated for the damping ring wake function. Bars represent rms frequency spread.

1.3 Damping ring beam diagnostics

1.3.1 Beam position monitors

BPMs are the most numerous diagnostic devices in the damping rings. Each ring has 49 BPMs that are mainly used to measure transverse beam trajectories. Several BPMs are dedicated for other purposes including beam dynamics studies. The drawing of the standard damping ring BPM is shown in Figure 13.

The basic principle of BPM operation is the following. The beam induces image charges on the inner surface of the vacuum chamber. According to Maxwell’s equations the axial distribution of the image charges mimics the radial displacement of the beam. These image charges follow the beam as closely as possible until they hit a BPM gap shown in Figure 13. After hitting this gap the DC component of the image current as well as some AC component go all the way around the inner BPM cavity while the rest of the AC component jumps across the gap. Consequently, a beam passing through a BPM excites currents on the walls of the inner BPM cavities that can be considered as transmission lines. The sum of the transmission line voltages measured by

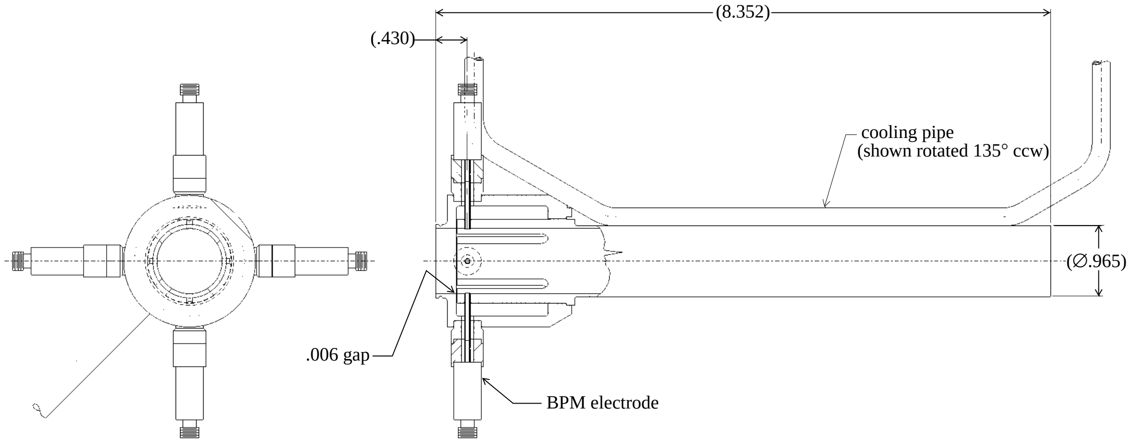

FIGURE 13. Damping ring 1” BPM drawing. Dimensions are in inches. Adapted from SLAC drawing SA-237-112-24.

any two opposite BPM probes is proportional to the total beam current, while the voltage difference relates to the transverse displacement in the corresponding direction. It is clear that the voltage variation with time $V(t)$ is related to the beam line density $\rho(z/c)$ which makes it possible to use BPMs for longitudinal beam profile measurements. However, since a BPM presents different impedance $Z(\omega)$ to different frequency components of the image current the dependence between $V(t)$ and $\rho(z/c)$ is more complex then just a direct proportionality. For example, there exists some higher frequency cutoff beyond which BPMs become largely insensitive. Detailed calculation of $Z(\omega)$ for real BPMs such as the one shown in Figure 13 is only possible numerically. However, there are some analytical approaches based on transmission line theory that can be used for approximate calculations in simplified geometry. Further discussion of this topic falls beyond the scope of the thesis and can be found elsewhere (e.g. [11], [12]).

Due to radiation hazards no measurements are possible in the direct vicinity of a BPM when the ring is in operation. In the SLC damping rings BPM signals are brought upstairs to the so-called kicker support building or to other places where all the diagnostics and control system interfaces are located. A minimum cable length required to patch signal from a damping ring BPM to the kicker building (where we had most of our setups for longitudinal diagnostics) is about 50 feet which presents significant attenuation at higher frequencies. Since the high frequency contents of the signal is valuable for longitudinal diagnostics the standard RG223 cable overwhelmingly used at SLC was not the best one for this purpose. This is why the cable runs from several BPM electrodes designated for longitudinal beam dynamics studies were equipped with a 1/2” or 1/4” HELIAX cables. A typical frequency spectrum at the kicker building end of this cable is shown in Figure 14.

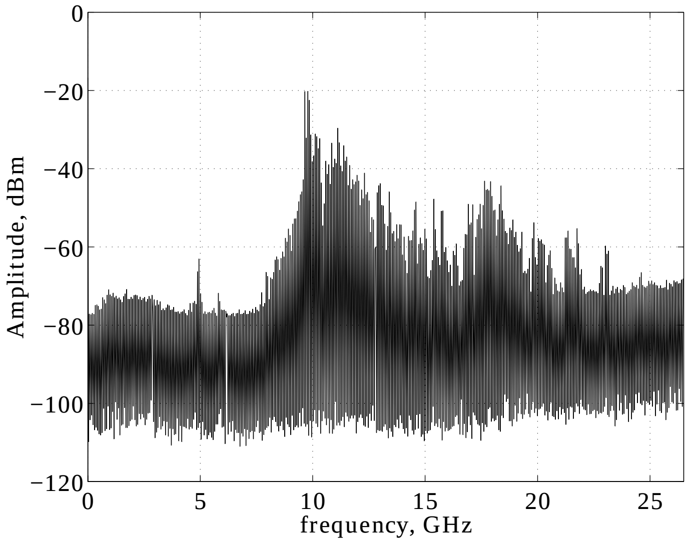

FIGURE 14. BPM signal spectrum taken with an HP 50000 swept spectrum analyzer. A 10 GHz high pass filter is connected to the input.

It is clear that there is a significant (20 dB above the noise level) signal component at frequencies as high as 20 GHz. Detailed discussion of this spectrum as well as further processing of BPM signals will take place in Section 5.0.

1.3.2 Synchrotron light ports and optical transport system

The frequency limitation of BPM-based beam diagnostics can, in principle, be bypassed by switching to the optical part of the electromagnetic spectrum. Synchrotron radiation emitted by a beam contains the information on both transverse and longitudinal distributions. To provide a path for this radiation a synchrotron light port was installed in each ring's vacuum chamber. This port consists of a water cooled molybdenum mirror inside the vacuum chamber together with a fused silica window in its wall. The mirror is oriented 45° with respect to the beam trajectory and is displaced radially a few cm back from it. This mirror accepts the synchrotron radiation from a bending magnet a few feet upstream and reflects it through the window.

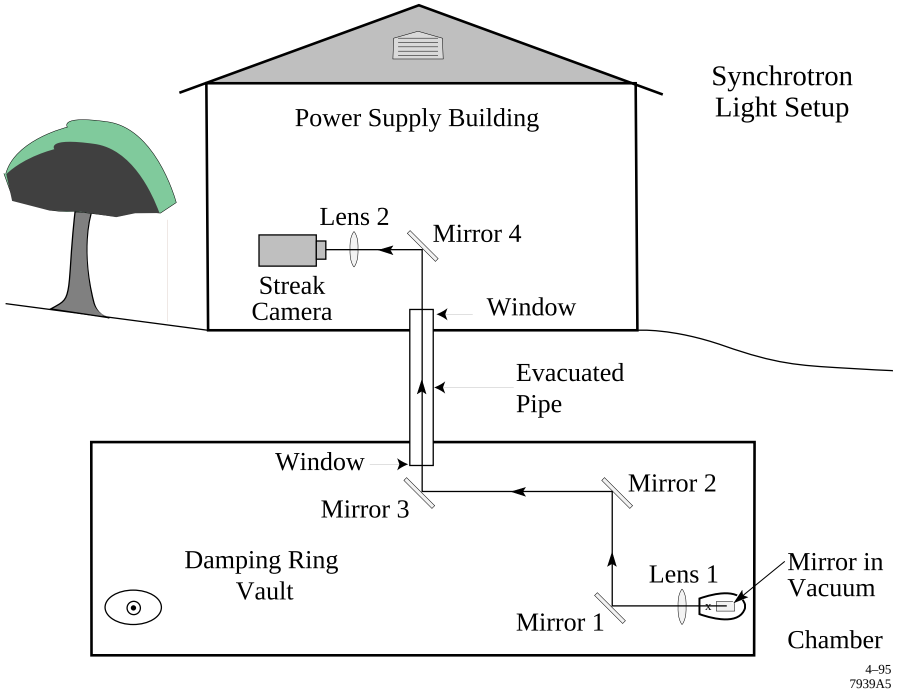

FIGURE 15. The damping ring optical transport line (from [6]).

As it was discussed in Chapter 2 the synchrotron radiation is dominated by frequencies on the order of ω_c which is equivalent to the wavelength of 0.67 nm for the SLC damping rings. Since this is well into the soft X-ray regime only a very small part of the incoming radiation power reflects off the first mirror. The frequency content of this reflected portion is in the optical regime, so a conventional transport optics is used to bring this light further upstairs. A cartoon view of this transport line used before 1997 run is shown in Figure 15 and it is further discussed in [6].

Note, that Lens 1 in this setup withstands a significant radiation flux that causes gradual transparency degradation. This is why this setup was slightly modified in the summer of 1997 when Lens 1 was replaced by a 2.5 m focal length parabolic mirror and two more flat mirrors were added prior to Mirror 1. This has solved the problem of optical degradation but resulted in a more complicated alignment procedure.

Once the synchrotron light is brought upstairs it is usually split between several diagnostic lines. Transverse beam distribution is often monitored by a gated camera [13], while the longitudinal beam profile is measured with a streak camera which will be described later.

1.3.3 Toroids

Although total beam charge can be deduced from BPM signal it can be measured more precisely by a toroid. This device basically acts as a secondary winding in a transformer in which beam trajectory makes up a primary winding. Each SLC damping ring has two toroids located at injection and extraction lines (LTR and RTL). The ratio of the currents in these two toroids is usually quoted as ring transmission. Since most current losses occur during the first few turns after the injection the readings of the toroid at extraction section relate more closely to the actual charge stored. This is why we normally used extraction section toroids (TORO 40 for electrons and TORO 71 for positrons) to quote beam charge. Similar to other toroids in the SLC the RTL toroids can be calibrated down to one percent absolute accuracy. In contrast to the toroids at many other locations these particular toroids tend to be quite stable. Even when uncalibrated they typically show current readings with only a few percent error.

1.3.4 Wire scanners

Other important diagnostics are two wire scanners located in the RTL sections for both electrons and positrons. Wire scanners intercept beams with three wires (in x, y, and 45 degrees between x and y) that emit low energy electron flux proportional to the amount of charge hitting them. Some fraction of this spray in the direction transverse to the beam motion is allowed to exit the vacuum chamber thorough a thin stainless steel window. This radiation subsequently gets detected by a photo multiplier tube (PMT). When the wire scanner moves transversely to the beam direction the pickup signal from the PMT samples the transverse charge distribution. Of course, this scan cannot be done on a single ultrarelativistic bunch. Instead, wire scanners move slowly (few seconds to get across the beam cross-section) and measure transverse beam sizes averaged over many extracted bunches. This may result in substantial errors if extracted beam trajectory differs from one store to the next.

Since the energy deviation of a beam particle is related to the amplitude of its transverse oscillation it is possible to infer beam energy spread from the transverse beam size. Assuming that the dispersion η_x and beta functions are known the energy spread can be found as [14]

$$\delta = \frac{1}{\eta_x}\sqrt{{\sigma_x}^2 - \beta_x\varepsilon_x}\,. \tag{3.3}$$

Extensive measurements of the beam energy spread vs. current and damping ring RF voltage using this technique were reported in [6].

1.3.5 RF system diagnostics

Most RF system parameters like accelerating voltage, cavity tuning angles, feedback loop setting etc. are routinely available from the SCP. Some of the corresponding analog signals for advanced diagnostics are also available. However, monitor and drive ports together with the rest of the low-level RF electronics are located in the building which is separate from the two that house the rings. This location (so-called damping ring alcove in sector 2 of the linac) is inconvenient for the experiments when electrical length changes due to the outside temperature are important. This had to be taken into account in some of our measurements.

One of the operating parameters of the RF system that crucially affects longitudinal beam dynamics is the total accelerating voltage. The readouts are nominally available in the SCP for the total voltages in each cavity and the individual voltages in each of the cells. Also available are the loading angles for each cavity that relate the phases of the induced cavity voltage and the generator current. Unfortunately, it has been our experience that the SCP readings for these values are inconsistent because they do not reproduce the value of the synchrotron frequency at extraction as seen in the BPM spectrum. This could be related to the way the accelerating voltage is regulated in the damping rings. The amplitude loop regulates on the sum of the magnitudes of all the cell voltages rather that on a vector sum. However, since the inconsistency can not be completely removed by taking into the account the difference in the loading angles there must be other factors present as well. These could result from incorrect calibration of the amplitude readouts, unaccounted path length differences etc. This is why the quoted SCP values of the RF voltage should be taken cautiously. When we had the synchronous frequency readings available we used them rather than the SCP readings to deduce the correct value for the accelerating voltage.

2.0 Control system and data acquisition

2.1 SLC triggers

Thorough description of the SLC timing system lies outside the scope of this thesis and can be found elsewhere ([7], [54]). What follows is a simplistic description of several kinds of triggers available in the SLC damping rings that were extensively used in our experiments. The most common are ordinary triggers (TRIG in SCP) that can be set by a SCP user to be issued at a specified time within the injection cycle. The repetition rate for these triggers matches the current machine rate. Also there are the so-called TRBRs that for our purposes work the same as regular triggers except they always operate at a fixed repetition rate. Finally, there are also the TRYY triggers that are issued by the control system when it runs the correlation plot utility that is discussed below. TRYY triggers are special in two ways 1) since they are issued in conjunction to the correlation plot data acquisition they are not periodic and have a maximum rate of a fraction of a Hz, 2) their timing cannot be adjusted from the SCP.

2.2 Buffered data acquisition and correlation plot utility

SCP provides two utilities that can be used for tracking short term dependencies between various beam and machine parameters. Buffered data acquisition program runs at rates up to 120 Hz and records up to 1024 machine cycles. This utility is convenient for recording data from BPMs, TOROIDs and GADC (gated ADCs). The gate timing for the latter can be adjusted from the SCP and the gate is issued automatically when the buffered data acquisition is running.

The correlation plot utility also allows recording various machine variables including the readings of the GADCs. The highest data acquisition rate is a fraction of a Hz and the maximum data buffer length is 512 points. Compared to the buffered data acquisition this utility has many more features. For example, it allows setting step variables other than time to scan various machine parameters during the measurement. Other useful features of this utility are described in [53].

When there is a need to measure a physical value that is not already available in the SCP the first step to try is to use a GADC in conjunction with either buffered data acquisition or correlation plot utilities. In order to do this, a measured quantity must be represented as a voltage level, which can be subsequently sampled by a GADC at any time during the store. Then the data acquisition utilities allow correlating recorded GADC readings with other beam or machine parameter measurements available through the SCP.

In a more complex case when the amount of data grows beyond several voltage levels to be sampled during the SLC cycle the use of GADCs becomes largely ineffective. This includes, for example, the case when we want to measure the evolution of some beam derived signal throughout a significant part of the damping ring store. In this case the amount of data is large, and it is acquired and processed by some dedicated measurement instrument, for instance, a digitizing oscilloscope. In these circumstances a more complex procedure of interfacing the hardware to the SLC control system has to be implemented. This procedure is outlined below.

2.3 Interfacing GPIB hardware to the SLC control system [55]

The easiest way to take data in the damping rings is to run a measurement device in a standalone mode. Later the average characteristics of the beam as well as the machine parameters during the measurement can be pulled out from the SCP history buffers. This, however, may not be enough for the measurements that are sensitive to the pulse to pulse variations in the beam and machine parameters. Characterizing the instability properties can be one of such measurements. Similarly, if the data is taken with a stored bunch then pulling the beam and/or machine parameters from the history buffer offline may lead to large systematic errors.

This is why there is often a need to interface the data taking with a particular instrument (or multiple instruments) to the SLC control system. In practice, implementing this interface requires, first of all, that the data acquisition on the instrument itself is controlled and synchronized with the SLC cycle. Second, the data recorded cannot be transferred directly to the main control system computer (MCC) but has to be stored someplace else, usually the computer that controls the measurement instrument. Finally, this data storage has to be organized in such a way that during an off-line analysis the data could be put into correspondence with the machine variables recorded by the MCC for the same SLC cycle.

In practice, the data acquisition and storage is done on one of several unix hosts distributed throughout the SLC that run the HP-VEE program. This software allows controlling the data acquisition for GPIB and VXI based instruments. The core of a typical data acquisition program is a loop that waits for the trigger, makes the measurement, and dumps the data onto a disk.

The actual interface to the MCC can be done by using the correlation plot utility. The handshake is implemented in two steps. First of all, this utility issues a TRYY trigger during every machine cycle for which it takes the data. Second, this program communicates with the remote unix hosts running HP-VEE and receives the values for the so-called physical variables. The correlation plot data acquisition does not proceed to the next machine cycle until the values of all the physical variables are received. Therefore, if the HP-VEE loop includes a routine that sends a physical variable at the completion of the data recording, then the correlation plot utility and the remote data acquisition are guaranteed to go in sync.

In principle, one dummy physical variable is enough to achieve synchronous running. In practice, it is convenient to increment the value of that variable making it a counter. Then, along with sending the counter value to the MCC its value can be appended to the name of the data file. This allows for easier identification of the data taken during a particular SLC cycle. In some cases additional physical variables are used. Usually these are the results of online data processing or the actual measurement results, when they can be represented as a few real numbers.

A typical setup with an oscilloscope interfaced to the SLC control system is shown in Figure 16. In this case the oscilloscope is recording the traces of the instability signal that for the purposes of this discussion can be thought of as

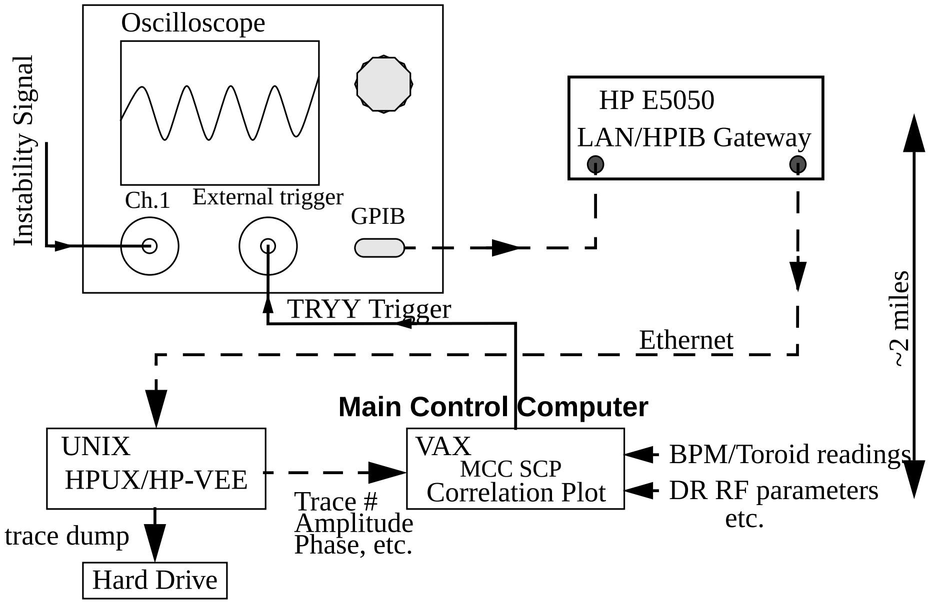

FIGURE 16. Interfacing an oscilloscope to the SLC control system.

varying amplitude sinusoidal signals. The HP-VEE program saves these traces to a disk and also extracts the values for the amplitude and phase of each trace and sends them together with a counter number to the correlation plot utility. The correlation plot in turn records those values plus all the relevant damping ring parameters like the beam current, RF voltage etc. Note that such a setup is quite flexible. It can be easily extended to multiple GPIB controlled instruments including the streak camera.

3.0 Synchronous phase measurement apparatus [56]

3.1 Traditional way to measure the synchronous phase and its limitations

Although other signals carrying beam phase information exist the simplest one to use is a BPM pickup signal. It includes the fundamental harmonic of the RF frequency the phase of which relative to the RF in the accelerating cavity defines the synchronous phase up to some constant offset. For large phase shifts the synchronous phase can be simply measured with an oscilloscope or a mixer-based phase detector. Smaller phase shifts require more accurate tools.

The most precise general purpose instrument to measure the phase of RF signals is the vector voltmeter. It is traditionally the instrument of choice for synchronous phase shift measurements ([57]- [59]).

However, as we found out in our experiments we could not measure the synchronous phase shift reliably with a Hewlett-Packard 8508A vector voltmeter. This is not surprising because the accuracy standard vector voltmeters provide is not sufficient for the SLC damping rings. For example, the specifications for the HP 8508A state an 0.8° phase accuracy within 1 mV to 100 mV input signal range and several times lower accuracy outside of it [60]. Another disadvantage of this device is the lack of convenient control over the averaging constant which is important for synchronous phase measurement. Indeed, in a noisy environment a significant increase in sensitivity can be achieved from averaging the phase over the interval comparable to the sampling time.

To overcome these limitations of the vector voltmeter we came up with the following solution.

3.2 New apparatus

In our apparatus we modify the approach described above in two ways. First, we do not perform the phase comparison at the fundamental RF frequency but rather downmix both beam and RF cavity signals to roughly 25 kHz where audio measurement techniques are available. Second, for the actual phase measurement we use the SR830 DSP Lock-in Amplifier manufactured by Stanford Research Systems. This device has a relative phase error of 0.01°, adequate input sensitivity and temperature stability, and it provides complete control over the time averaging constant. Other features we found useful for this measurement include power line notch filters in the signal arm, auxiliary ADC channels and complete GPIB capability.

The basic idea of our apparatus is shown in Figure 17. To provide an LO arm for the downmixing, we use an RF synthesizer. The low pass filters cut

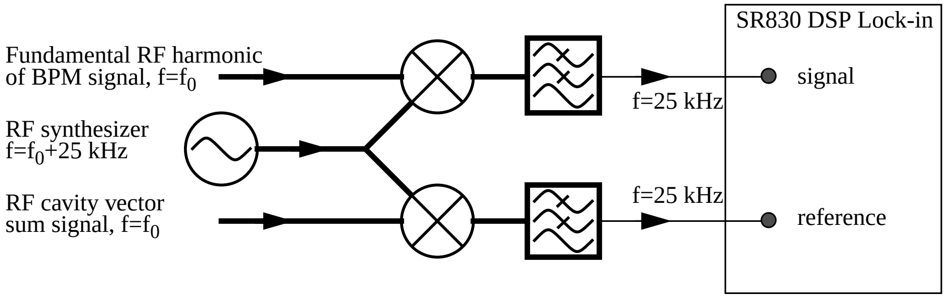

FIGURE 17. The principle of a synchronous phase measurement apparatus.

the higher frequency mixing products out. Since a bridge is implemented synthesizer frequency drift should not in the first order result in a phase error. Note that the total cost of this setup is a fraction of that for the vector voltmeter. Also, the system is rather flexible. Indeed, to switch to another RF frequency one needs to either reprogram the synthesizer or replace it when the frequency is substantially different. Also this setup can be used in other experiments which require phase measurement of RF signals of practically any frequency. For example, a similar approach was used in a home-made W-band vector network analyzer [61] where phase and amplitude of a 92 GHz signal were measured. Finally, filtering a beam signal at the fundamental harmonic can be hard for larger rings where a very high-Q RF filter may be needed. However, with this setup we can easily insert one more stage downmixing to some common frequency where appropriate off-the-shelf crystal filters are available.

3.3 Experimental details

In order to accurately measure the phase it is not enough to have a precise lock-in amplifier. Care has to be taken about other elements of the system as well as the machine conditions. Here we summarize our experience coming from the SLC measurements.

3.3.1 Input Cables

Typical electrical length change in cables runs from 150 PPM/°C (RG223) to ~6 PPM/°C (HELIAX). Therefore, a temperature drift during a measurement can significantly alter the result if the cable runs are long enough. In the SLC (~100 ft. of RG223) we found out that using a temperature stabilized cable significantly improves measurement reproducibility. Unfortunately, this cable was only available for part of the distance needed and also the temperature in the room with our setup was not fully controlled. This may explain our experience of better reproducibility when the measurements were taken at night so that the outside temperature did not change much.

3.3.2 BPM signal filter

To measure the phase correctly the input signal to the lock-in amplifier should not have significant amplitude modulation. Approximating a filter as an oscillator of a quality factor Q gives a requirement $Q/h \geq 1$, where h is the harmonic number. For the SLC damping rings (f_{RF}=714 MHz, h=84) we made a simple coaxial cavity filter with $Q \approx 300$.

3.3.3 Vector sum

EQ 2.75 includes the total accelerating voltage. To measure it the pickup voltages from the individual cells must be summed vectorially. This signal is available for the SLC since it is used in the so-called direct feedback loop [10].

3.3.4 Signal levels

The SR830 specifications require at least 200 $\mathrm{mV_{peak\text{-}peak}}$ (into 1 MΩ) reference arm input signal. We had to use an audio amplifier to bring the reference signal above this level. To make sure that the amplitude stayed constant we monitored it by a home-made RMS detector with the output connected to one of the auxiliary inputs of SR830. Related issue here is the isolation of the power splitter that divides the LO signal. We had to make sure that it is high enough so that the cavity signal does not leak through the coupler and does not significantly distort the beam signal or vice versa.

3.3.5 Beam lifetime and the lock-in averaging constant

To get a significant current decay the store should be comparable to the beam lifetime. There are simple ways of shortening the lifetime (with scrapers, transverse detuning etc.) to accelerate the measurement and reduce the temperature drift effect. However, the decay has to be rather smooth because rapid drops in the input signal to the lock-in amplifier may result in phase measurement error. In the SLC (lifetime on the order of ten minutes with no scraper) we tried the transverse detuning but could not make it smooth enough. We proceeded with our measurements using nominal lifetime stores. The data was sampled about every three seconds and the lock-in time averaging constant was set to one second. Shorter settings resulted in noisier data but did not lead to a different phase slope with the current.

3.3.6 Feedbacks

If the vector sum signal is properly derived then most feedback loops should not affect the measurement. For the SLC this is not true only for the S-band feedback that adjusts the beam phase for subsequent injection to the linac as well as for the direct feedback loop that effectively changes the cavity shunt impedance. These two feedbacks had to be turned off for our measurements.

4.0 Streak Camera

4.1 General Description

The most advanced and expensive instrument used for longitudinal beam dynamics studies in the SLC damping rings is the Hamamatsu model C3735 streak camera. SLAC owns a unique 500 ps resolution version of this camera called FESCA-500 which was custom-made for the short SLC linac beam. This streak camera allows single shot measurements of the longitudinal beam profile in the damping rings as well as at much more demanding conditions at the end of the SLC linac. Some of the parameters of this streak camera are listed in Table 2.

Streak tube model	N3373-02
Photocathode diameter	3 mm
Photocathode spectral response	200-900 nm
Phosphor screen diameter	15 mm
Micro-channel plate gain	>3000
Time resolution	<700 fs
Sweep rate	60, 200, 500 and 1200 ps/10 mm
Trigger jitter	< 30 ps
Streak trigger input signal	
Amplitude	+5-40 V in 50 Ω
Pulse width	2-100 ns
Maximum repetition rate	1 kHz
CCD head	
Number of pixels	1000 (hor.) by 1018 (vert.)
Pixel size	12 µm × 12 µm
Exposure time	10 ms - 1 hour
Spectral response	400-1000 nm
Cooling method	Thermoelectric air cooling
Frame readout time	4 s

TABLE 2. Some parameters of the streak camera and CCD.

Streak camera principle of operation is illustrated in Figure 18. The light pulse is collected at the horizontal input slit which is imaged onto the photocathode by the input optics. The photocathode converts the incident light pulse into a flux of electrons that mimics the light intensity distribution vs. time. This electron flux is accelerated by the accelerating mesh and then it passes through the deflection plates. When the electrons pass the plates they receive a high speed voltage ramp that results in a differential kick. Those in the center of the beam do not get any deflection while electrons in the head (tail) get deflected upwards (downwards). (Note, that these directions refer to

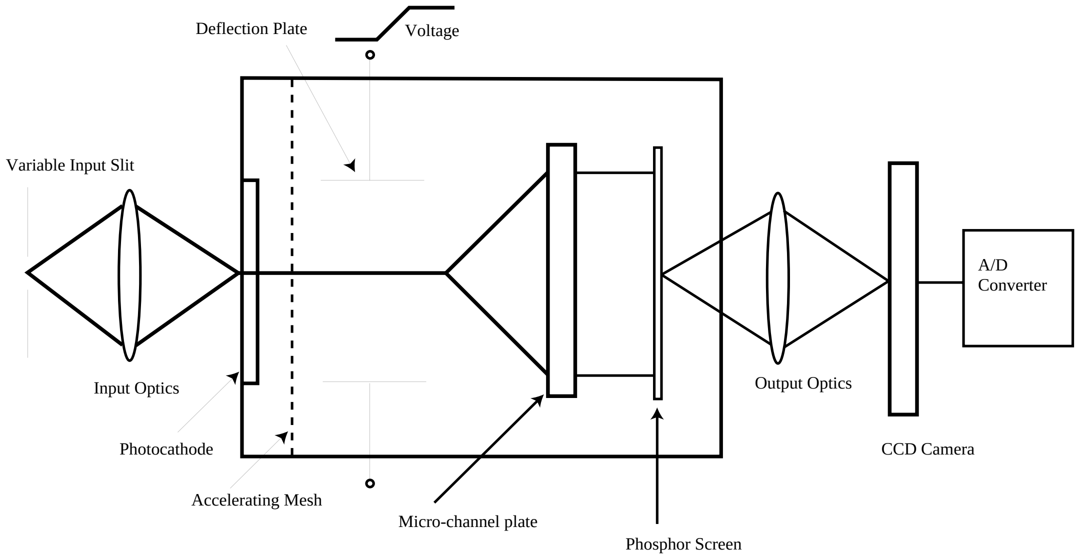

FIGURE 18. Streak camera component layout (from [6]).

Figure 18 and not to the actual streak camera where multiple plates are present and geometry is involved.) Subsequently, this deflected electron cloud hits the micro-channel plate (MCP) where the electron flux gets significantly amplified. MCP gain can be adjusted during the operation and it ranges from 3.3 to 6000 for our particular camera. Upon exiting the MCP electrons hit the phosphor screen causing it to emit light proportional to the electron flux intensity. Note, that the horizontal intensity distribution for this light is proportional to the intensity dependence vs. time for the initial light pulse that entered the streak camera. Similarly, the vertical distribution of the phosphor screen intensity mimics the initial pulse intensity variation along the input slit. The light emitted by the phosphor screen is imaged by the output optics onto the CCD camera attached directly behind the streak camera. The CCD camera digitizes the image so that it can be grabbed by a data acquisition module. Since, in many cases, the incoming light intensity variation along the slit has no value, the CCD may also be used to integrate the image along the vertical direction. The resulting horizontal image profile represents the longitudinal beam density and it may be recorded for further analysis.

The above description gives only a simplified picture. In fact, a great deal of effort comes into convincing oneself that the profile read off the CCD is a meaningful representation of the beam longitudinal charge distribution. As obvious from Figure 18, potential complications may include 1) input slit width contribution to the resolution, 2) dispersion in the input optics, 3) space charge effects distorting the shape of photoelectron bunches, 4) nonlinearities of the streak camera sweep, 5) possible saturation and/or nonuniform sensitivity of the photocathode, MCP, phosphor screen, or CCD, 6) noise generation by these elements, 7) need for extremely precise trigger. Some of these issues are addressed in the streak camera manual [15] while extensive studies and analysis of some others can be found in [6]. We should say that items 1) 2) 4) and 7) listed above are quite serious for the measurements at the end of the SLC linac where light intensity is low and bunches are as short as 0.6 mm. For the damping rings these problems are either non-existent or their solution is simple. On the other hand, in order to study longitudinally unstable beams additional aspects become relevant. They include acquisition of large amounts of high quality beam profiles, synchronizing this acquisition with the SLC control system, and, finally, processing the data to extract the varying features in the longitudinal density of unstable beams. In order to address these questions several modifications of the procedure of running the streak camera in the damping rings (as described in [6]) had to be implemented. This is the subject of the next section.

4.2 Techniques for running the streak camera

4.2.1 Cylindrical lens and other optics

Many streak camera and CCD components add some noise to the output image. One of the greatest contributors is the streak tube itself, which, similarly to other electron tube devices, possesses inherent shot noise problem. The relative intensity of this noise is proportional to $1/\sqrt{N_{ph}}$, where N_{ph} is the number of the photoelectrons emitted by the photocathode. Unfortunately, even if the input light intensity is not an issue, N_{ph} cannot be made very high. Apart from obvious considerations of photocathode saturation and general camera protection there is usually a lower intensity limitation associated with the space charge effects in the streak tube. Basically, the denser the cloud of photoelectrons is the stronger it blows up due to the Coulomb forces leading to effective lengthening of the output image. To alleviate this problem one should use a cylindrical rather than a spherical lens to focus light on the input slit. This spreads up the input light spot along a much wider area of the photocathode thereby reducing the space charge forces as well as the possibility of saturation or burn. For the damping ring experiments we used cylindrical lenses with the focal length of 50 mm.

Other input optics we used in the damping rings included 80 nm FWHM interference filter to reduce chromatic effects [6] as well as neutral density filters to adjust the intensity below the streak camera saturation levels. Input slit was usually set to 200 µm which, according to [6] and [15], should not give any appreciable distortion of the damping ring beam profile.

4.2.2 Camera gate settings

Depending on the speed set the streak camera system is supposed to record the variation in the incoming light that takes place in the time window 60 to 1200 ps wide. On the other hand, as it was mentioned earlier, many of the streak tube elements generate noise and some of this noise is generated continuously. This noise mainly comes from stray light hitting the input slit as well as from the dark currents of the photocathode and the MCP. The noise creates a problem, because the luminescence decay time of the phosphor screen (and integration time of the CCD) is in the sub-ms time scale. Therefore, the CCD can accept noise from a much wider time window than is covered by the incoming signal. In order to address this problem a special gating procedure is implemented in most streak cameras including FESCA-500. It involves special deflecting plates that are gated so that the photoelectrons can go through only within a short time interval close to the streak sweep. This procedure also implements some gating on the MCP that is kept at a reduced gain most of the time. Both the deflecting plate gate and the MCP gate occur very close to each other and will be further referred to as cutoff gate.

Specifically, FESCA-500 streak camera has three gate modes that differ in the timing and logical relationship between the incoming triggers, streak sweep, and the cutoff gate [15]. Although “Normal” mode is the simplest one to use since it does not require a pretrigger this mode results in a much noisier image than the other two modes. This is because in the “Normal” mode the cutoff gate is open most of the time. Therefore, any incoming light can generate photoelectrons that reach the microchannel plate and eventually end up recorded by the CCD. Since the damping ring revolution frequency is four orders of magnitude higher than the maximum trigger rate for the streak camera, any stored beam creates at least 10^4 parasitic synchrotron light pulses per each one recorded. Furthermore, even if external noise is significantly reduced (for example by using a light chopper as described in [6]), dark currents coming from the photocathode and the MCP still remain a problem.

The other two modes, “Gate A” and “Gate B”, are significantly less noisy. This is because the gate stays open during a very short (but controllable) period of time. Both of these modes use an extra trigger to open a cutoff gate and they differ in the logic of the gate closure. Mode B allows maximum flexibility since the gate timing and the streak sweep are independently controlled. This is the mode we used in most of our experiments. Detailed trigger timing for this mode is described in the next section.

4.2.3 Streak camera trigger setup

Independently of the gate mode used the streak camera requires the “main trigger” synchronized to the damping ring beam. It has to be a positive pulse 5 to 40 V high and 2 to 100 ns in duration. In addition, for the sweep rate of

200 ps/10 mm that we normally used in the damping rings, this trigger has to be rather stable on a 100 ps time scale. Since the typical streak camera experiment in the damping ring lasted several hours, both shot to shot trigger jitter and long term thermal drift were important. To derive the main trigger we used the one out of four (in each ring) dedicated streak camera TRBRs that cover the entire store. Timing adjustment of these triggers both in coarse 8.3 ns steps and also, for limited range, in 0.1 ns steps is possible through the SCP. Physically, these triggers come out of a VDU (variable delay unit) located in the corresponding kicker building. Interestingly, we observed that bypassing the VDU significantly reduces the trigger jitter. The drawback is that the fine timing adjustment through the SCP becomes unavailable. This, however, can be effectively dealt with by using a variable delay coaxial line (trombone). Finally, since all the control voltages in the SLC are in NIM standard, right before the streak camera trigger socket we had to reshape this trigger signal with a special NIM converter module.

Streak camera operation in “Gate B” requires a pretrigger that starts the tube gate. It has to arrive about 300 ns prior to the main trigger and last long enough to completely overlap with the main trigger. Since the pretrigger affects only the cutoff gate it does not require ps timing precision. For our damping ring experiments we usually derived the pretrigger from one of the standard triggers of the SLC timing system (i.e. gated camera trigger).

Finally, in our experiments we used C5050 module which is Hamamatsu manufactured GPIB interface for the CCD camera. Using this module makes the streak camera a regular GPIB device that can be interfaced to the SCP via correlation plot routine and TRYY trigger handshake as described in Section 2.3. In the damping rings we had to stretch the TRYY trigger to about 2 ms and then logically add it to the main trigger. Typical timing relationship between various triggers is shown in Figure 19.

Finding the beam without any prior knowledge always presents a challenge. To automate this procedure we used a 2 ns rise time photodiode (model

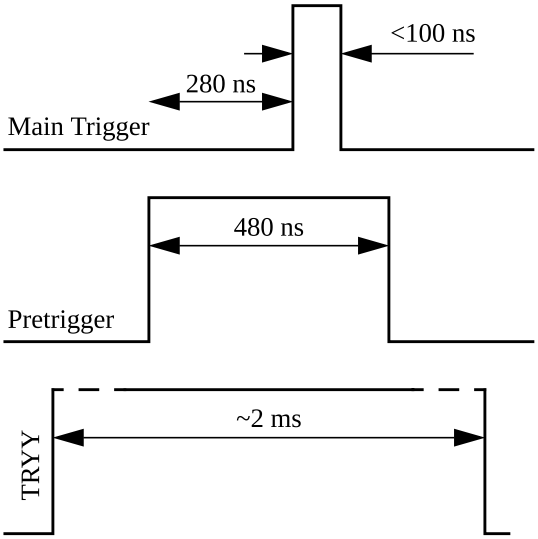

FIGURE 19. Streak camera timing.

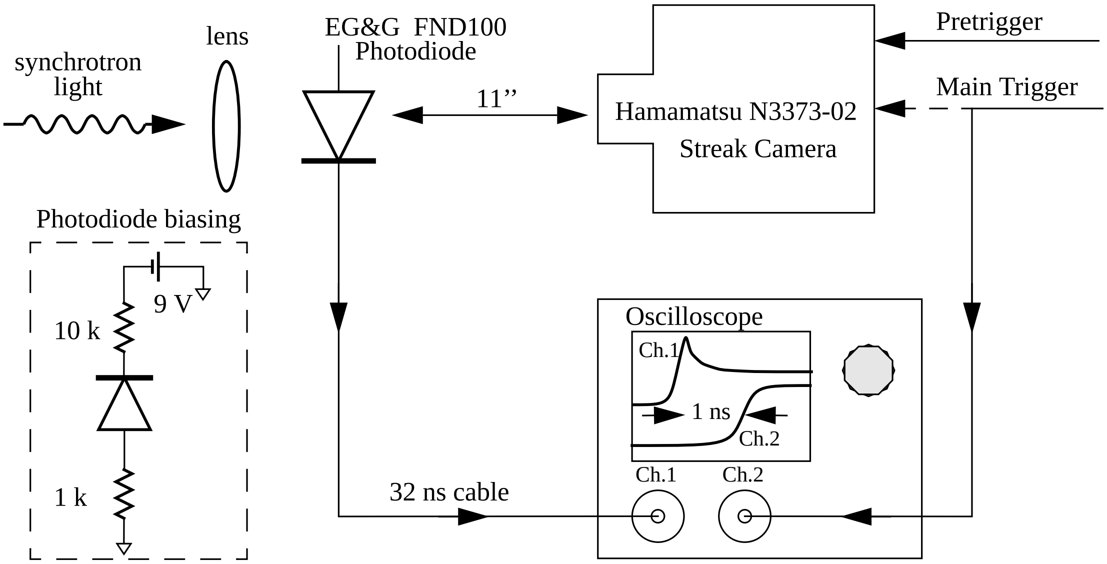

FIGURE 20. Finding the beam with a photodiode. Streak camera should be in Gate B mode and at the slowest streak speed.

FND-100 manufactured by EG&G). This photodiode was placed in the synchrotron light path before the streak camera and the light was focused on the active area of the diode. For a given distance between the photodiode and the streak camera the delay of the photodiode signal with respect to the main trigger defines the timing on a sub-ns scale. This allows quickly finding the beam on the slowest streak speed. Going to a faster speed should be done according to the Table 3.3.1 of reference [6]. Parameters for the setup we used are shown in Figure 20.

5.0 Detecting instability signals

5.1 Motivation

The easiest way to see the presence of the instability in the damping ring is by looking at the BPM signal spectrum near a high frequency revolution harmonic. One of such spectra is shown in Figure 21 (left). This spectrum was taken with an HP 50000 swept spectrum analyzer system and is averaged over many injection cycles. The frequency offset is given with respect to 9.77 GHz rotation harmonic seen in the center. Other features present in this plot are, first of all, broad lines displaced by about f_{s0} from the revolution harmonic. In the beginning of each store these lines are dominated by injection transients but after a ms or so into the store their residual amplitude presumably comes from the noise in the RF system. Also in the plot are narrower lines with much higher amplitude that are displaced slightly less than $2f_{s0}$ from the rotation line. These are the instability sidebands and they only appear above the threshold value of current. These instability sidebands

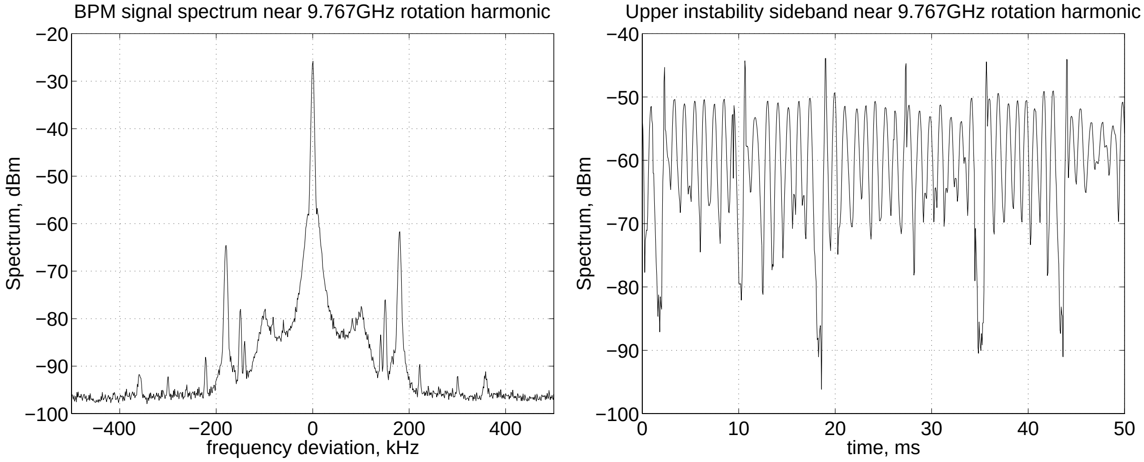

FIGURE 21. Typical spectrum analyzer traces.

sometimes have rather peculiar time dependence. They may blow up and damp down on a ms scale which is seen in the right of Figure 21. What is shown there is the spectrum analyzer trace vs. time when the spectrum analyzer was set as a receiver at the upper instability sideband frequency. One can clearly see roughly 20 dB oscillations in the instability sideband amplitude.

Although the spectrum analyzer gives a clear indication of the instability presence it does not allow drawing any quantitative conclusions regarding the instability. In addition, it does not provide any signal that can be easily correlated with other measurements performed throughout the SLC. This is because both the video output signal and the signal coming from the IF port have a significant (fraction of a ms) delay compared to the input.

Another problem studying the instability in the damping rings is unrelated to the spectrum analyzer. It has to do with a simple fact that during normal SLC operation there are two bunches circulating in either damping ring. Therefore, if a spectrum analyzer or other diagnostics is connected directly to a BPM they would sample the signals from both bunches. This is clearly a disadvantage when studying a single bunch phenomenon.

Before describing the ways of getting around these problems we will comment on the relation of instability sidebands to the coherent motion of the beam particles.

5.2 Longitudinal signals from a BPM

The qualitative features of the spectra seen in Figure 21 can be understood using a simple model that ignores the finite bandwidth of the BPM and the measurement apparatus. This section reproduces some results from [11].

5.2.1 Single particle motion

Consider a single unit charge particle that circulates around the ring with a revolution frequency ω_0. A BPM sitting at a fixed location in the ring would see this particle to arrive at multiples of a revolution period T_0. Ignoring the transverse oscillations (or alternatively assuming that we are sampling the sum signal from the two opposite BPM electrodes) we conclude that the BPM samples the beam current

$$I(t) = \sum_{n=-\infty}^{\infty} \delta(t - nT_0) \tag{3.4}$$

that has a spectrum given by

$$\tilde{I}(\omega) = \omega_0 \sum_{n=-\infty}^{\infty} \delta(\omega - n\omega_0). \tag{3.5}$$

This is an infinite comb of rotation harmonics.

Now assume that the charge executes synchrotron oscillations with amplitude a and phase φ. This leads to the modulation of its arrival time to the BPM which now samples the current

$$I(t) = \sum_{n=-\infty}^{\infty} \delta(t - nT_0 - a\cos(\omega_s nT_0 + \varphi)). \tag{3.6}$$

The spectral density of such current is given by

$$\tilde{I}(\omega) = \omega_0 \sum_{m=-\infty}^{\infty} (-i)^m J_m(\omega a) e^{-im\varphi} \sum_{n=-\infty}^{\infty} \delta(\omega + m\omega_s - n\omega_0), \tag{3.7}$$

where J_m is a Bessel function of order m. Note, that each line in the spectrum above has a phase factor $e^{-im\varphi}$ and thus contains information on the phase of the synchrotron oscillation.

In reality spectrum analyzers measure neither negative frequencies nor the phase. Therefore the physical spectrum one would see on a spectrum analyzer is obtained from EQ 3.7 by taking the absolute value and folding with respect to $\omega=0$. During such a procedure the phase information is lost.

The physical spectrum corresponding to EQ 3.7 is sketched in Figure 22. There are several new features in this spectrum compared to the one we

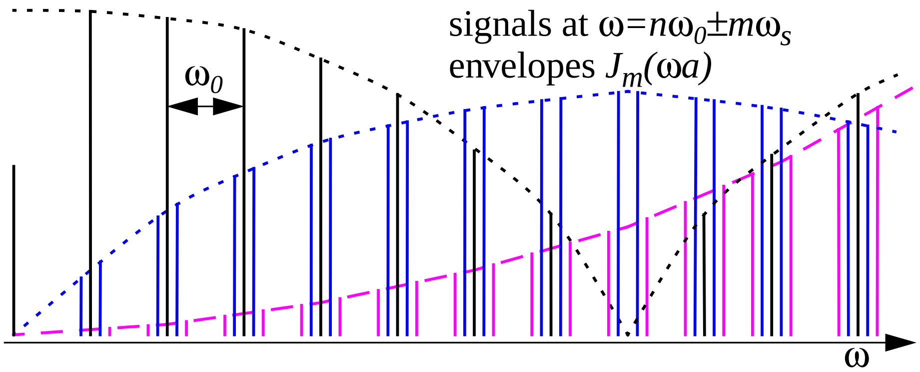

FIGURE 22. Idealized BPM signal spectrum for a single particle executing synchrotron oscillations. Only the first two sidebands are shown.

would obtain from EQ 3.5. First of all, the rotation harmonics are no longer of the same height. Instead they are modulated with an envelope function $J_0(\omega a)$. Second, the rotation harmonics acquire sidebands displaced from them by multiples of ω_s. Each set of sidebands is also modulated by an envelope function $J_m(\omega a)$ where the index m corresponds to the sideband order ($m=1$ for dipole, $m=2$ for quadrupole etc.).

Bessel functions achieve their first maximum when the argument roughly equals to the index. Therefore, a significant amplitude signal at the m-th sideband occurs at a frequency $\omega\sim m/a$. This tends to be rather high for short electron bunches as the sideband order goes up.

5.2.2 Incoherent oscillations

A beam in a storage ring is not a single particle but rather a collection of particles that are generally distributed in phases, amplitudes and frequencies of their synchrotron oscillations. If there is no coherent motion within a beam the phases of individual particles are independent. Therefore, averaging EQ 3.7 over φ we conclude that the resulting spectrum has only rotation harmonics (Figure 23). The envelope function in this case is given by a Bessel function $J_0(\omega a)$ folded with the particle distribution over the amplitudes of synchrotron oscillations $\rho_0(a)$.

For example, when the latter is Gaussian $\rho_0 \propto \exp\left(-\frac{1}{2}a^2/\sigma^2\right)$ the envelope function is also Gaussian $\propto \exp(-\omega^2\sigma^2/2)$ with characteristic folding (angular) frequency equal to inverse bunch length (in units of time).

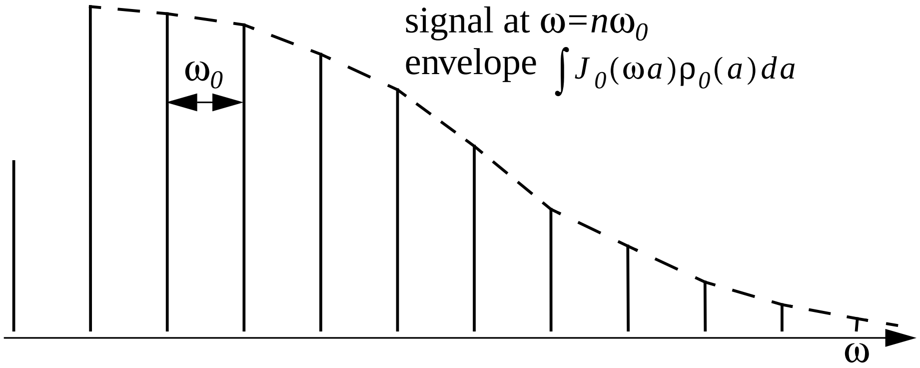

FIGURE 23. BPM spectrum when there is no coherent motion within a bunch.

5.2.3 Coherent motion

Now assume that a coherent azimuthal mode of periodicity m is excited within a beam. Similar to EQ 2.67 the beam density in phase space can be represented as

$$\rho(a, \varphi, t) = \rho_0(a) + \rho_m(a)\exp(i\Omega t - im\varphi), \tag{3.8}$$

where we assumed $a \propto \sqrt{J}\cos(\varphi)$ and neglected higher order terms.

The resulting spectrum is obtained by averaging EQ 3.7 with this distribution. It is clear that in this case the averaging over phases eliminates all the sidebands except for the m-th for which the oscillatory term in EQ 3.7 vanishes. Therefore, rotation harmonics in the resulting spectrum have m-th order sidebands. It is also clear that in the likely case of an amplitude distribution $\rho_m(a)$ having a maximum somewhere within several σ, the envelope function would peak up in amplitude at angular frequencies around m/σ.

For illustration we draw a cartoon picture of a quadrupole mode excited in the beam phase space and the corresponding spectrum we would see on the spectrum analyzer (Figure 24). Note, that similar to the single particle case, if it was not for the phase averaging, the phase of each sideband would represent the instantaneous phase space orientation of the quadrupole structure.

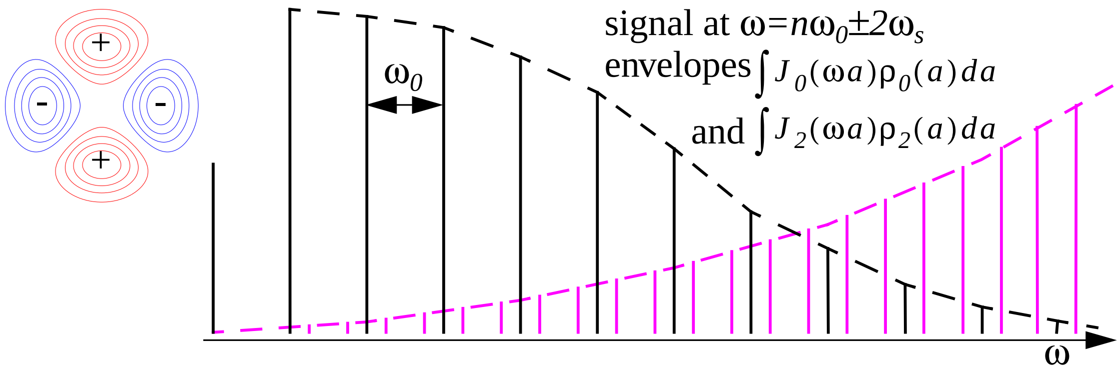

FIGURE 24. Quadrupole mode in phase space and resulting BPM spectrum.

5.2.4 Conclusions

The consideration above leads us to the following conclusions

- The bulk of the BPM signal power comes in rotation harmonics with frequencies less that $1/\sigma$.
- m-th sideband in the spectrum suggests a collective mode with m-fold azimuthal symmetry.
- To observe m-th sideband one has to go to rather high frequency $\omega \sim m/\sigma$.
- Before the phase averaging the spectrum completely describes the beam phase space. Radial structure is in the envelope function while the azimuthal orientation is in the phase of any of the sidebands.

The last conclusion assumes that the spectrum is available over very large bandwidth. In reality, as we discussed in Section 1.3.1 the bandwidth available is quite limited and for the damping rings is comparable to the inverse bunch length. Furthermore, even within that bandwidth extracting the envelope information is difficult because the response is dominated by the BPM response and the cable transmission (see Figure 14). On the other hand, extracting the instability phase or relative amplitude does not require very large bandwidth and is not compromised by unknown response functions. The implementation of this is discussed in the following section.

5.3 Detector circuit

5.3.1 General idea and the layout

The conclusions above tell us that the instability phase information is contained in the corresponding sidebands to the high frequency revolution harmonics. It could be demodulated from these sidebands by downmixing the corresponding rotation harmonic to DC and subsequently filtering out the DC component. Another approach is to use a square law detector which is schematically illustrated in Figure 25. The advantage of this approach is that the signal at the instability frequency f_{inst} results from all the instability sidebands to all the rotation harmonics within the bandwidth of the detector.

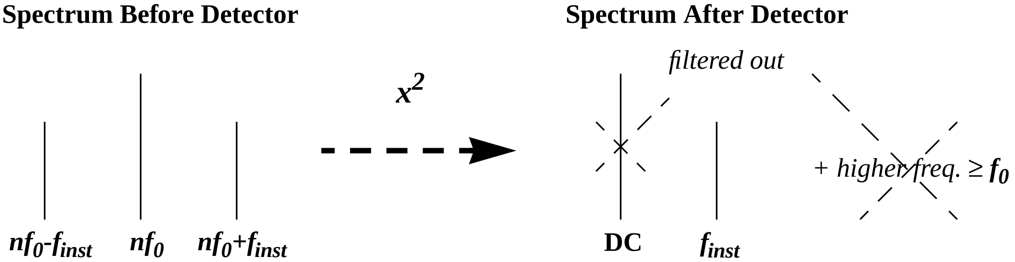

FIGURE 25. Detecting the instability with a square law detector.

Adding some extra elements to separate the signals between the two bunches we have implemented the following circuit.

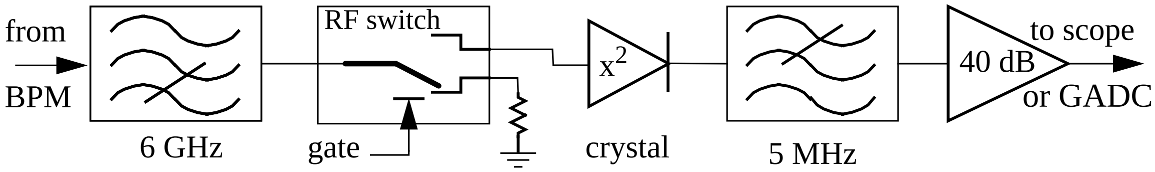

FIGURE 26. The setup to detect instability signals.

The front end high pass filter eliminates the bulk of the RF power that does not contain the instability information. Now the signal level is acceptable for the fast RF switch immediately after the filter. This switch is gated at f_0=8.5 MHz, and the gate delay is adjusted so that the output has only a signal from one of the two bunches in the ring. The detector demodulates the instability signal from the sidebands to the rotation harmonics as described above. Finally, the output of the detector is connected to the amplifier (no gain at DC) through a low pass filter that removes higher frequency mixing products.

The oscilloscope trace of the resulting signal is shown in Figure 27.

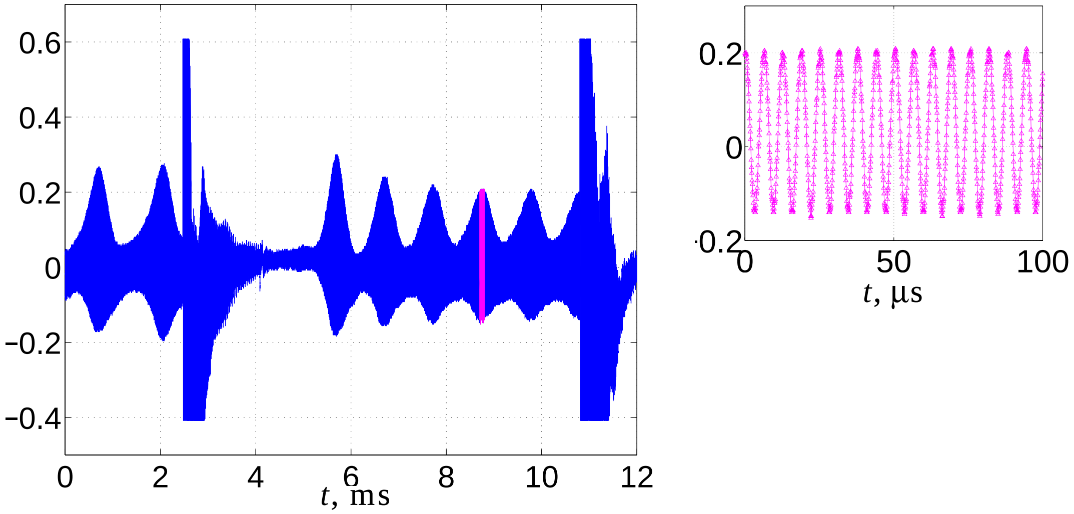

FIGURE 27. Detected instability signal (left) and a zoomed out portion. Two largest spikes indicate injection and extraction.

Note, that in addition to the slowly varying envelope (similar to the one we would see with a spectrum analyzer set to a zero span) the resulting signal includes the instability phase information (Figure 27, right).

5.3.2 Microwave components

Parameters for the two most important circuit elements are shown in Table 3. We have used both double throw reflective and single throw absorptive RF switches. Both of these present a matched impedance to the input independently of the gate applied. The advantage of the double throw switch is that the signals on two different ports come from different bunches stored in the ring (this assumes 50% duty cycle gate and also that two bunches are opposite to each other). This allows duplication of the circuit shown to the right of the RF switch in Figure 26 on the second port (shown terminated) and then simultaneously observing the instability signals from both bunches. This would show any cross-talk between the bunches. On the other hand, for continuous monitoring of the level of instability signals the cheaper SPST switch works fine as well.

	WJ-MSE203	**MITEQ-S138B**	**ACTP-1506N**
Type	SPDT PIN Diode Reflective	SPST PIN Diode Absorptive	Square Law Detector
Bandwidth	2-18 GHz	2-18 GHz	8-18 GHz
Switching time	25 ns	20 ns	N/A
Isolation	~60 dB	80 dB	N/A
Video bandwidth	N/A	N/A	2 MHz

TABLE 3. RF switch and crystal detector specifications.

Assuming σ=22 ps high current bunch length gives the optimum frequencies for detecting the dipole, quadrupole and sextupole instability modes at 7, 14 and 21 GHz respectively. The frequencies are quite high and as evident from earlier discussion and Figure 14 the sextupole mode is probably the highest that can be detected with the available BPMs and cabling. This is why there was no need to push the upper frequency limit of the RF part of the circuit much higher that 20 GHz. We ended up with off-the-shelf components with standard upper frequency value at 18 GHz. The rest of this section describes the key requirements for the individual components.

As mentioned earlier the purpose of the high pass filter is rather simple, namely to bring down the total RF power delivered to the switch without significant attenuation in the high frequency signal component. Ideally, the filter should do so while preserving the time structure of the incoming signal. Of course, real world filters have some amount of dispersion or frequency dependent delay and complete preservation is impossible. The highest group delay usually occurs in the transition area from the stopband to the passband; the sharper the transition the larger the delay. This is why for our application where unwanted signal component is significantly separated in frequency it was possible to pick a filter (model 4HS-5.5G-S11 manufactured by REACTEL, INC) so that the transition from the stopband to passband was relatively smooth resulting in lower dispersion. This brought down significantly the time overlap between the signals from the two bunches at the output of the filter. Furthermore, for our filter the transition region was located low enough in frequency where the instability sidebands were small. In addition, the filter transmission in the passband was essentially constant resulting in a flat group delay there. As evident from Figure 25 in this case the time overlap between the bunches introduced by the filter affected only the DC component of the detected signal and not the component at the instability frequency f_{inst} we were after.

For the RF switch used in this application the switching time is of crucial importance. The bunches in the electron ring are separated by only 56 ns (59 in SDR) and this should accommodate the switching time including the contribution from the finite rise times of the gate plus the window where the actual beam signal is present. The length of the latter is typically a few ns and it is defined by the amount of dispersion in the front end. As evident from Table 3 there is not much time left. Fortunately, as we have seen in our laboratory tests, the switching time specifications given by the manufacturers are very conservative. Nevertheless the timing of the switch gate is not trivial and has to be done with care. The details of the gating are described in Section 5.3.3.

Isolation specification defines the maximum leakage from the input to the output when the gate is closed. For our application poor isolation would mean getting a significant signal component from the other bunch. According to Table 3 the isolation for both switches we used is more than adequate. We expect that if there was a small signal leakage from the other bunch it was due to the dispersion in the high pass filter rather than imperfect isolation in the switch.

Finally, the two major requirements for the square law detector are for it to be sufficiently wideband (both RF and video bandwidth) and sensitive. The detector we used from the Advanced Control Components had an adequate RF and video bandwidths. The latter was in fact as high as 2 MHz and subsequent amplifiers usually had at least 500 kHz bandwidth. Therefore, our ability to detect higher order instability sidebands was limited solely by the bandwidth of the incoming signal and to lower extent by the RF bandwidths of the components shown in Figure 26.

5.3.3 Deriving the gate for the RF switch.

Surprisingly there is no 8.5 MHz timing system signal in the vicinity of the damping rings that could be used to gate the RF switch. The closest place where 8.5 MHz signal is generated is the injector [71]. Unfortunately, although damping ring bunches are locked to this signal during any injection cycle, due to some intricate details of the SLC timing system there is a 180° switch in the lock from one store to the next. Therefore, if we derive a gate off of this signal in the electron damping ring then we would get a production or scavenger beam signal on alternating stores.

This is why for our studies we have exclusively used beam derived gate generated as illustrated in Figure 28 for the positron ring. First, the two bunch clock is derived using a discriminator on the low frequency BPM signal. Subsequently, a veto is applied to this clock so that it becomes effectively locked to the bunch to be extracted. Such a gate proved to be robust and convenient. The only problem with this way of gating the RF switch is that the gate can slip somewhat in time when there are significant variations of the beam intensity.

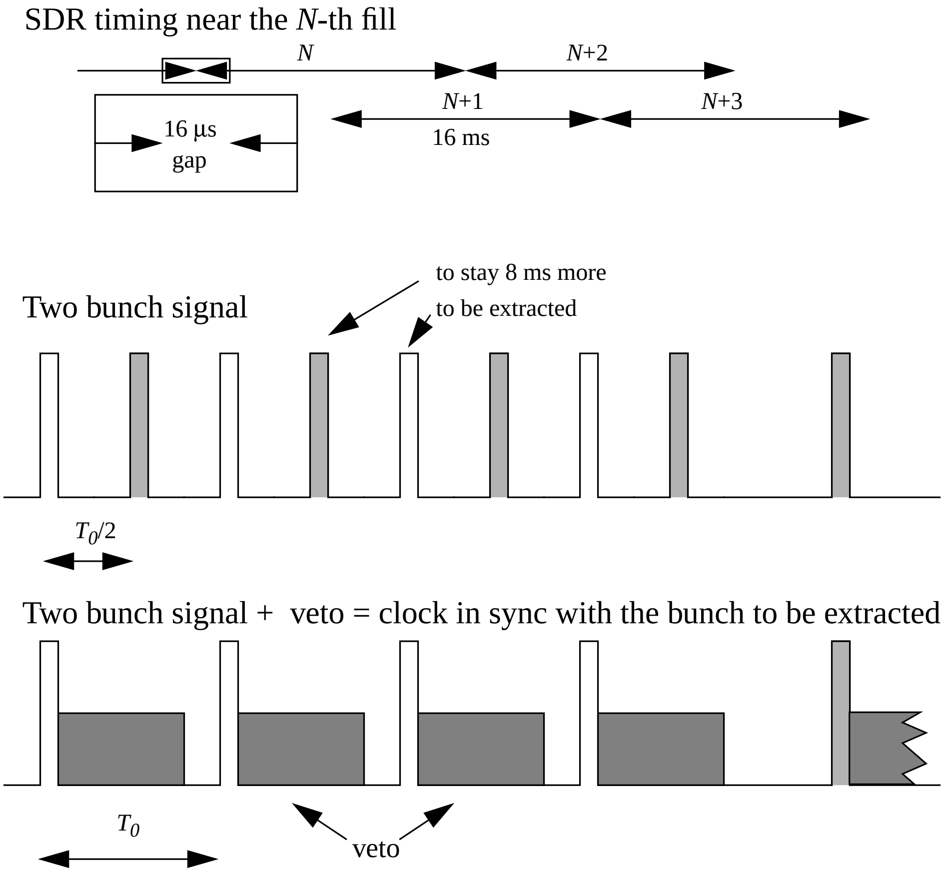

FIGURE 28. Deriving beam-based gate in SDR.

The optimal delay and width of such a gate at the control port of the switch had to be determined experimentally. The easiest way to do this is by running a single bunch in the ring. In this case we start with 50% duty cycle gate (59 ns pulse width) and find the delay setting that maximizes the amplitude of any rotation line within the switch bandwidth. Subsequently, we shorten the gate width until the amplitude of the rotation line starts decreasing. For best results 2-3 iterations of this procedure should be repeated. We have found that the optimum gate width is around 40 ns which is the value we have usually used in our measurements. The only exception is the measurement of the cross-talk between the two bunches in the positron ring where we had to settle for a 50% duty cycle.

Unfortunately single bunch conditions are rarely available. This is why to find the best delay setting we often used a different method that does not require single bunch running. In the positron ring this procedure is especially simple due to the symmetry of the fill. The latter leads to an alternating pattern in the rotation lines of the BPM spectrum with even harmonics significantly suppressed as shown in the top plot of Figure 29. Therefore, for getting a single bunch signal from the switch the gate delay has to be adjusted to minimize the signal at any even rotation harmonic. If the delay is chosen properly the amplitudes of the adjacent rotation harmonics equalize as shown in the bottom plot of Figure 29. Note, that at frequencies this high the interference from the switch gate feedthrough is negligible.

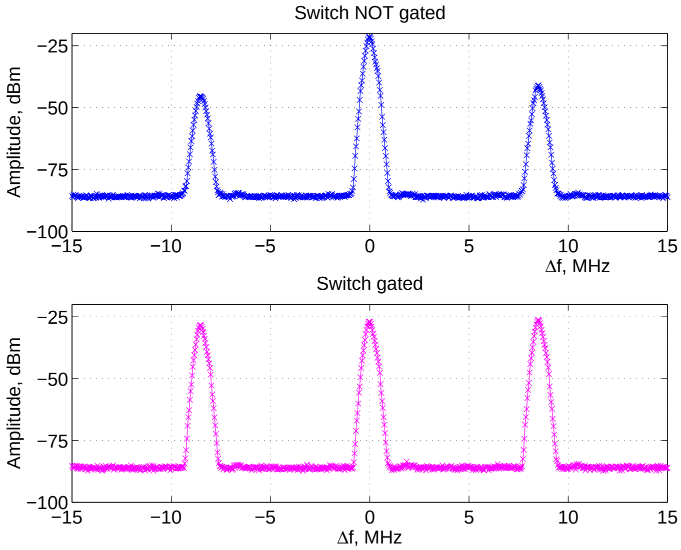

FIGURE 29. SDR BPM signals near 9.76 GHz rotation harmonic.

Similarly, this procedure can be done in the electron damping ring except the rotation line has to be chosen accordingly. For the NDR fill pattern the beating of the envelopes of the rotation harmonics from different bunches cancels out at frequencies that are multiples of 21 times the rotation frequency. Therefore, at the optimal gate delay setting the amplitude at any of these rotation lines should be at a maximum. We have usually used the 1113th revolution harmonic to adjust the gate delay in the NDR.

Finally, we should comment that BPM spectra taken before and after putting the gate on the RF switch allow to estimate how well the signals from the two bunches are isolated. For example, from the amplitudes of rotation lines in Figure 29 we can estimate that the isolation exceeds 25 dB.

Chapter 4

Experimental results

1.0 Synchronous phase measurement [56]

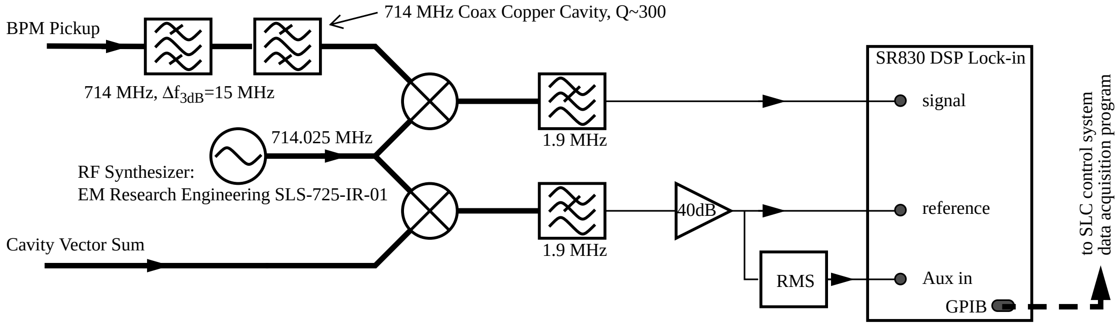

FIGURE 30. Synchronous phase measurement setup.

The measurements we describe here were done in the positron damping ring. Similar results were later obtained in the electron damping ring as well. The setup we used is shown schematically in Figure 30. Single beam stores were done at different values of accelerating voltage clustered near 600 kV, 800 kV and 900 kV. The total beam charge was 1 to 1.5×10^{10} ppb at the beginning of each store, which is below the instability threshold. The stores lasted ten to fifteen minutes, so that the current could decay roughly a factor of two (Figure 31 a). For such a measurement many systematic errors could show up as a linear change of phase with time. Since this could hide real effects, we did several measurements at every value of accelerating voltage. The total number of stores we did was seventeen.

For each store we were recording some of the RF system parameters as well as the beam current. Simultaneously we sampled five values with the lock-in amplifier namely the lock status bit, reference arm amplitude, refer-

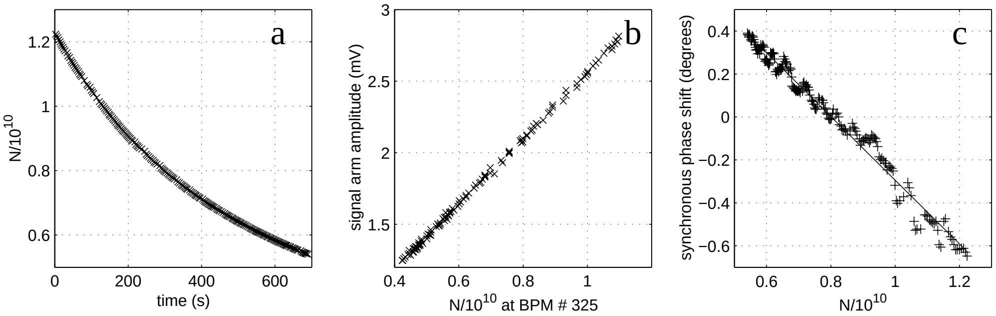

FIGURE 31. Synchronous phase measurement data.

ence arm frequency, signal arm amplitude and signal arm phase. All but the last were recorded for diagnostic purposes to ensure solid lock to the external reference with stable frequency and amplitude. The signal arm amplitude was proportional to the beam current (Figure 31 b) which argues that the signal was largely beam induced. The phase shift measured by the lock-in was the actual synchronous phase shift and as expected it turned out to be linear with the beam current (Figure 31 c). The phase shift slope with current substituted in EQ 2.76 allowed us to extract the value for the loss factor. The results for seventeen stores at different gap voltages are shown in Figure 32 which plots the scaled loss factor vs. accelerating voltage. The results from each store are plotted with the statistical error of the fit (diamonds). Also plotted are the mean values within each group (squares) with their errors derived from the rms spread of the individual stores.

There appears to be an insignificant slope with respect to the voltage which may indicate some deviation from the short bunch approximation made in EQ 2.78 or from the low current assumption $\sigma^2 \propto V_{RF}$; alternatively it may be caused by some systematic error. Ignoring this slope and using $\sigma^2 \propto V_{RF}$ dependence we found the average nominal value for the loss factor k_0=17 V/pC±15% which corresponds to about 1 kΩ resistive component in the longitudinal impedance. This measured value is in good agreement with calculations [51] discussed in Section 1.2 of Chapter 3. The error quoted is an estimate. It is dominated by the uncertainty in absolute values of accelerating voltage; the error in the mean from the data points in Figure 32 is less than 3%. It is also possible to estimate the loss factor for a given accelerating voltage without making any assumptions on bunch length scaling. For example, for V_{RF}=790 kV the loss factor $k_{790\mathrm{kV}}$=17 V/pC±17% which is also consistent with calculations [51].

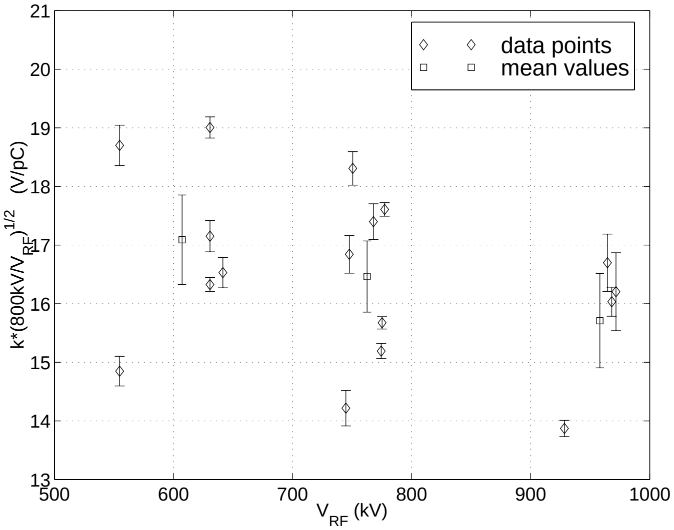

FIGURE 32. Synchronous phase measurement results.

2.0 Low current bunch shape measurements

The synchronous phase measurement gives an estimate of the resistive component of the impedance because the latter causes the bunch centroid to shift with respect to the RF wave. Similarly, since the impedance causes the potential well distortion that makes the bunch shape deviate from a Gaussian we expect that bunch shape measurements should give some insight on the magnitude of the impedance.

Utilizing the streak camera we have performed a series of a low current bunch shape measurements in the positron damping ring. The ring operated at the nominal 120 Hz SLC injection cycle with two bunches stored. Streak camera profiles were taken roughly a half ms before the extraction. We have recorded 9 batches of data files with each batch (9 to 13 files long) corresponding to a different value of the RF voltage ranging from 510 to 940 kV. The data were taken at two settings for the beam current, namely 8×10^9 and 1.5×10^{10} ppb and we have specifically checked the instability was not present at any value of the RF voltage.

During the processing phase we generated the average bunch shape for each batch. This shape was subsequently fitted with the Haissinski distribution for 5 different impedance models a) zero impedance, b) $Z(\omega) = R$, c) $Z(\omega) = R - i\omega L_0$ where $L_0 = 6$ nH was taken from reference [51], d) $Z(\omega) = R - i\omega L$ and e) calculated wake function from reference [50]. We used simple least square method that minimized the squared deviation between the average shape and a numerically generated Haissinski solution. For each type of fit we fitted the centroid position and the amplitude scale factor. Fits b) and c) had the value of R as a fit parameter and fit d) had both R and L values fitted. The results of the fits b) c) and d) are shown in Table 4.

	$Z(\omega) = R$	$Z(\omega) = R - i\omega L_0$	$Z(\omega) = R - i\omega L$	
			R	L
Average value	1072	1038	1067	-1
Error in the mean	138	131	139	2

TABLE 4. Fit results (in Ω and nH) for different impedance models.

The first row shows the average value of the impedance parameter fitted and the second row shows the error in the mean (standard deviation divided by $\sqrt{8}$).

The resistance values obtained are consistent between the various models used. However, as indicated by the second column, the spread in the impedance values between the batches is quite high. This is further illustrated in Figure 33 where the results for fit d) are shown for each of the 9 batches.

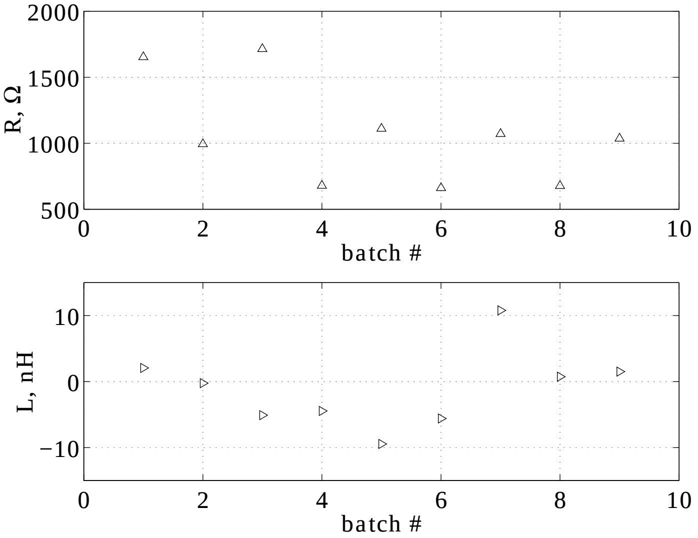

FIGURE 33. Fitted values of *R* and *L* for fit d).

The variation in R and even larger spread in L is not surprising. It is a consequence that this method of impedance measurement has a low sensitivity to the impedance parameters. Indeed, the impedance information is contained not in the beam profile as a whole but rather in the deviation of the profile from the low current Gaussian shape. In the case we are dealing with these

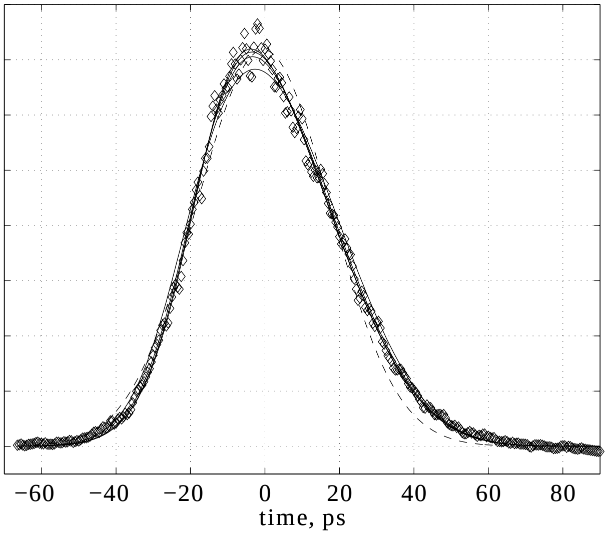

FIGURE 34. Average beam profile (symbols) and fitted shapes a) (dash) and b) through e) (solid); N=1.5×10^{10}, V_{RF}=790 kV.

deviations are rather small as seen from Figure 34 where the average shape for one of the batches is shown together with all the fits a) through e).

When the deviation is comparable to the measurement errors there tends to be a large spread in the values obtained. This is somewhat inferior to the synchronous phase shift measurement where the measured value is directly proportional to the resistive component of the impedance. Therefore, at least for the measurement of the resistive component, we conclude that the bunch shape measurement should be considered supplementary to other techniques.

Nevertheless, our data allows us to draw the following conclusions.

- The resistive component of the vacuum chamber at the characteristic bunch frequency is R=1 kΩ ± 130 Ω. The error quoted only includes the error in the mean.
- The inductive component is likely to be less that 10 nH.
- Our data is consistent with the wake function model from reference [50]. However, the measurement accuracy is inadequate to distinguish between this and other models we used.

3.0 Network analyzer measurements

As it was mentioned in Chapter 2 the impedance of the vacuum chamber causes the synchrotron frequency to shift with intensity. The measurement of this effect in principle allows estimation of the magnitude of the characteristic inductive component of the ring impedance. Below the instability threshold bunches do not broadcast any signal. Because of that, in order to observe the synchrotron motion beams have to be excited externally. In the longitudinal case this can be done by small modulation of the RF voltage. Phase modulating the RF makes the beam oscillate as a whole (rigid dipole mode). In that case it moves with its own potential well and the frequency of this motion does not shift with intensity and equals f_{s0}. On the other hand, amplitude modulation of the RF excites the bunch length oscillations with characteristic frequency $2f_s(N)$.

The excitation is usually done with either broad-band noise sources or swept narrow-band sources. We have opted of the latter and used a network analyzer to measure both the amplitude and phase responses of the beam as a function of frequency. Such a measurement is commonly referred in literature as a beam transfer function measurement (e.g. [3]).

The setup that we used in the positron damping ring for the amplitude modulation case is sketched in Figure 35. For the case of phase modulation the variable attenuator in this schematic should be replaced by a fast phase shifter.

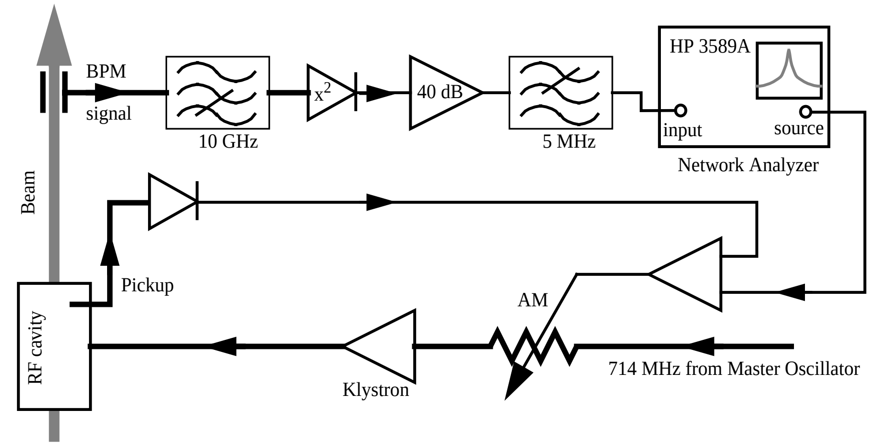

FIGURE 35. Beam transfer function measurement setup (amplitude modulation case).

The setup is similar to the one described in the reference [62] except at the receiver end we used the detecting circuit described earlier which allowed us to greatly increase the sensitivity. We used the HP 3589A network analyzer which was interfaced to the SCP through the GPIB port.

This measurement was done running single bunch stores in the positron damping ring. The SCP readout for the RF voltage was 860 kV and the instability threshold was about 1.5×10^{10} ppb. The current was allowed to decay from ~2×10^{10} down to ~3×10^9 ppb which typically took about 20 minutes. The network analyzer sweep time was roughly 2 sec.

The measurement results for both phase and amplitude modulation are shown below.

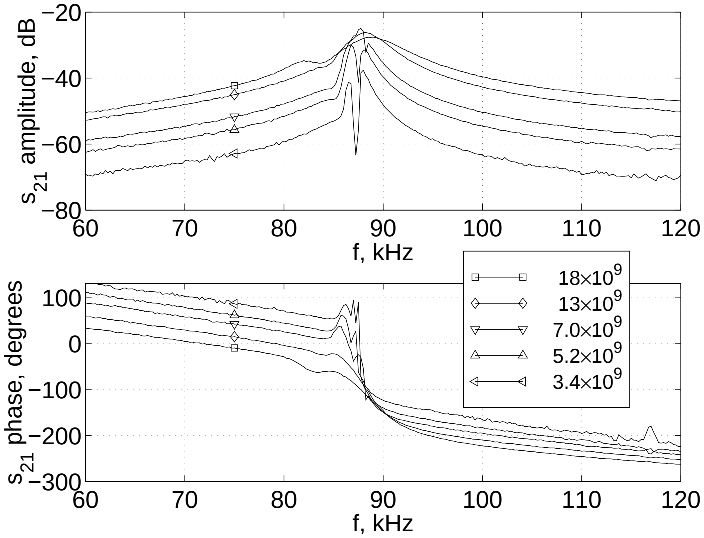

FIGURE 36. Beam transfer function measurement for phase modulation. To avoid overlap an arbitrary phase shift is introduced between the phase curves.

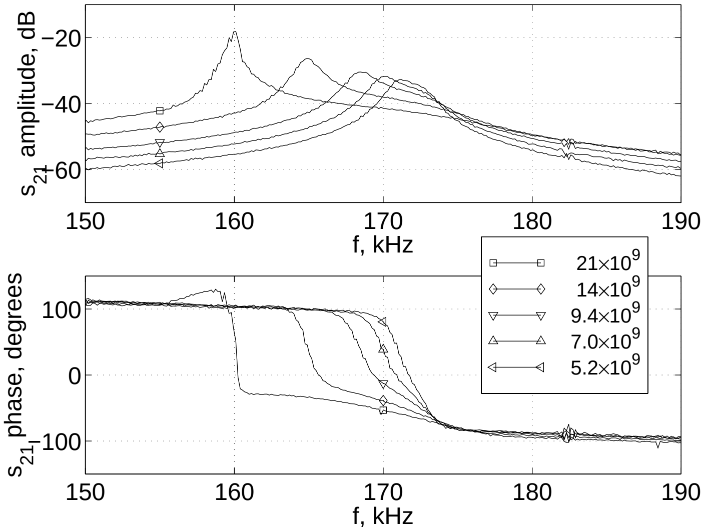

FIGURE 37. Beam transfer function measurement for amplitude modulation.

As expected, for phase modulation there is almost no change in the center frequency of the beam response as current decays. This gives the value for f_{s0}=87 kHz. In addition, there are several qualitative features seen in both amplitude and phase response curves. First of all, there is a characteristic split in the center of the amplitude response function. It comes from the cancellation of the dipole moments of particles in the core of the bunch and those trapped in the separatrix of the nonlinear resonance. This effect was first reported in [62] and later investigated in more detail in [63]. Other features include a slight depression in both amplitude and phase responses above the instability threshold.

For the amplitude modulation case the difference between the traces taken above and below the instability threshold is more dramatic. The amplitude response peaks out much sharper for currents above the threshold while the phase response has a characteristic bump at frequencies just below the resonance. Note, that for clarity only one curve taken above the instability threshold is shown in Figure 37. In reality, for this particular store roughly 25 more traces were taken above the threshold and they all have the bump present (It gets smaller as current decays). In addition, this feature was reproducible from store to store. While we do not have a quantitative explanation that describes this bump we note that a similar feature may appear in a driven response of a nonlinear oscillator.

Another feature seen in Figure 37 is a shoulder above the resonance frequency that becomes narrower as the current decays. This shoulder presumably comes from the frequency spread of individual particles within a bunch. The amount of this spread is comparable to that shown in Figure 12 at corresponding intensity.

Finally, in Figure 38 we plot the center frequency of the beam response (defined by the maximum phase slope) from the amplitude modulation measurement.

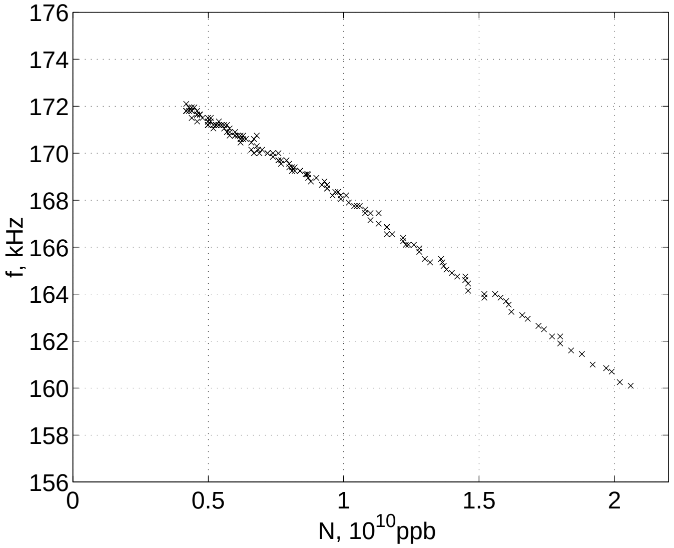

FIGURE 38. Center frequency of the beam response from the amplitude modulation measurement.

The dependence is almost linear and at zero current it extrapolates to two times f_{s0}.

The results from the driven excitation measurements can be summarized as follows

- The synchrotron frequency shift below the threshold was measured to be 7 kHz/10^{10} ppb at the zero current synchrotron frequency f_{s0}=87 kHz. This is roughly consistent with the wake function from reference [50] discussed in more detail in Section 1.2 of Chapter 3.
- There is no significant change in the dependence $f_s(N)$ above the instability threshold. In other words the instability frequency extrapolates to $2f_{s0}$ when N goes to zero.
- There is a characteristic bump upwards in the phase of the beam response above the instability threshold.

4.0 High current stored beam experiments

The purpose of the experiments to be described in this section was to study the instability behavior under the broad range of stored beam parameters namely the current and accelerating voltage. In this section we report the results of a series of such experiments performed in the positron damping ring. Qualitatively similar results were obtained at a different time in the electron ring. However, since the positron ring studies were much more detailed we chose to present the positron ring results alone.

4.1 Setup

As described in Section 5.0 of Chapter 3 the simplest diagnostic for the instability is a spectrum analyzer connected to a BPM electrode. It allows, for instance, accurate measurements of the instability sideband frequency or amplitude as a function of stored beam current. Alternatively, when set as a receiver to the sideband frequency the spectrum analyzer shows a characteristic ms time scale bursting behavior that may occur at certain values of current. However, studying such behavior with a spectrum analyzer is not convenient for longer stores when the instability sideband frequency changes as the stored charge decreases. A more convenient way to do that is to utilize the instability signal detector described earlier. To obtain the maximum amount of information we decided to perform both measurements simultaneously utilizing the setup shown below.

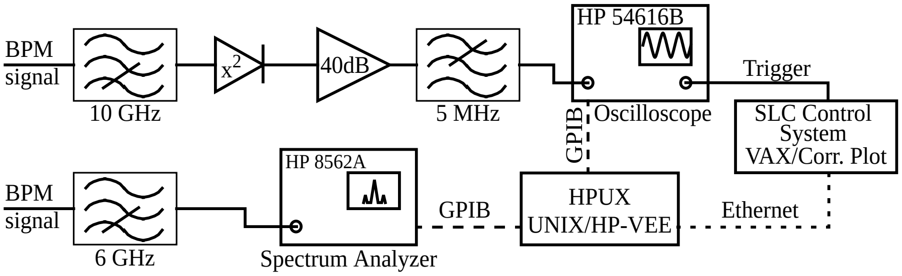

FIGURE 39. Stored beam experiment setup in SDR.

As shown in Figure 39 BPM signals were simultaneously measured with a spectrum analyzer and a digitizing oscilloscope that was connected after the detecting circuit described in Section 5.3 of Chapter 3. Since this experiment was done with a single bunch the RF switch was not used. During our experiments the major settings were as follows. The central frequency of the spectrum analyzer was set to the 1149th revolution harmonic which is roughly 9.77 GHz. The span was 500 kHz, and the resolution and video bandwidths were 1 kHz. This results in a sweep time of 2 s and, moreover, two subsequent sweeps were video averaged. The oscilloscope was AC coupled. It was set to 1 ms/div and the trace length was 2000 points.

The oscilloscope and the spectrum analyzer were interfaced to the SLC control system via the correlation plot routine as described in Section 2.3 of Chapter 3. The oscilloscope was triggered by a TRYY trigger while the spectrum analyzer was free running but the HP-VEE program guaranteed that the data was acquired synchronously with the oscilloscope trace. The data taking rate was a fraction of a Hz which was adequate for a beam lifetime of several minutes.

In the course of our measurements several dozen beam stores at various accelerating voltages were recorded. Each store lasted about seven minutes; this allowed the initial beam current of $\sim 3.4\times 10^{10}$ ppb to decay roughly a factor of two to a value below the instability threshold.

4.2 Measurement results: instability properties vs. current [64]

In this section we will illustrate some of the most interesting aspects of our measurements using the data for the RF voltage of V_{RF}=690 kV as determined from the measured synchrotron frequency (see Section 4.3.1).

The typical spectrum analyzer sweep when the quadrupole mode of the instability is present is shown in Figure 40. One can clearly see the instability sidebands to the revolution harmonic displaced by about 160 kHz. This is

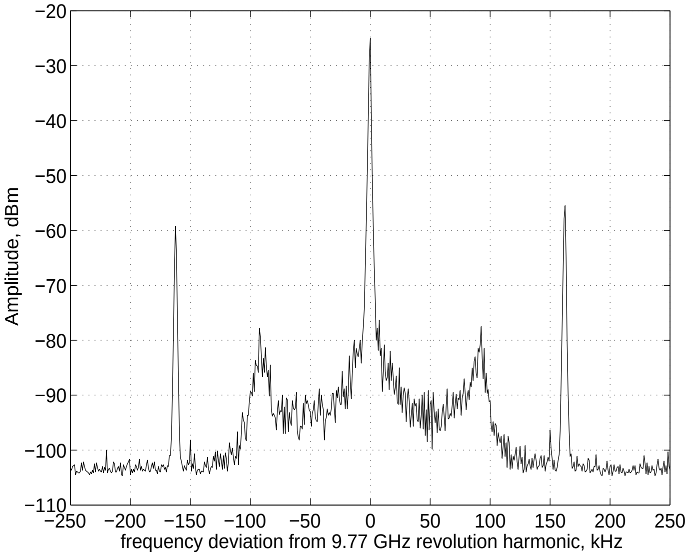

FIGURE 40. Typical BPM spectrum at N=3×10^{10} ppb.

roughly 10% lower than twice the zero current synchrotron frequency at this RF voltage. To represent the change of the instability spectrum with current we use a contour plot of all the spectrum analyzer sweeps for each store as shown in Figure 41.

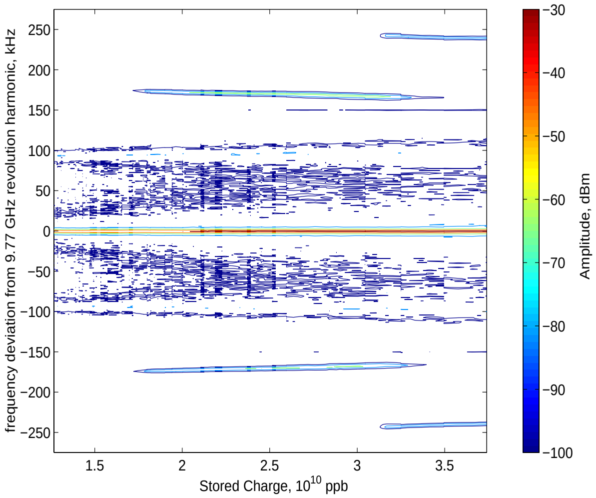

FIGURE 41. Spectrum analyzer data vs. stored charge.

One can see the quadrupole mode threshold at about 1.7×10^{10} ppb. It is also clear how the instability jumps from sextupole to a quadrupole mode in the region of 3.2-3.4×10^{10} ppb. It is interesting that there is no exact harmonic relation between the frequencies of the quadrupole and sextupole modes when they both coexist. Rather than being exactly 3/2 the ratio of the sextupole to the quadrupole mode frequency is only 1.45±0.01. Note that other than this mode switching the instability behavior with current seems to be mundane. The frequency of the quadrupole mode is linearly decreasing at a rate of ~5 kHz/10^{10} ppb. Such a behavior is usually attributed to the inductive portion of the ring impedance.

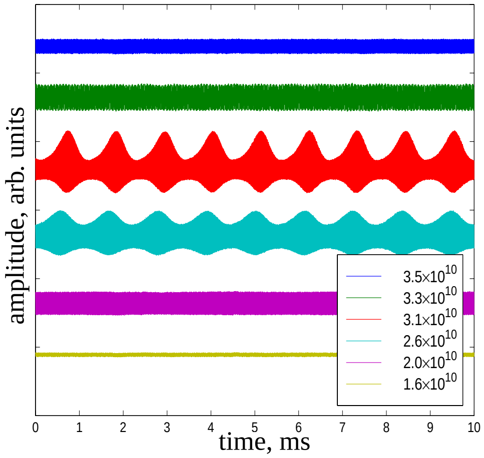

FIGURE 42. Oscilloscope traces of the instability signal for different values of stored charge. Traces and labels go in order.

The picture, however, becomes more interesting if along with the spectrum analyzer data we consider oscilloscope traces taken concurrently. Several such traces taken for the same store as Figure 41 are shown in Figure 42. The top trace that corresponds to the highest current shows a constant amplitude sextupole mode. The second trace from the top relates to the case when both sextupole and quadrupole modes coexist. At even smaller values of current (two traces in the middle) the instability becomes pure quadrupole but it acquires the characteristic bursting behavior. As seen from Figure 42 the bursts repeat in time with a period of about 1 ms. Finally, below 2.5×10^{10} ppb bursts disappear and the quadrupole mode oscillates with constant amplitude.

It is interesting to compare the amplitude dependence of the signals measured by the spectrum analyzer and the oscilloscope. The results for all the traces for this particular store are shown in Figure 43. From the spectrum analyzer data we again clearly see the transition between the quadrupole and sextupole mode. It appears that the sextupole mode has a clear threshold of 3.2×10^{10} ppb while the quadrupole mode makes a slower transition in that region.

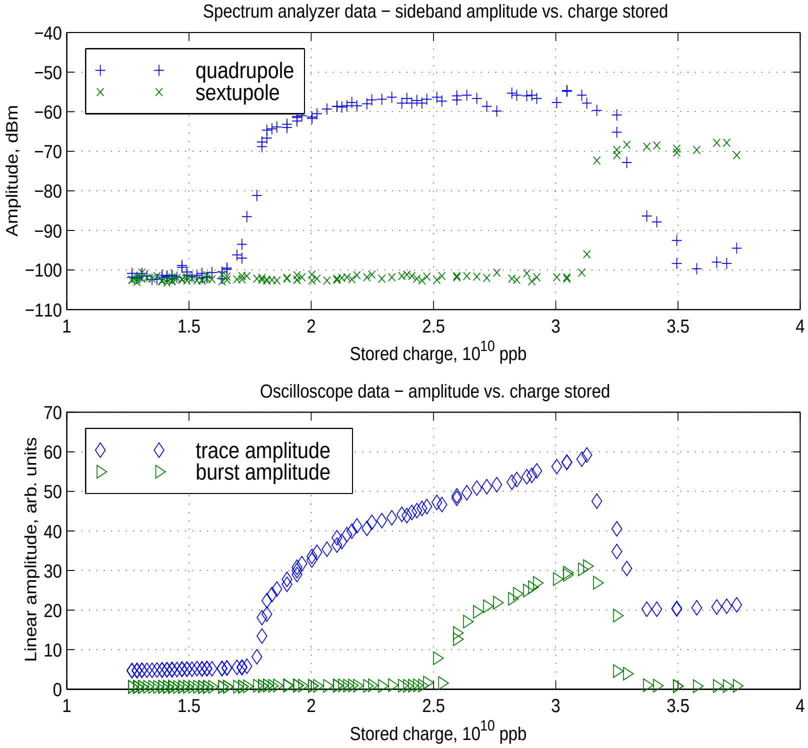

FIGURE 43. Instability amplitude behavior.

In order to summarize the oscilloscope data we derived the amplitude information from the traces by simply taking the standard deviation of the whole trace (trace amplitude) and its envelope (burst amplitude). Although the oscilloscope data does not directly distinguish the two modes, the transition between them is clearly seen as the amplitude jump on the upper trace. The lower trace shows the region where instability is bursting. Note, that the thresholds seen from oscilloscope data slightly exceed the ones observed with the spectrum analyzer which can be attributed to better sensitivity of the latter. Still the agreement between the two plots in Figure 43 is quite good.

Finally, as discussed in Section 5.2 of Chapter 3 the relative amplitudes of the quadrupole and sextupole modes seen from the spectrum analyzer or the oscilloscope data do not reflect the ratio of the quadrupole and sextupole components in the beam phase space. One way to quantify what a particular signal means in terms of the changes to the beam phase space is to simultaneously employ a streak camera to show a variation of the beam profile with the instability signal as will be described in Section 5.0.

4.3 Measurement results: instability properties vs. RF voltage

4.3.1 Quotation of the RF voltage

As we mentioned in Section 1.3.5 of Chapter 3 SCP readings of the RF voltage are unreliable. Calculated values of the RF voltage based on the measured synchrotron frequency should be used instead when possible. This is what we did for this experiment. For each store recorded the frequency of upper and lower synchrotron sidebands were extrapolated to zero current and the average of these two values was taken as f_{s0}. Then the value of V_{RF} was

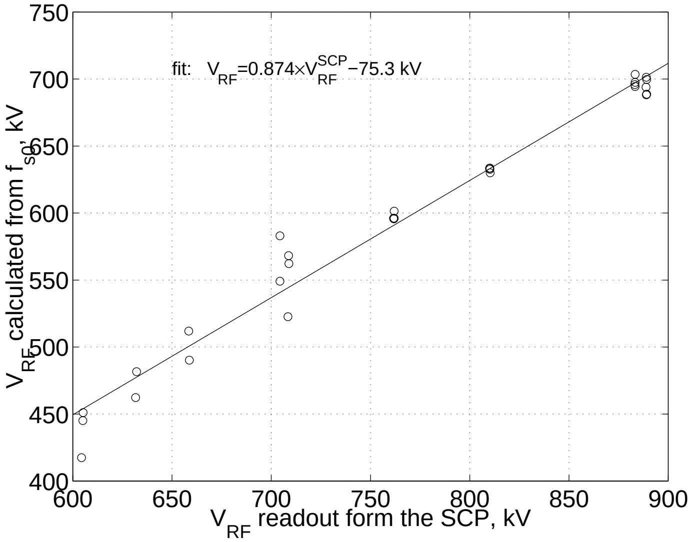

FIGURE 44. Relation between the SCP readout for the RF voltage and the value calculated from the synchrotron frequency.

calculated from f_{s0} utilizing the definition of the synchrotron frequency EQ 2.5. For reference purposes the relation between the calculated and SCP voltages is presented in Figure 44.

4.3.2 Amplitudes

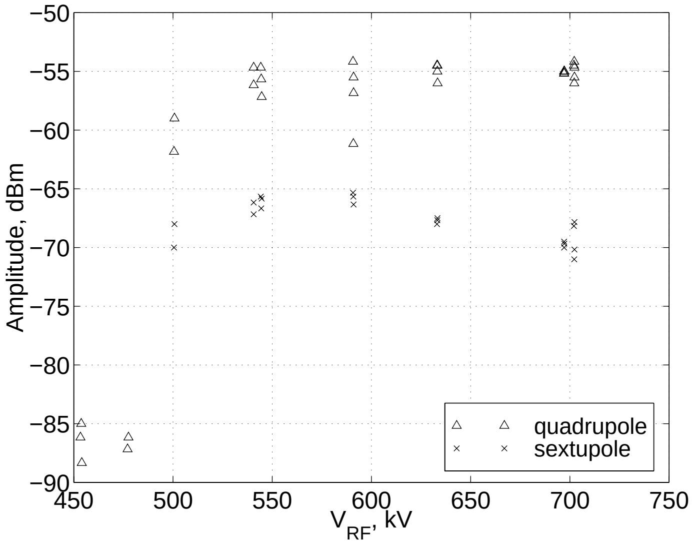

FIGURE 45. Maximum saturation amplitudes of the quadrupole and sextupole modes. Maximum amplitude for the quadrupole mode is usually achieved around N~3×10^{10} while for the sextupole mode it is limited by the initial current.

Figure 45 shows the amplitudes of the instability sidebands as a function of RF voltage. These data points were obtained from the spectrum analyzer data by simply finding maximum values on the curves such as plotted in Figure 43. The dependence is essentially flat (less than 5 dB spread) from the highest value of V_{RF}~700 kV down to about 500 kV after which there is a sharp drop in the amplitudes. In addition to the data shown on the plot there were two more stores recorded at V_{RF}=418 kV and 445 kV that did not show any signs of the instability. We should note that even for the higher voltage values, specifically 450 kV<V_{RF}<480 kV, it is unclear whether the low amplitude data points in Figure 45 actually mean some residual instability signal or they correspond to some RF system noise.

The oscilloscope data generated simultaneously are consistent with Figure 45 and show no instability below 480 kV. In addition, they show that the instability bursts only at higher values of the RF voltage $V_{RF}\geq 630$ kV. The maximum bursting amplitude (as defined in Section 4.2) was measured to be a factor of 5 lower at $V_{RF}\sim 630$ kV than at $V_{RF}\sim 700$ kV.

4.3.3 Thresholds

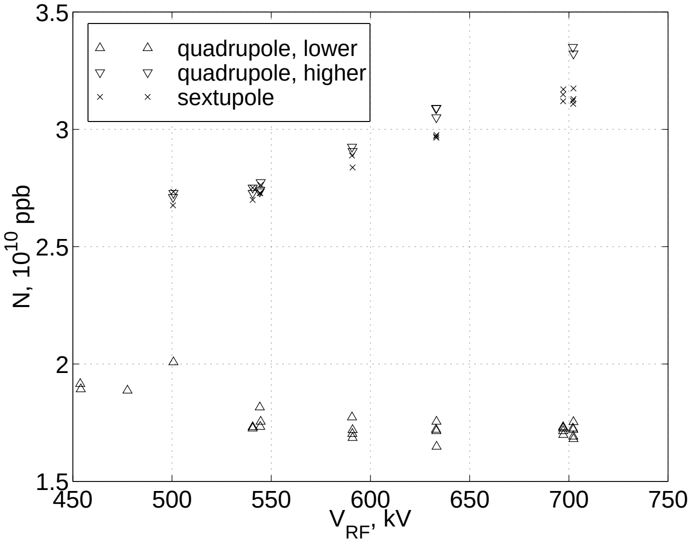

FIGURE 46. Instability thresholds as a function of V_{RF}.

Figure 46 plots several thresholds we obtained from the spectrum analyzer data as a function of RF voltage. In particular, it shows the lower and upper thresholds for the quadrupole mode and the threshold for the sextupole mode. The lower threshold for the quadrupole mode (the instability threshold) is essentially constant $N\sim 1.7\times 10^{10}$ as function of V_{RF} from the highest RF voltage values down to about 550 kV. After that the threshold rises to about $N\sim 2\times 10^{10}$ at $V_{RF}\sim 490$ kV. The same comments as in Section 4.3.2 apply to the three lowest voltage points in Figure 46.

The other two thresholds plotted in Figure 46 behave quite differently than the instability threshold. They remain essentially constant $N\sim 2.7\times 10^{10}$

at lower values of the RF voltage 500 kV<V_{RF}<590 kV and rise with V_{RF} to approximately 3.2×10^{10} (sextupole) and 3.4×10^{10} (quadrupole). Since the upper threshold for the quadrupole mode grows faster with V_{RF} the overlap between the modes widens at higher values of RF voltage.

This data is quite consistent with the one we obtained from the oscilloscope traces. In addition, the oscilloscope data show that the quadrupole mode bursting threshold for the stores at V_{RF}~700 kV is about 2.6×10^{10} and is roughly 3×10^{10} for V_{RF}~630 kV stores.

4.3.4 Frequencies

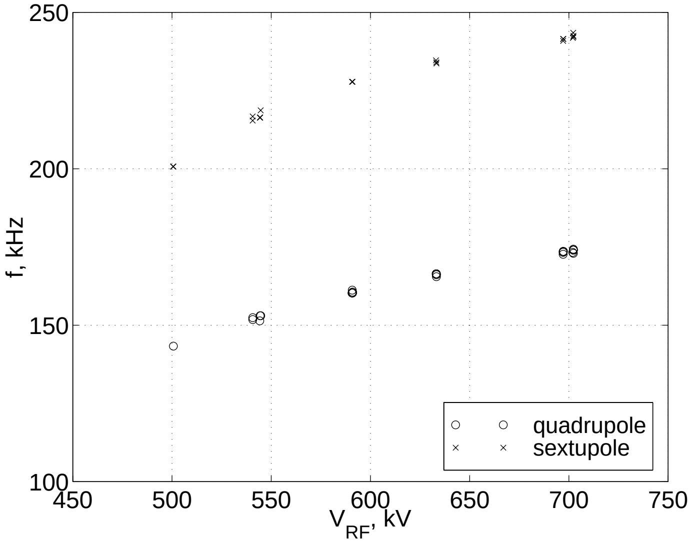

FIGURE 47. Quadrupole and sextupole mode frequencies at the thresholds for these modes.

Figure 47 shows the threshold frequencies for the quadrupole and sextupole modes. Both curves can be fitted reasonably well with a square root function, however due to a limited range of V_{RF} other dependencies cannot be ruled out.

4.4 Discussion and summary of the results

4.4.1 Properties vs. current

It appears that some features of the data obtained, e.g. frequency dependence on current or the quadrupole mode threshold, can be explained in terms of conventional theory that is usually based on the linearized Vlasov equation. For example, in reference [50] simulations with a numerically obtained wake function yielded values similar to those measured. However, some aspects of the measurement results clearly go beyond the linear theory. Those are 1) the fact that instability saturates, 2) occasional bursting behavior and 3) switching between the modes. As it was discussed in Section 5.2.4 of Chapter 2 there have been some theoretical models published ([46]- [50]) that could at least in principle lead to 1) and 2). It appears that item 3) is the most unusual. Indeed, it is common to see more than one azimuthal mode go unstable as intensity increases. What is surprising is that the mode that first goes unstable becomes stable again. Furthermore, this stability switch happens near the intensity value at which the other mode becomes unstable. This suggests some mechanism of coupling between these azimuthal modes. On the other hand, it is commonly thought that as long as frequency shifts are small compared to f_s then different azimuthal modes are independent and instability can only arise as a result of other mechanisms e.g. radial mode coupling.

4.4.2 Properties vs. RF voltage

Briefly the instability behavior with the RF voltage can be summarized as follows

- The instability is not present or insignificant below 480 kV.
- The saturation amplitudes for both the quadrupole and the sextupole modes are essentially independent of the RF voltage when it exceeds 500 kV.

- The threshold of the instability is independent of the RF voltage when the latter exceeds 550 kV. The threshold becomes higher at lower values of V_{RF}.
- The threshold for the sextupole mode and the upper threshold for the quadrupole mode are approximately constant below 580 kV and increase significantly when RF voltage exceeds that value.
- The quadrupole mode is bursting only at higher values of V_{RF}. The amplitude of the bursts increases significantly with V_{RF}.

We note that the very fact that some of the instability properties have significant RF voltage dependence is not trivial. Indeed, from theoretical point of view the instability depends on two parameters only. The first is the intensity I which is by definition (EQ 2.46) voltage independent. The second is the size of a characteristic feature of the wake function in units of zero current bunch length σ_0. This parameter has only a week square root dependence on accelerating voltage and does not change appreciably within the range of voltages we had in the experiment. Furthermore, it is interesting that while some features of instability are very sensitive to the RF voltage the other similar features are not. For example, we observed significant growth of the sextupole mode threshold with RF voltage in contrast to the essentially flat instability threshold curve in the same voltage range.

5.0 Instability phase space structure experiments

5.1 Results from the 96/97 SLC run [65]

5.1.1 Setup and hardware

As it was mentioned above the instability properties in both electron and positron damping rings were similar. Due to some technical reasons the latter was chosen for the present experiment.

The setup is shown in Figure 48. There were two major beam diagnostic channels. Synchrotron light was analyzed by the streak camera, while the high frequency BPM signal was processed and digitized by an oscilloscope. The key part of the experiment was simultaneous data acquisition; hence the timing was important. Both the camera and the oscilloscope were triggered on the same trigger pulse (locked to the injection cycle) provided by the SLC timing system. The streak camera profiles were recorded by its own computer while the oscilloscope traces were saved on a PC connected via GPIB bus.

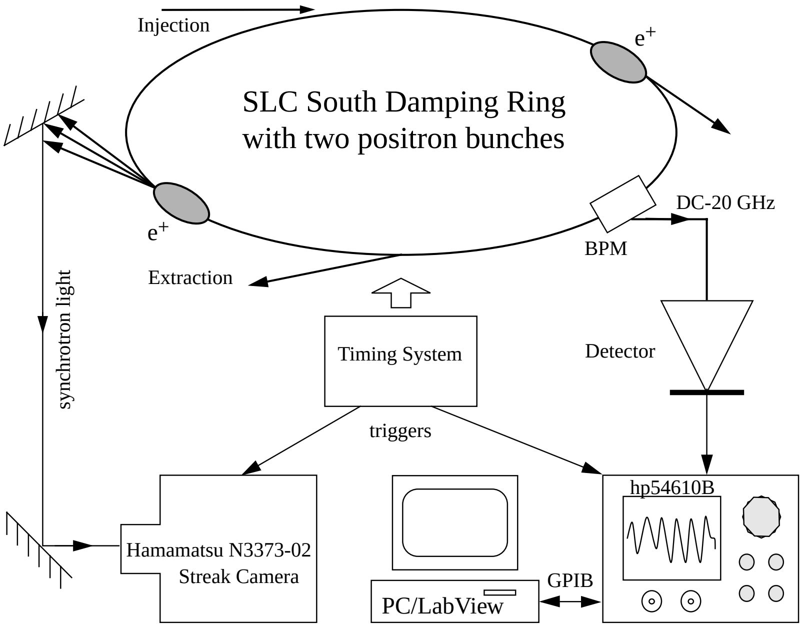

FIGURE 48. Setup for the phase space structure experiment.

5.1.2 Data taking and processing

The experiment consisted of repeatedly taking the streak camera profile and simultaneously recording the detector signal. The oscilloscope time range was 100 μs/screen - enough to cover about 20 instability periods. Both the camera and the oscilloscope were triggered on the same timing pulse always coming ~0.5 ms before extraction and before any external modulation. The oscilloscope trigger position was adjusted so that the streak camera picture was taken exactly in the middle of the trace as illustrated in Figure 49. A total of 589 profiles were acquired in the time-frame of several days under roughly the same running conditions parasitically to the normal SLC operations. The average charge per bunch was 3.8×10^{10} ppb and RF voltage was around 800 kV. The latter was fairly consistent with the value of the synchrotron frequency observed on the spectrum analyzer.

The individual streak camera profiles did not require processing other than a calibration [6]. Bringing all the profiles to the common time reference was less obvious since the centroid position information was lost due to substantial (>30 ps) trigger jitter. Since the instability never causes measurable sidebands near f_s, we assumed that all the movements of the profiles on the streak camera screen were caused by this trigger jitter. This allowed us to find the zero dipole moment time point for each profile and assign t=0 to it.

The instability amplitude and phase at the moment of the streak camera shot were obtained from the oscilloscope traces (Figure 49). To eliminate extraction related effects the last 20% of each trace was discarded and the rest was digitally filtered to reduce the noise (filtering details are not important). We defined the phase of instability based on zero crossings of the filtered signal. For the amplitude we picked the maximum deviation of that signal in the 20 µs region centered at the shot moment. Of course, the phase makes sense only when the amplitude is large, i.e. a burst and the shot coincide.

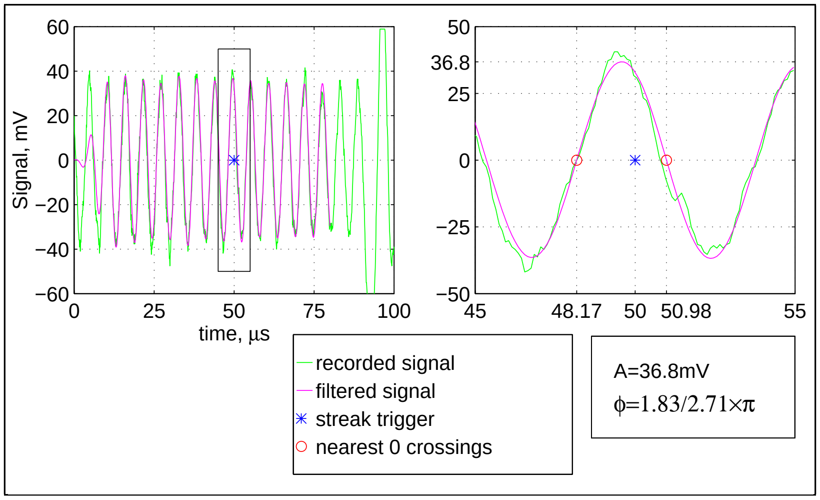

FIGURE 49. Extracting the instability phase and amplitude from the detector signal.

5.1.3 Results

We ended up with a few hundred streak camera profiles each tagged with the instability amplitude and phase obtained from the oscilloscope traces. To study large amplitudes we selected the profiles with the instability amplitudes higher than one half of the maximum bursting amplitude. The average instability frequency corresponding to those 295 profiles was 178 kHz±1 kHz. These profiles had a 7% variation in bunch length that strongly correlated (72% correlation coefficient) with the instability signal.

Subsequently, the large instability amplitude profiles were binned according to their phases. The average shapes for the +π/2±π/4 and -π/2±π/4 phase bins, and the overall average profile are shown in Figure 50. The main changes as the phase varies happen near the top as well as about 30 ps into the head and into the tail. We found that the profile height at those regions varied in a sine-like fashion versus instability phase. Since this is a manifestation of the phase space rotation we defined the instability structure as $\delta\rho(\tau_i) = \langle(\rho_k(\tau_i) - \rho_0(\tau_i))/\sin\phi_k\rangle_k$, where ρ_k are all the profiles with corresponding phases ϕ_k, k=1,2,...295, ρ_0 is the phase-averaged profile (Figure 50, solid) and angle brackets denote the median value.

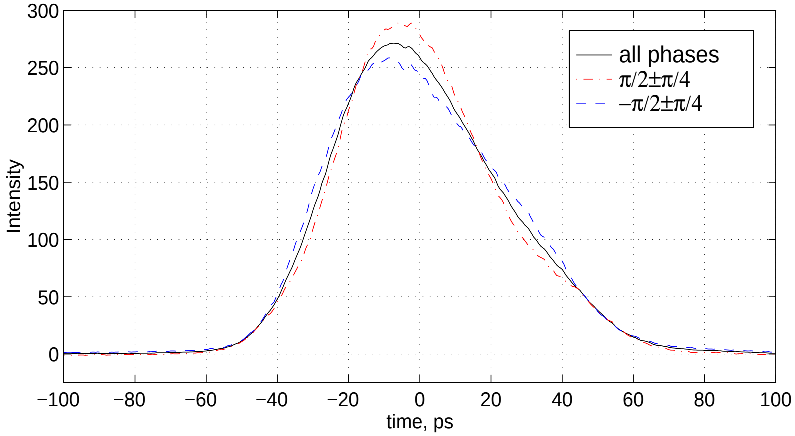

FIGURE 50. High instability amplitude case: average profiles for different instability phases.

The structure obtained is plotted in Figure 51. It is very much like a projection of a quadruple mode (sketched in the corner). The ratio of the positive peak area to the one under ρ_0 is about 3% which measures the amount of redistributed particles creating the quadrupole structure.

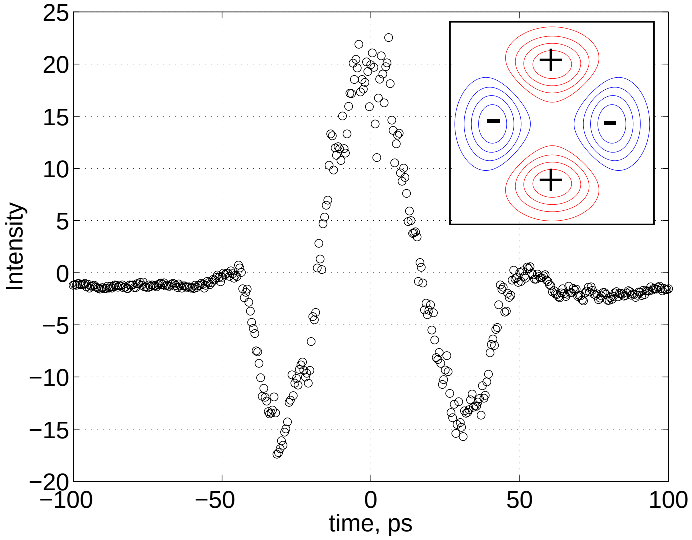

FIGURE 51. High amplitude instability structure.

For the low amplitude case we found the average profile, and it is similar to ρ_0 for high amplitudes. That means that the difference between the beam distributions when the instability is high or low is less than our sensitivity and the characteristic feature size in Figure 51.

Finally, we should note that the average profile shape ρ_0 is quite different from the Haissinski distribution at corresponding current. This is illustrated in Figure 52 where ρ_0 is shown together with a fitted Haissinski distribution corresponding to the damping ring wake $W^{\delta}_{DR}(x)$ from [50]. The fit was done as described in Section 2.0 (fit e). In contrast to Figure 34 plotted for low current data Figure 52 shows a substantial difference in the measured and simulated beam profiles. Particularly, the measured profile is about 15% longer than the simulated one. We note that such a large disagreement could not be caused by the errors in the profile alignment algorithm. Indeed, the bunch length of the average profile (defined as $(2\sqrt{2\log 2})^{-1} FWHM$) falls within 2%

of the average bunch length of the individual profiles. Similar disagreement in bunch shapes was observed when we tried to compare these data with other impedance models described in Section 2.0.

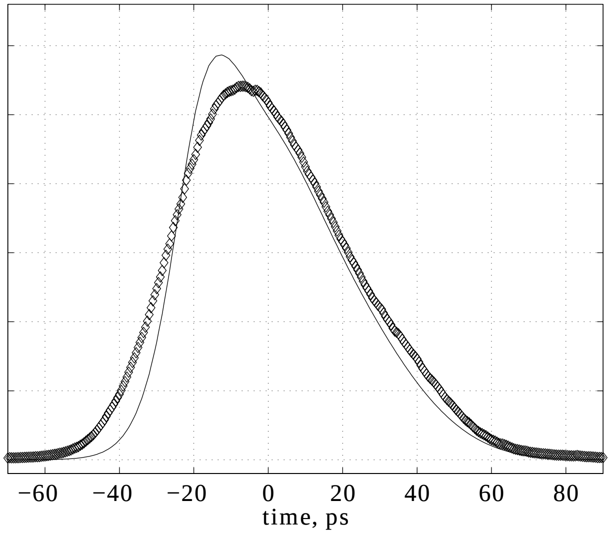

FIGURE 52. Instability phase-averaged beam profile ρ_0 (symbols) and a fitted Haissinski solution for $W^{\delta}_{DR}(x)$ at N=3.8×10^{10}, V_{RF}=800 kV.

5.2 Results from the 97/98 SLC run

5.2.1 Setup changes

During 97/98 SLC run the phase space structure experiment was repeated with improved hardware and at different operating parameters. This section summarizes the changes we made to our setup compared to the one described in Section 5.1.

The main change in the hardware was the addition of the GPIB interface to the streak camera. This allowed us to automate and significantly speed up the data taking process which in turn provided larger amounts of data. In addition, we were able to interface the streak camera and the oscilloscope to the SLC control system as described in Section 2.3 of Chapter 3. This, of course, eliminated the need for PC/Lab-View controller for the oscilloscope (shown in Figure 48) as well as Hamamatsu PCTA-software controller (not shown but used in 96/97 run experiment).

Additional changes in our hardware included switching from 1/2” to a 1/4” HELIAX cable for the BPM pick-up signal and using a better amplifier in the detector circuit. The new amplifier was based on a faster, low noise operational amplifier chip and it had 1 kΩ input impedance to increase the effective sensitivity of the detector. In addition, the HP 54610B oscilloscope was replaced by a more convenient Tektronix TDS 460A that allowed direct video output onto a PC monitor. During our experiment we were recording oscilloscope traces 40 μs in duration.

Finally, the VDU in the streak camera trigger circuit was bypassed and a trombone was added for fine timing adjustment (as described in Section 4.2.3 of Chapter 3). This significantly reduced beam centroid jitter in the recorded profiles and lead to unexpected consequences to be described in Section 5.2.3.

5.2.2 Data taking

Unfortunately, our data taking happened right after an accidental vent in the NDR vacuum chamber. This somewhat compromised our ability to chose operating parameters, since we had to do our experiment (in SDR) in parallel to the RF processing in NDR. We ended up with 60 Hz single bunch operation with the stores of 32 ms long. Roughly 3000 data file pairs were taken in the time period of about 24 hours. The SCP readings of V_{RF} and N, as well as instability frequency extracted from oscilloscope traces are plotted in Figure 53.

During the first half of the experiment the instability was in sextupole mode and then it switched to mostly quadrupole mode after N/V_{RF} were slightly lowered/raised. Throughout the duration of the experiment the instability was in a continuous mode which is consistent with the results described previously in Section 4.0. We should point out that the experiment described in that section was done right after the present one.

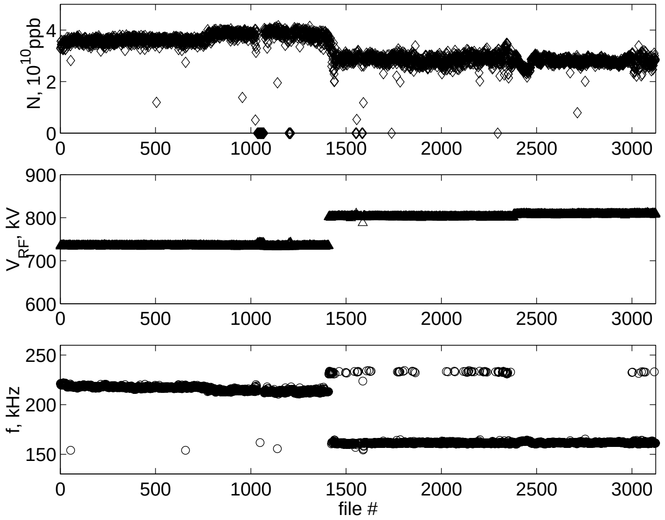

FIGURE 53. Operating parameters and instability frequency.

5.2.3 Data processing

The core of the data processing algorithm remained the same as described in Section 5.1.2. A few important details have changed and are described below.

First of all, due to automated data acquisition roughly 2% of data files were recorded during “bad stores” which we define as those when no streak camera profile (or a profile that is impossible to fit) was recorded. Most of these stores corresponded to the cases when the timing system sent all the triggers needed but there was no beam. Others include beam stores with very low current, drops in the RF voltage, different injection pattern due to rate limiting etc. Such stores were discarded from further processing.

Second, since the instability was in a continuous mode we implemented a better fitting routine for the oscilloscope traces. Instead of relying on just two zero-crossings during one instability period we used a nonlinear least squares algorithm to fit the whole 40 μs trace with a sine-like curve with the amplitude, the frequency and the phase being the fit parameters.

With the two changes above included we processed a major portion of the data when the instability was in a quadrupole mode. Unexpectedly, we observed a strong correlation between the centroid positions of fitted profiles and their bunch lengths. The bunch length for the files in the center of the CCD was about 20% longer than for those closer to either edge of the CCD (see Figure 54 top). This systematic effect of course hid the instability induced features in the beam distribution. We have traced this effect to a local sensitivity drop in the streak camera system (most likely the photocathode). To correct for this we had to boost the values for the CCD pixels from 191 to 256 by various amounts up to 14%. To find the correction coefficients for each pixel we used a procedure described in detail in reference [66] (however, we came up with slightly different correction coefficients). In summary, this procedure amounts to i) constructing an average beam profile from the data without any centroid alignment, ii) identifying the pixel range on this profile that is significantly depressed compared to the neighboring areas, iii) using a fourth order polynomial to extrapolate the average profile into that region, and iv) defining the correction coefficient for each pixel as a ratio of the polynomial to the actual profile values in the depressed region.

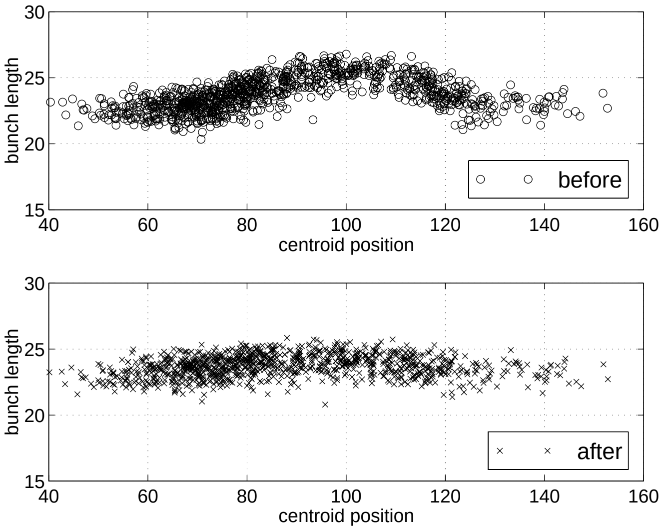

FIGURE 54. Bunch length dependence on the centroid position before and after the sensitivity calibration.

As a source profile we used a sum of all the profiles from 96/97 run. In contrast to the data from the present experiment those profiles were much more uniformly distributed in their centroid positions due to larger trigger jitter. Adding such a correction has essentially eliminated the bunch length dependence on the centroid position as illustrated in Figure 54. We have used this correction to get the results to be described next.

5.2.4 Results

Using the data processing with the changes described above we have separately processed the files that correspond to the sextupole mode at V_{RF}=730 kV and to the quadrupole mode at V_{RF}= 800 kV (SCP readings). This choice is obvious from Figure 53. For the purposes of this section we will refer to these data as a sextupole and quadrupole batches. After making cuts in the profile area, beam current, and instability frequency and amplitude the total number of files remained in the sextupole and the quadrupole batches were 1164 and 1590 respectively. The average instability frequency was calculated to be 161.5 kHz±0.8 kHz for the quadrupole batch and 216.3 kHz±2.3kHz for the sextuple batch.

The average bunch shapes for these two batches are plotted in Figure 55. Other than a small difference in the bunch length which is 25.3 ps for the sextupole batch vs. 23.7 ps for the quadrupole batch, the bunch shapes are quite similar. At the same time, similarly to the data from the previous run, these average shapes are substantially different from the corresponding Haissinski solutions, particularly they are significantly longer. This statement holds for every wake function model described in Section 2.0.

The spread in bunch lengths of individual files turned out to be 3% for the sextupole batch and 4% for the quadrupole batch. It is conceivable that a substantial portion of this spread is due to the instability, especially for the quadrupole batch. Indeed, the correlation coefficient between the bunch length

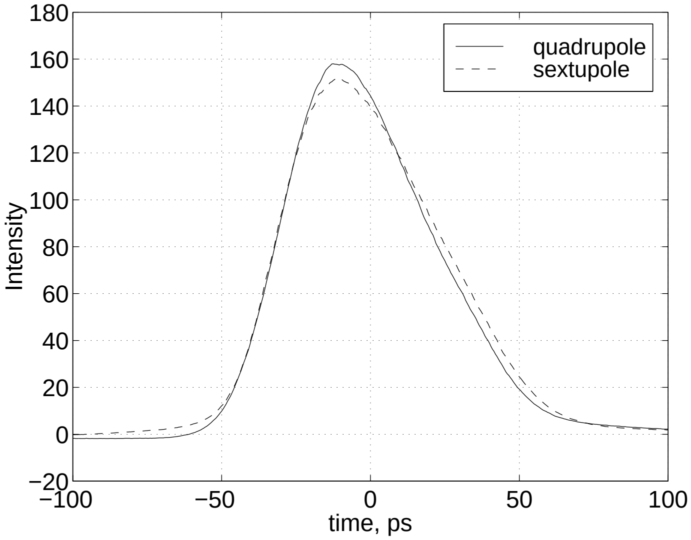

FIGURE 55. Average beam profiles for quadrupole and sextupole batches.

and the instability signal is 54% for the quadrupole batch and 24% for the sextupole batch.

The instability induced structure is plotted in Figure 56. The quadrupole

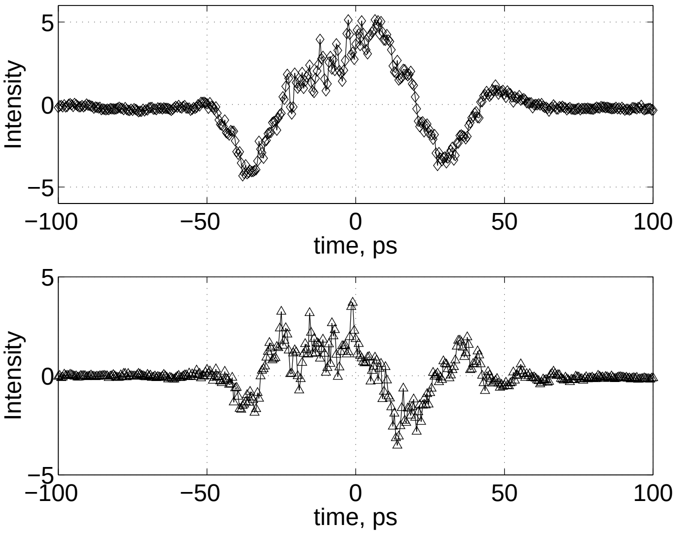

FIGURE 56. Measured instability mode structure for quadrupole (top) and sextupole batches.

mode structure is clear although it is not as symmetric as the one obtained from the 96/97 run data. The number of particles displaced by the quadrupole mode is about 1%.

For the sextupole batch the mode structure is nosier. Nevertheless the two positive peaks and two negative peaks (the characteristic feature of the sextupole mode) are fairly pronounced. The total area under the two positive peaks is about half a percent of that under the average bunch shape.

It is worth mentioning that while in both cases the instability amplitudes obtained are fairly small the results shown in Figure 56 are statistically significant. To illustrate this we repeated the same data processing except we replaced the instability phases extracted from the oscilloscope traces by an array of random numbers uniformly distributed from -π to π. The resulting mode structures are plotted below.

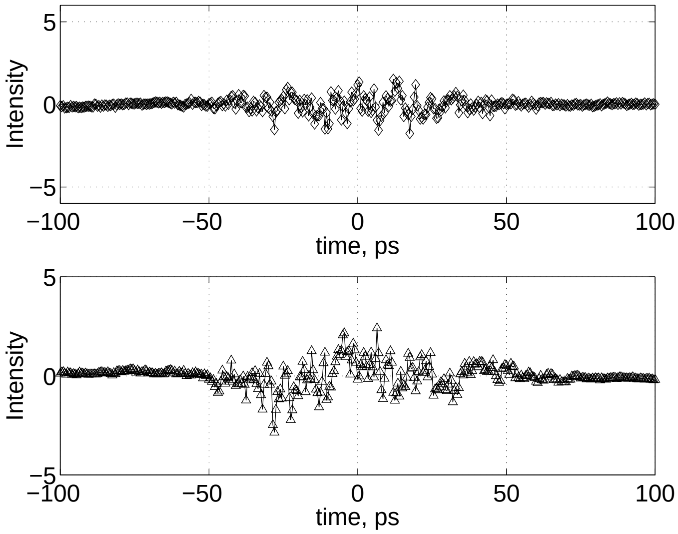

FIGURE 57. Simulated instability mode structures for quadrupole (top) and sextupole batches.

The characteristic feature size in Figure 57 is much smaller than that in Figure 56 which outlines the statistical significance of the results shown in the latter.

5.3 Summary

Combining the instability signal detector with the streak camera proved to be valuable technique for studying longitudinal microwave instability. This combination allowed us to simultaneously take advantage of beneficial properties of the detector (continuous data taking) and the streak camera (practically infinite bandwidth). In addition, interfacing this setup to the SLC control system we were able to acquire large number of data files allowing quantitative studies of a fairly small effect.

Utilizing this setup we have measured the phase space features for the strongly developed saw-tooth instability. The instability can be in either quadrupole or sextupole mode and contains anywhere from a few percent down to a fraction of a percent of the beam particles. In addition, the average profile at large instability amplitudes for the case of bursting instability was measured to be the same as the distribution at small amplitude. These facts make it likely that the instability can be interpreted with perturbation techniques.

Finally, there appears to be some difference in the instability frequency, strength and modal structure for the data from two different SLC runs. Although the two experiments were done with different number of bunches stored in the ring we do not think that this was significant (see Appendix A for more details). Rather we believe that this difference is due to the changes done to the SDR vacuum chamber and RF system between the two runs. These included replacing the RF cavity and the klystron, installation of RF shielding on the ion pump slots in the RF cavities, significantly changing the design of a kicker magnet as well as some smaller jobs. While we cannot definitely attribute observed difference to any one of these factors we can speculate that some of them may have affected the ring impedance and the instability properties.

6.0 Instability signal correlation with the bunch behavior downstream of the damping rings

6.1 General comments

So far we have only presented the instability measurements in the damping rings. Since the rings serve as injectors to the SLC linac we expect that the instability in the damping rings may affect the performance of the SLC as a whole.

To quantitatively characterize this we have performed a series of measurements correlating the instability signal at extraction to the beam trajectories in the linac downstream of the damping rings. These experiments were performed on both electron and positron bunches during 96/97 and 97/98 SLC runs.

6.2 Setups

We have mostly used the setup with the GADC running the buffer acquisition utility. The instability signal was usually sampled a fraction of a μs before extraction. Another (much slower) version of the experiment included running the correlation plot software while recording the instability signal traces with an oscilloscope interfaced to the SCP as shown in Figure 16. With this method the instability signal amplitude and phase at extraction were fitted online and sent to the correlation plot utility. Other machine variables recorded by the buffer acquisition or correlation plot utilities included BPM readings for various sectors in the linac as well as in the RTL. We have also recorded the “36 GHz bunch length” which is a GADC readout of the high frequency detector in the microwave cavity coupled to the beam pipe in sector 25 [67]. It was shown in the streak camera measurements described in [6] that this signal is proportional to the bunch length divided by the beam current.

6.3 Examples of measurement results

6.3.1 NDR instability results from 97/98 SLC run

An example of one 1024 point buffered data acquisition file is shown in Figure 58. This data was taken on December 8, 1997 with the instability signal derived from the production bunch in the electron damping ring. The beam conditions were $N_{two\ bunches}$=8.3×10^{10}, V_{RF}=700 kV, and the current jitter was on a 1% level. The values shown on both axis are direct readings from the corresponding GADCs and BPMs as recorded by the buffer data acquisition program.

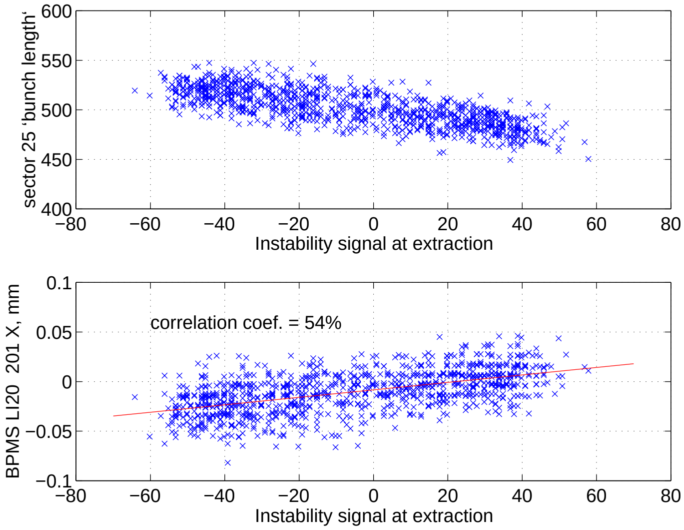

FIGURE 58. Correlation between the NDR instability and linac signals.

The top plot shows that the damping ring instability signal correlates with the bunch length in sector 25. The correlation is not 100% which may be caused by measurement errors or be due to other factors affecting the bunch length in the linac. Nevertheless, since the linear correlation coefficient exceeds 80% we conclude that the damping ring instability is the dominant factor in the bunch length jitter.

On the bottom plot the readings of the BPM 201 x in sector 20 are plotted against the instability signal. First of all, we note that there is a significant spread in the BPM readings. In fact, for the data set shown the standard deviation in pulse-to-pulse horizontal BPM readings exceeds 20 μm. This is to be compared with the typical horizontal beam size in the linac on the order of 50 μm. Second, we note that the significant part of this jitter comes from the instability in the damping rings. The linear correlation coefficient between the values plotted is 54%.

During this measurement we were recording the BPM 201 readings for even sectors 2 through 24 and for all the remaining sectors. The correlation coefficient vs. the linac sector number is shown in Figure 59. This figure leads us to the following conclusions i) correlation coefficient in both *x* and *y* rapidly changes from sector to sector and grows along the linac, ii) this correlation coefficient can be as high as 50%, iii) correlation of instability signal with current in the linac is insignificant.

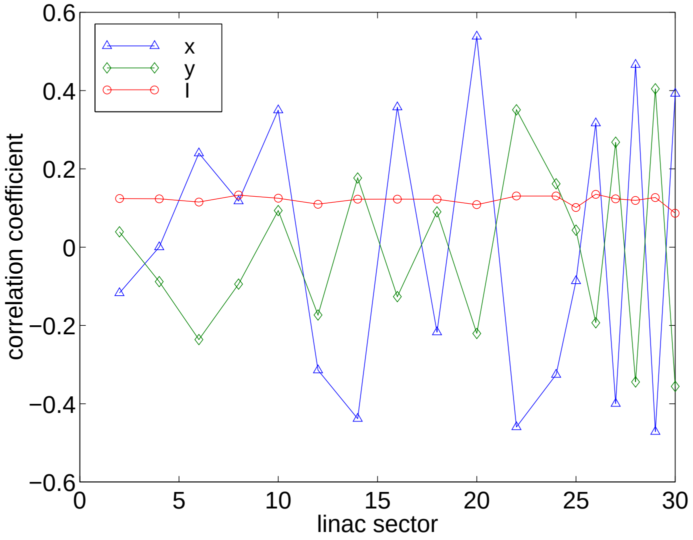

FIGURE 59. Instability signal correlation with BPM readings along the linac I.

When running above the instability threshold it was always possible to find a sector with significant correlation between the damping ring instability signal and either *x* or *y* BPM reading. However, the exact dependence vs. sector number would change considerably depending on the linac tuning and possibly other factors. For example, similar data taken three months earlier on September 14 ($N_{two\ bunches}\sim 8.3\times 10^{10}$, V_{RF}=890 kV) is plotted below.

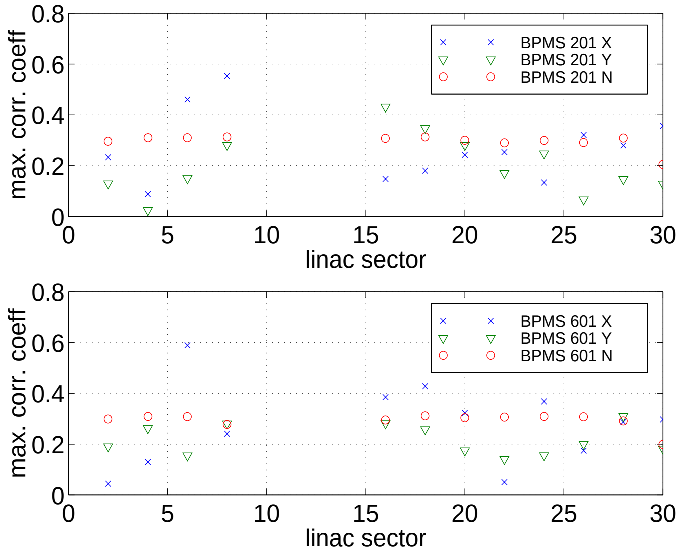

FIGURE 60. Instability signal correlation with BPM readings along the linac II.

These data were taken through the correlation plot utility. For each SLC cycle a 100 μs long instability signal trace before the extraction was recorded. Subsequently, the correlation coefficient was calculated between each point of this trace and the corresponding linac data. The maximum value of the correlation coefficient is plotted in Figure 60.

6.3.2 SDR instability results from 96/97 SLC run

An even higher correlation between the beam jitter in the linac and the instability signal in the SDR was observed during the 96/97 SLC run. We have routinely observed instability signals correlation with the transverse BPM readings exceeding 60%. For one particular case (when the correlation coefficient was about 64%) it was estimated that the total jitter power coming from the instability exceeded 40% making the instability one of the major contributors to the beam transverse jitter. A typical development of the correlation along the linac is shown in Figure 61.

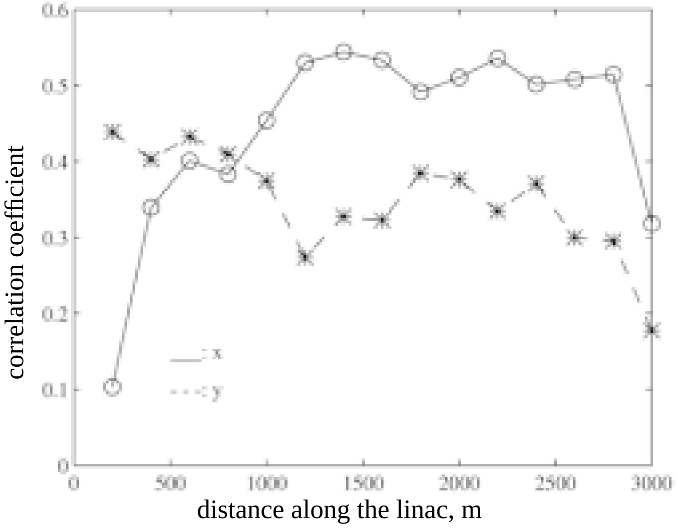

FIGURE 61. Instability to jitter correlation (from [69]).

6.4 Discussion

The correlation between the instability signal and the bunch length in the linac is not surprising. Indeed, there are no other elements downstream of the RTL compressors that should affect the bunch length and/or the energy spread. If the compressor voltage is stable, the correlated energy spread and bunch length jitter (coming from the damping rings due to the instability) is preserved down to the end of the linac.

In addition to preserving the bunch length jitter, the compressor may introduce the correlation between the transverse and longitudinal displacement of the beam particles. This occurs due to non-zero dispersion (introducing $\delta x = \eta\delta$) or higher order dispersive terms in the compressor optics ($\delta x = \eta^{(n)}\delta^n$) that lead to different offset of particles with different energies. This correlation further develops along the linac due to the transverse wakefields [69].

Another cause of the bunch length correlation to the transverse displacement comes directly from the incoming bunch length jitter amplified by the transverse wakefields. They introduce the dependence of the phase advance on the bunch length and therefore convert the bunch length jitter into the transverse orbit jitter. This qualitatively explains the dependence along the linac shown in Figure 59 where drastic changes in the correlation coefficient from one BPM to another simply reflect different betatron oscillation phase spreads.

There are, of course, other sources of transverse jitter in the beam trajectories in the SLC linac. Some of them include quadrupole vibrations induced by the water pumps, slow vibration of the accelerator supporting structure, ground motion, and the quadrupole field ripple. All of these factors were analyzed in reference [68] by running computer simulations with the realistic beam lattice, wakefields, klystron phasing and orbit bumps. It was found that if the bunch length jitters on the order of 10% (based on our measurements described in Section 5.1) this may lead to the transverse beam trajectory jitter of 35% of σ_y.

Note that the transverse jitter this large may significantly compromise the SLC luminosity, because it decreases the effective overlap area between the colliding beams in the final focus. Future linear colliders have even lower tolerance to the transverse jitter because the beam size is expected to be reduced an order of magnitude or more [70].

Finally, we should note that having continuous GADC based diagnostics of the level of the instability signal proved to be useful for the regular SLC running. In case of unexpected increase in the linac jitter it allowed to easily check whether it was due to the increase in the instability level in the damping ring or alternatively eliminate is as a suspect.

Chapter 5

Analytical results and comparison with experiments

1.0 Asymmetry in the instability sidebands

Among the peculiar features of the BPM signal spectra from unstable bunches are unequal heights of the left and right instability sidebands. This is clearly seen for example in Figure 21 or Figure 40. In both cases the upper instability sideband exceeds the lower one by about 4 dB. In the course of our studies we have routinely observed an asymmetry between the instability sidebands with magnitudes as high as 5 dB with either the upper or the lower sideband being the highest. This ratio changes (both in magnitude and sign) as a function of current, suggesting that this asymmetry is a property of the instability rather than being due to variation in the BPM sensitivity. In addition, the fact that asymmetry can be present several minutes into the store (Figure 40) argues that it is coming from the particles in the final, saturated state of unstable beam rather than being caused by the injection transients or initial growth due to the instability.

Such a significant difference in the amplitudes of the instability sidebands cannot be explained by a simple derivation given in Section 5.2 of Chapter 3. Some asymmetry indeed appears in that derivation and it is due to the envelope functions. We expect, however, these envelope functions to change appreciably only in the frequency range of $\Delta\omega \sim c/\sigma_{inst}$ where σ_{inst} is the characteristic size of the instability induced structure within a beam. For any storage ring this number is orders of magnitude higher than the synchrotron frequency ω_s meaning that envelope functions are essentially flat between the lower and higher instability sidebands for any rotation harmonic.

Therefore the asymmetry observed is due to something else that was unaccounted for in the derivation of Section 5.2 of Chapter 3. One possible generalization is to account for a deviation of beam particle trajectories from a pure harmonic motion. As discussed earlier such a deviation does occur even below the instability threshold and we naturally expect it to continue above the threshold as well. As it will be shown below such an approach not only may explain our observations but also gives additional insight on the physics of the instability.

Before we proceed with the derivation we should mention that other explanations of the sideband asymmetry have been proposed in references [47] and [50]. However, we believe that neither of these fully explains the effect at least for the case of the SLC damping rings. The explanation in [47] requires two azimuthal modes to be excited simultaneously and the frequencies of these modes to be exact multiples of each other. This disagrees with our experimental observations described in the previous chapter. The second reference ([50]) states that the sideband asymmetry is caused by the asymmetry in the potential well, which we find to be incorrect as will be described in Section 1.2.

1.1 Simple case - second harmonic term

For brevity we assume in this section that only the second harmonic term is present in the particle trajectory. The generalization to include more terms is straightforward.

Similar to EQ 3.6 we assume now that the beam current is given by

$$I(t) = \sum_{n=-\infty}^{\infty} \delta(t - nT_0 - a\cos(\omega_s nT_0) - \alpha a\cos(2\omega_s nT_0 + \phi)), \tag{5.1}$$

where α is a small parameter. Compared to EQ 3.6 we have neglected the phase shift φ in the fundamental harmonic that was shown not to affect the magnitude of the single particle spectrum. In addition, we have introduced the phase shift ϕ between the second and the first harmonics of single particle motion.

The spectral density of such current is given by

$$\tilde{I}(\omega) = \omega_0 \sum_{k,\, l,\, n = -\infty}^{\infty} (-i)^k J_k(\omega a) J_l(\alpha\omega a) e^{-il\psi} \delta(\omega + (k+2l)\omega_s - n\omega_0), \qquad (5.2)$$

where $\psi \equiv \phi + \pi/2$.

Let us look at a pair of sidebands of order q near some rotation harmonic $n=n_0$. The sideband frequencies are given by $\omega_{\pm}=n_0\omega_0 \pm q\omega_s$. From the discussion of Section 5.2 of Chapter 3 we can limit our consideration to positive frequencies only and then account for the negative ones by simply doubling the resulting amplitude. Therefore, the amplitudes of the upper and lower sidebands are given by

$$A^+ = 2\omega_0 \left| (-i)^q \sum_{l=-\infty}^{\infty} J_{q-2l}(\omega_+ a) J_l(\alpha\omega_+ a) e^{-il\psi} \right|, \qquad (5.3)$$

$$\begin{aligned} A^- &= 2\omega_0 \left| (-i)^{-q} \sum_{l=-\infty}^{\infty} J_{-q-2l}(\omega_- a) J_l(\alpha\omega_- a) e^{-il\psi} \right| \\ &= 2\omega_0 \left| (-i)^q \sum_{l=-\infty}^{\infty} (-1)^l J_{q-2l}(\omega_- a) J_l(\alpha\omega_- a) e^{il\psi} \right|. \end{aligned} \qquad (5.4)$$

As we have already mentioned due to small a there is basically no difference in the values of Bessel functions at lower and upper sideband frequencies. Therefore, if it was not for the extra $(-1)^l e^{2il\psi}$ factor in EQ 5.4 the amplitudes of the sidebands would be approximately equal. We first note that this factor has absolute value of 1 for a special case $\psi=\pm\pi/2$ or equivalently $\phi=0, \pi$. We will comment on the significance of this case in the next section.

For now we rewrite the two formulas above in a slightly different way that explicitly shows the asymmetry in a general case. Using the known Bessel function properties we have for the amplitudes

$$\begin{aligned} A^{+} = 4\omega_0 \Bigg| & \sum_{l\,=\,0,\,2,\,\ldots}^{\infty} [J_{q-2l}(\omega_+ a)e^{-il\psi} + J_{q+2l}(\omega_+ a)e^{il\psi}]\,J_l(\alpha\omega_+ a)\frac{1}{1+\delta_{l0}} \\ & + \sum_{l\,=\,1,\,3,\,\ldots}^{\infty} [J_{q-2l}(\omega_+ a)e^{-il\psi} - J_{q+2l}(\omega_+ a)e^{il\psi}]\,J_l(\alpha\omega_+ a)\Bigg|, \end{aligned} \tag{5.5}$$

$$\begin{aligned} A^{-} = 4\omega_0 \Bigg| & \sum_{l\,=\,0,\,2,\,\ldots}^{\infty} [J_{q-2l}(\omega_- a)e^{il\psi} + J_{q+2l}(\omega_- a)e^{-il\psi}]\,J_l(\alpha\omega_- a)\frac{1}{1+\delta_{l0}} \\ & - \sum_{l\,=\,1,\,3,\,\ldots}^{\infty} [J_{q-2l}(\omega_- a)e^{il\psi} - J_{q+2l}(\omega_- a)e^{-il\psi}]\,J_l(\alpha\omega_- a)\Bigg|, \end{aligned} \tag{5.6}$$

where δ_{l0} is a Kronecker's symbol.

It is clear that the envelope functions for the upper and lower sidebands are essentially different due to opposite signs of odd terms in l (and l=0 term being the dominant one).

We can simplify the formulas above for small α. For example, the ratio of two quadrupole sidebands $(q=2)$ comes out to be

$$\frac{A_2^{+}}{A_2^{-}} \approx \left|1 - \alpha\bar{\omega}\frac{J_0(\bar{\omega}) - J_4(\bar{\omega})}{J_2(\bar{\omega})}\sin\phi\right|, \tag{5.7}$$

where $\bar{\omega} \equiv n_0\omega_0 a$, index denotes the sideband order, and we only kept terms up to the first order in α. Therefore, for a given observation frequency and amplitude of the synchrotron motion, the asymmetry in instability sidebands is directly proportional to the relative strength of the second harmonic times the sine of its phase with respect to the fundamental. From the derivation above it is easy to see that we would arrive to the same conclusion had we considered 4th, 6th or any other even harmonic in the single particle motion. Odd harmonics, on the other hand, would not produce any asymmetry.

It should be noted that the derivation above considers only the single particle motion. Without a detailed model of the instability and understanding of the coherent beam motion we cannot predict which particular set of sidebands dominates the spectrum. Furthermore, even if we pick a set of quadrupole sidebands we cannot fully utilize EQ 5.7 since do not have any handle on the value of ϕ which is a free parameter in the present model. Nevertheless, assuming that a typical value of ϕ becomes significant (ϕ~1) during the instability we can attempt some comparison with the observations.

As an example we consider n_0=1149, a=30 ps, and α=0.1 which according to EQ 5.7 gives the ratios of 3 dB and -4 dB for $\phi=\pi/2$ and $\phi=-\pi/2$ respectively. Provided that ϕ is not too small, we see that even a minor second harmonic term in particle motion leads to the magnitude of the asymmetry comparable to the one observed in experiment (see for example Figure 40 for the spectrum and Figure 56 for the value of a).

1.2 General case and time inverse asymmetry

Now consider a general case of periodic single particle motion

$$x(t) = \sum_{k=1}^{\infty} a_k \cos(k\omega_s t + \phi_k), \tag{5.8}$$

where we again assume that ϕ_1=0.

A BPM samples the beam current

$$I(t) = \sum_{n=-\infty}^{\infty} \delta(t - nT_0 - x(nT_0)) \tag{5.9}$$

which in this case has the spectrum

$$\tilde{I}(\omega) = \sum_{k_1, k_2, \ldots = -\infty}^{\infty} \left(\prod_{p=1}^{\infty} J_{k_p}(a_p\omega) e^{-ik_p\psi_p} \right) \sum_{n=-\infty}^{\infty} \delta\left(\omega + \omega_s \sum_{p=1}^{\infty} p k_p - n\omega_0 \right), \tag{5.10}$$

where $\psi_p \equiv \phi_p + \pi/2$. From this spectrum it follows that the envelope functions for the upper and lower sidebands of the same order are generally different. Similar to the result of the previous section it turns out that the envelope functions are the same in either of two special cases i) when *x(t)* includes odd harmonics only or ii) *x(t)* has arbitrary harmonics but there is a special phase relationship between them, namely they all are in phase with the fundamental $\phi_p=0$, $p=2,3,\ldots$ Let us look at the second case in more detail.

Inspecting the trajectory EQ 5.8 it is easy to see that the constraint of all phases being zero is nothing else than a requirement for this trajectory to be time inverse symmetric. This means that there exists such a fixed time shift Δ that for any time t

$$x(-t) = x(t+\Delta). \tag{5.11}$$

In other words, this condition means that when the time is reversed the trajectory repeats itself with the exception of a possible shift of the initial point to a different point in phase space that lies on the same trajectory.

The fact that any time inverse symmetric trajectory leads to symmetric sidebands can be seen directly from EQ 5.10. Indeed, for such a trajectory and its time inverse compliment *x(-t)* the BPM spectra are the same. Formally, however, the *x(-t)* trajectory has the corresponding spectrum given by EQ 5.10 with the sign of ω_s flipped in the argument of the δ-function. This sign flip can be viewed as an interchange between the envelopes of the upper and lower sidebands. Therefore, the spectrum of any time inverse symmetric trajectory has the same envelope functions for the lower and upper synchrotron sidebands of any given order. This means that the sidebands to any rotation harmonic are essentially equal.

This last observation connecting the time inverse symmetry of the single particle motion and the sideband symmetry in the corresponding spectrum allows drawing important conclusions. Since the sideband asymmetry is observed in experiments we conclude that at least some beam particles have time inverse asymmetric motion. Since the laws of mechanics are time reversible it requires the single particle Hamiltonian of unstable beam to be time dependent (due to the timescale of the problem we can neglect the effects of the synchrotron radiation). However, as we mentioned at the end of Section 5.2.3 of Chapter 2 this Hamiltonian is explicitly time independent. The dependence on time can appear in the system (and the Hamiltonian) if the particle density becomes time dependent as a result of spontaneous symmetry breaking process [44]. Therefore, the presence of unequal sidebands in the spectrum is an indication that such a process indeed takes place during the saw-tooth instability.

2.0 Instability threshold and the physics of the instability

As discussed in Section 5.2.2 of Chapter 2 there are several empirical criteria for the onset of microwave instability. Apart from exotic case of multiple minima in the unperturbed collective potential all the other criteria are based on the dependence of incoherent particle frequency on action $\omega(J)$. Utilizing the linearized Vlasov equation technique, we will show shortly that such criteria are flawed and they may not work for all impedances. It will be shown that the instability appears due to the real part of impedance which affects the single particle motion by creating an asymmetry of the collective potential. This asymmetry can also be expressed through the relative strength of even harmonics of particle trajectories. We will show that the above statements regarding the stability apply both to the case of radial and azimuthal mode coupling. Finally, making certain simplifying assumptions that hold at low intensity we will show how to find analytically the upper bound estimate on the value of the growth rate for any azimuthal mode. Provided that the radiation damping rate is known such a calculation gives an estimate of the instability threshold.

2.1 Analysis of the dispersion relation

We start with the linearized Vlasov equation dispersion relation EQ B.11 derived in Appendix B which reads

$$\frac{\Omega}{m}\tilde{f}_m(J) = \omega(J)\tilde{f}_m(J) + I\frac{d\rho_H}{dJ}\sum_{n=1}^{\infty}\int R_{m,n}(J,J')\tilde{f}_n(J')dJ', \tag{5.12}$$

where Ω is the coherent frequency, f_m is the m-th azimuthal mode (m>0), I is the intensity and $\rho_H(J)$ is the Haissinski solution for the density. The kernel of EQ 5.12 is given by

$$R_{m,n}(J, J') \equiv -i\int\frac{Z(\xi)}{\xi}C_m(\xi, J)C_n^*(\xi, J')d\xi, \tag{5.13}$$

where $\xi \equiv \omega\sigma_0/c$ is the dimensionless frequency, $Z(\xi) \equiv cZ(\omega(\xi))/A$ is the normalized impedance,

$$C_m(\xi, J) \equiv \frac{1}{2\pi}\int e^{im\varphi + i\xi x(J, \varphi)}d\varphi, \tag{5.14}$$

and $x(J, \varphi)$ is a trajectory of a particle defined by the Haissinski Hamiltonian.

We will choose the initial phase of this trajectory so that the latter has cosine-like terms only

$$x(J, \varphi) = \sqrt{2J/\omega_0}\cos\varphi + \Phi(J, \cos n\varphi) . \tag{5.15}$$

Here n=0,1,2,... and Φ is some function, that, in principle, can be found by perturbation theory (see EQ B.18). Such a choice of the initial phase that cancels all the sine-like terms is always possible due to the mentioned earlier time reversibility of Hamiltonian systems.

For such a trajectory $x(J, \varphi) = x(J, -\varphi)$ and

$$C_m(-\xi, J) = C_m^*(\xi, J) . \tag{5.16}$$

To proceed with our derivation we first neglect the possibility of the second minimum in the potential well which gives $\frac{d\rho_H}{dJ} < 0$ for any J. Therefore, the dispersion relation EQ 5.12 can be transformed (as was pointed out in [42]) to a more symmetric form

$$\frac{\Omega}{m}g_m(J) = \omega(J)g_m(J) - I\sum_{n=1}^{\infty}\int\sqrt{\frac{d\rho_H}{dJ}\frac{d\rho'_H}{dJ'}}R_{m,n}(J, J')g_n(J')dJ', \tag{5.17}$$

where

$\rho'_H \equiv \rho_H(J')$ and $g_m(J) \equiv \tilde{f}_m(J) / \sqrt{\left|\frac{d\rho_H}{dJ}\right|}$.

EQ 5.17 is equivalent to the eigenvalue problem

$$\frac{\Omega}{m} h(J) = \int \left(\omega(J)\delta(J-J') - I\sqrt{\frac{d\rho_H}{dJ}\frac{d\rho'_H}{dJ'}}\tilde{R}(J, J') \right) h(J')dJ', \tag{5.18}$$

where

$$h(J) \equiv \begin{bmatrix} g_1(J) \\ g_2(J) \\ \dots \end{bmatrix}, \qquad \tilde{R}(J, J') \equiv \begin{bmatrix} R_{1,1}(J, J') & R_{1,2}(J, J') & \dots \\ R_{2,1}(J, J') & R_{2,2}(J, J') & \dots \\ \dots & \dots & \dots \end{bmatrix},$$ and $R_{m,n}$ are given by EQ 5.13.

The kernel of EQ 5.18 is symmetric with respect to $J \leftrightarrow J'$ interchange when

$$R_{m,n}(J, J') = R_{n,m}(J', J). \tag{5.19}$$

It is well known that an integral equation with a real and symmetric kernel allows only real eigenvalues. Therefore, when the condition EQ 5.19 holds true then all collective frequencies Ω in EQ 5.18 are real and there is no instability. Let us further investigate the meaning of this condition.

Recalling that $Z(-\xi) = Z^*(\xi)$ (EQ 2.38) and making use of EQ 5.16 we rewrite the definition of $R_{m,n}$ EQ 5.13 as

$$\begin{aligned} R_{m,n}(J, J') = {} & 2\int_0 \frac{1}{\xi} Im(Z(\xi)) Re(C_m(\xi, J)C_n^*(\xi, J'))d\xi \\ & +2\int_0 \frac{1}{\xi} Re(Z(\xi)) Im(C_m(\xi, J)C_n^*(\xi, J'))d\xi. \end{aligned} \tag{5.20}$$

This shows that $R_{m,n}$ is always real and that it can be represented as a sum of two distinct parts that are proportional to the imaginary and the real part of the impedance respectively.

To establish whether either of these two parts obeys the condition EQ 5.19 we note that by definition of C_m EQ 5.14

$$\begin{aligned} 4\pi^2 C_m(\xi, J)C_n^*(\xi, J') &= \iint \cos[m\varphi - n\varphi' + (x(J,\varphi) - x(J',\varphi'))\xi]\,d\varphi d\varphi' \\ &+ i\iint \sin[m\varphi - n\varphi' + (x(J,\varphi) - x(J',\varphi'))\xi]\,d\varphi d\varphi', \end{aligned} \tag{5.21}$$

which gives

$$\begin{aligned} Re(C_m(\xi, J)C_n^*(\xi, J')) &= Re(C_n(\xi, J')C_m^*(\xi, J)), \\ Im(C_m(\xi, J)C_n^*(\xi, J')) &= -Im(C_n(\xi, J')C_m^*(\xi, J)). \end{aligned} \tag{5.22}$$

Using these two equations and substituting EQ 5.20 into the stability condition EQ 5.19 we conclude that the latter generally does not hold because the second integral in EQ 5.20 (proportional to the real part of impedance) acquires an extra minus sign. However, when $Z(\xi)$ is imaginary EQ 5.19 does hold true which means that the kernel of EQ 5.18 is symmetric and instability cannot occur. In the opposite case of a real impedance the kernel is anti-symmetric. In this case there may or may not be an instability depending on the exact form of the kernel of EQ 5.18. Specifically, we may expect that the instability will occur when the frequency spread due to the variation of $\omega(J)$ (which makes up the diagonal of the kernel) is relatively small.

It is also useful to relate the above conclusions formulated in terms of impedance to the characteristics of single particle motion. From the consideration of the potential well distortion given in Section 4.1 of Chapter 2 we recall that imaginary part of impedance keeps the potential well symmetric with respect to the origin while the real part distorts the well asymmetrically. Therefore the conclusion above says that the instability is due to the asymmetry in the collective potential. Furthermore, when the potential well becomes asymmetric the particle trajectories expressed in term of J and φ (EQ 5.15) acquire even harmonics of phase. Therefore we expect that the onset of instability may be related to the relative strength of these even harmonics. This will be shown in detail in Section 2.3.

Finally, we note that the analysis above trivially applies to the case of a single azimuthal mode where the instability may only occur as a result of radial mode coupling. Therefore, our consideration shows that independent of whether instability shows up as radial or azimuthal mode coupling it always appears due to the asymmetry of the collective potential brought by the real part of the impedance. This justifies our instability classification suggested in Figure 8 of Chapter 2.

2.2 Discussion of the threshold criteria

As was shown above in the framework of the linearized Vlasov equation the longitudinal microwave instability is due to the asymmetry of the collective potential. On the other hand, many of the suggested criteria for the onset of instability are based on the dependence of incoherent particle frequency on action $\omega(J)$. It is easy to see now that such criteria are flawed and they may not work for all impedances.

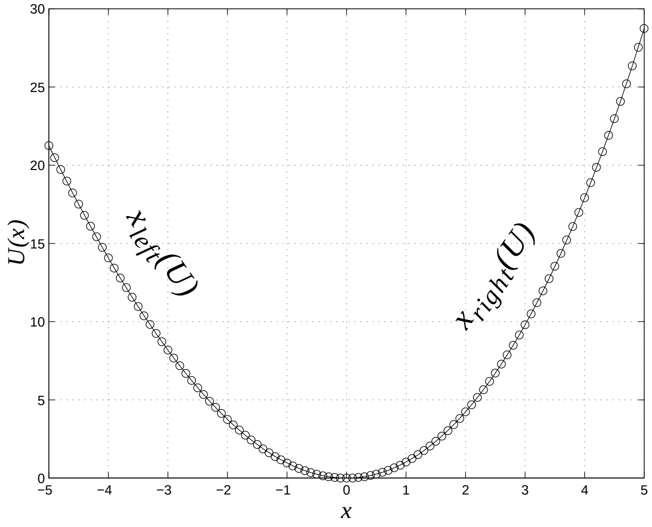

FIGURE 62. Illustration to EQ 5.23.

Indeed, generally $\omega(J)$ does not define the potential well. It only constrains the difference between $x_{right}(U)$ and $x_{left}(U)$ as [72]

$$x_{right}(U)-x_{left}(U) = \frac{1}{\pi\sqrt{2}}\int_0^U \frac{T(E)dE}{\sqrt{U-E}} = \sqrt{2}\int_0^{J(U)}\left(U-\int_0^J \omega(J')dJ'\right)^{-1/2} dJ\,, \tag{5.23}$$

where $T \equiv 2\pi/\omega$ is a period of oscillations, $J(U)$ is given by $\int_0^{J(U)} \omega(J')dJ' = U$ and $x_{left,right}(U)$ are the inverse functions of the potential $U(x)$ defined for the left and right halves of $U(x)$ respectively as illustrated in Figure 62.

Therefore, for any $\omega(J)$ there exists a corresponding symmetric potential, which according to Section 2.1 must be stable. For example, it is known that neglecting the radiation damping resistive impedance $Z(\omega)=R$ is unstable at any intensity [42]. We can easily find (numerically at least) a purely imaginary impedance that has exactly the same $\omega(J)$. As said above such an impedance leads to a symmetric potential well (see Figure 63) and hence causes no instability. Note, that the same argument can be applied against other instability onset criteria that are based on the behavior of $\omega(J)$.

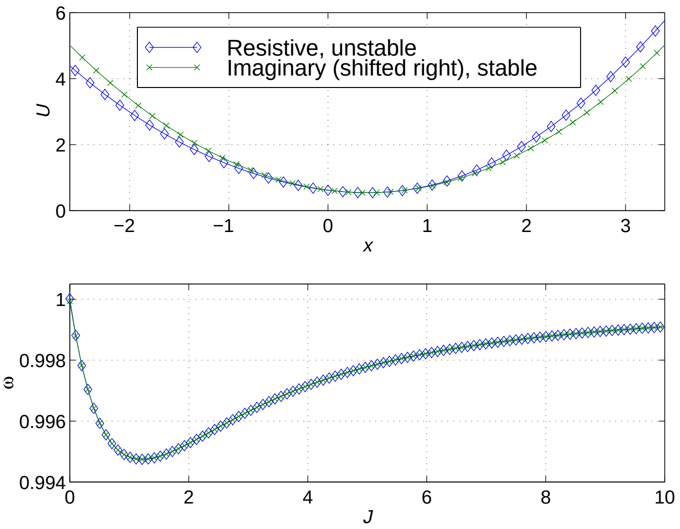

FIGURE 63. Collective potentials and incoherent frequencies for resistive impedance at intensity I_R=1 and for some imaginary impedance $Z(\omega)=iIm(Z(\omega))$.

Strictly speaking, the concept of a purely real or a purely imaginary impedance is not entirely accurate. If causality is assumed and $Z(\omega)$ is analytic in the upper half plane then the real and imaginary parts of impedance are related via the Hilbert transforms EQ 2.39 and EQ 2.40. Therefore, any imaginary part of $Z(\omega)$ causes some real part and vice versa. Nevertheless, our arguments regarding the stability remain valid because the Hilbert transforms relate only some integral measures of $Z(\omega)$ and allow flexibility choosing the impedance for a given $\omega(J)$. This impedance may be chosen so that $U(x)$ is almost symmetric and the beam is stable while a different choice could correspond to an instability. As shown earlier, what ultimately defines the stability is the degree of asymmetry of the kernel of EQ 5.18 which, of course, is not fixed by $\omega(J)$ dependence.

2.3 Analytical estimate of the threshold

The previous section is not too constructive since it does not tell us what the correct instability onset criterion should be. In our view a simple universal criterion for the onset of microwave instability does not exist. The steady-state solution is not enough to conclude about the stability. Instead, one has to deal with the linearized Vlasov equation dispersion relation. Fortunately, the latter allows some analytical treatment when the beam intensity is low. In this case it is possible to find the elements of $R_{m,n}$ and then estimate the upper limit of the instability growth rate. Given the radiation damping time this provides the lower bound of the instability threshold. The derivation is outlined below.

2.3.1 General idea

We will only consider the case of radial mode coupling i.e. only one azimuthal mode becoming unstable. This applies to the SLC damping rings close to the threshold. We should also note that while this case may not be entirely general there are computer simulations that show that the radial mode coupling tends to occur at lower intensity than the azimuthal mode coupling [42].

Intuitively this is rather clear because the azimuthal mode coupling should not occur when the incoherent frequency shifts are small which is usually the case at low intensities.

According to EQ 5.18 for a single azimuthal mode $g_m(J)$ the dispersion relation is given by

$$\frac{\Omega}{m} g_m(J) = \int\left(\omega(J)\delta(J-J') - I\sqrt{\frac{d\rho_H}{dJ}\frac{d\rho'_H}{dJ'}} R_{m,m}(J,J')\right) g_m(J')\,dJ', \tag{5.24}$$

where $R_{m,m}$ is defined by EQ 5.20 and has both symmetric and anti-symmetric parts given respectively by the first and second integrals in EQ 5.20.

On the other hand, according to Schur inequality (e.g. [74]) for any n-by-n matrix M with eigenvalues λ_i (i=1,2,...,n)

$$\sum_{i=1}^{n} \left|Im(\lambda_i)\right|^2 \le \sum_{i,j=1}^{n} \left|\frac{M_{i,j} - M_{j,i}}{2}\right|^2 \tag{5.25}$$

which relates imaginary parts of eigenvalues with anti-symmetric part of M.

Therefore, treating EQ 5.24 as an eigenvalue equation for an infinite matrix we get

$$\sum_{i=1}^{\infty} \left|Im(\Omega_i)\right|^2 \le 4I^2 m^2 \iint \frac{d\rho_H}{dJ}\frac{d\rho'_H}{dJ'}\left(\int_0 \frac{1}{\xi} Re(Z(\xi)) A_m(J,J',\xi)\,d\xi\right)^2 dJ\,dJ', \tag{5.26}$$

where

$$A_m(J,J',\xi) \equiv Im(C_m(\xi,J)C_m^*(\xi,J')). \tag{5.27}$$

In the simplest case when there is only one unstable radial mode with the growth rate γ the left hand side of EQ 5.25 equals $2\gamma^2$. In a general case of several unstable modes we can approximately write the left hand side as $2\gamma_{max}^2$ where γ_{max} is a growth rate of the most unstable mode.

Therefore, EQ 5.26 gives an estimate of the instability growth rate in terms of the Haissinski density ρ_H and some characteristics of single particle motion defined by the Haissinski Hamiltonian. In the next two sections we will show how one can approximately calculate the integrals in the right hand side of EQ 5.26 and estimate the instability growth rate and threshold.

2.3.2 Essential assumptions

First, we explicitly rewrite EQ 5.27 in terms of single particle trajectories. Separating odd and even harmonics of phase in these trajectories

$$x(J, \varphi) = x_o(J, \varphi) + x_e(J, \varphi), \tag{5.28}$$

and making use of EQ 5.14 we get by direct substitution that

$$\begin{aligned} &A_m(J, J', \xi) = \\ &\begin{cases} \int \frac{d\varphi}{2\pi} \cos(m\varphi)\cos(\xi x_o)\sin(\xi x_e) \int \frac{d\varphi'}{2\pi} \cos(m\varphi')\cos(\xi x_o')\cos(\xi x_e') \\ \int \frac{d\varphi}{2\pi} \cos(m\varphi)\sin(\xi x_o)\sin(\xi x_e) \int \frac{d\varphi'}{2\pi} \cos(m\varphi')\sin(\xi x_o')\cos(\xi x_e') \end{cases} \\ &\qquad - ((\varphi, x_o, x_e) \leftrightarrow (\varphi', x_o', x_e')) \ . \end{aligned} \tag{5.29}$$

In the last equation the first and the second lines in the right hand side apply to the cases of even and odd m respectively. The last line makes A_m anti-symmetric with respect to $J \leftrightarrow J'$ interchange.

For the subsequent calculations it is convenient to rewrite the trajectory in terms of amplitude and phase similar to EQ B.17. A_m expressed through these variables will be denoted as $\overline{A}_m$

$$\overline{A}_m(a, a', \xi) \equiv A_m(J(a), J(a'), \xi) . \tag{5.30}$$

We will assume in the further derivation that the higher harmonics of single particle motion are weak and can be considered as a perturbation of the fundamental. As evident from the trajectory written in terms of the amplitude EQ B.17 this assumption is valid when the amplitudes are small and the potential well is not too distorted from a parabolic shape (note that this does not have to be the low current parabolic shape). While there are always some beam particles with large amplitudes of synchrotron motion their number is generally small and should not affect the stability. This is evident directly from the dispersion relation EQ 5.24 that includes the derivatives of the Haissinski density that exponentially fall down at higher amplitudes. Therefore we can assume that the maximum amplitudes are not too large a_{max}~1. Whether the potential well distortion is small enough to consider the higher harmonics of single particle motion as a perturbation, depends, of course, on the intensity. Fortunately, for practically interesting intensities this is often valid. For example, if we calculate the Haissinski solution using the model SLC damping ring wake function $W^{\delta}_{DR}(x)$ (described in Section 1.2 of Chapter 3) and assume the beam population of N=10^{10} ppb, then the cubic term coefficient in the potential well (defined in EQ B.16) comes out to be $q_3 \approx 0.326$. Same calculation results in the value for the zero amplitude incoherent frequency $\omega_0 \equiv \omega(0)$ very close to 1, specifically $\omega_0 \approx 0.986$, which is expected for a fairly resistive vacuum chamber. Taking a=1 and substituting these values into EQ B.17 we get that the maximum amplitude of the second harmonic is less then 6% of the fundamental.

For the reasons above we will assume now that the intensity is low enough that we can use the following approximations.

1. Only the first two harmonic terms in particle trajectory matter for stability, which gives

$$\begin{aligned} x_o &= a\cos(\varphi)\ , \\ x_e &= \frac{q_3 a^2}{6\omega_0^2}(-3+\cos 2\varphi)\ . \end{aligned} \tag{5.31}$$

   We will also assume that typical x_e is small, so that $\sin(\xi x_e) = \xi x_e$ and $\cos(\xi x_e) = 1$. This is equivalent to saying that the impedance at frequencies much higher than the inverse beam size does not affect the stability.

2. To calculate the derivative of the Haissinski density in EQ 5.26 we can neglect higher order terms in the Hamiltonian assuming that $H_H(J) = \omega_0 J$. This is expected to hold well for low amplitude particles. Therefore, writing the density similar to EQ 2.64 $\rho_H(J) = (Z_H)^{-1} e^{-H_H(J)}$ we get approximately for the derivative

$$\frac{d\rho_H}{dJ} = -\frac{\omega_0}{Z_H} e^{-\omega_0 J} . \tag{5.32}$$

The value of the normalizing coefficient Z_H can be found from EQ B.6.

3. The relationship between the action and the amplitude is simply

$$J(a) = \omega_0 a^2/2 , \tag{5.33}$$

which neglects the terms of the order of $q_3^2 a^4 \omega_0^{-3}$, $q_4 a^4 \omega_0^{-1}$ and higher.

The approximations above allow calculation of integrals in EQ 5.26 when $Re(Z(\xi))$ is ξ-independent (resistive impedance). For general impedance we can still proceed replacing $Re(Z(\xi))$ with its upper bound

$$Re(Z(\xi)) \le 1 , \tag{5.34}$$

where, as usual, the scale factor is absorbed in our definition of intensity I (see EQ 2.46 and EQ B.13). Such a replacement is expected to make the threshold and growth rate estimates more conservative.

2.3.3 Growth rate and threshold calculations

We will illustrate the calculations for the quadrupole mode m=2 which is of interest for the SLC damping rings. Any other azimuthal mode may be treated similarly. Substituting beam trajectories EQ 5.31 into EQ 5.29 gives

$$\overline{A}_2(a, a', \xi) = \xi\frac{q_3 a'^2}{6\omega_0^2} J_2(a\xi)\left[\frac{1}{2}J_0(a'\xi) - 3J_2(a'\xi) + \frac{1}{2}J_4(a'\xi)\right] - (a' \leftrightarrow a). \quad (5.35)$$

We now see that due to EQ 5.34 the integral over ξ in EQ 5.26 is of the type $\int_0 J_\mu(ax)J_\nu(bx)dx$ which can be expressed through a Hypergeometric function (e.g. [74])

$$\int_0 J_\mu(ax)J_\nu(bx)dx = \frac{b^\nu a^{-\nu-1}\Gamma\left(\frac{\mu+\nu+1}{2}\right)}{\Gamma(\nu+1)\Gamma\left(\frac{\mu-\nu+1}{2}\right)} F_{\frac{\mu+\nu+1}{2}, \frac{\nu-\mu+1}{2}; \nu+1}\left(\frac{b^2}{a^2}\right). \quad (5.36)$$

This requires that $a>0$, $b>0$, $Re(\mu+\nu)>-1$, and $b<a$.

Assuming that the first term in the square brackets of EQ 5.35 dominates at small amplitudes we get that

$$\int_0 \overline{A}_2(a, a', \xi)\frac{d\xi}{\xi} = \xi\frac{q_3 a'^2}{12\omega_0^2} \times \begin{cases} \frac{1}{a}F_{\frac{3}{2}, -\frac{1}{2}; 1}\left(\left(\frac{a'}{a}\right)^2\right) & (a' < a) \\ -\frac{1}{8}F_{\frac{3}{2}, \frac{3}{2}; 3}\left(\left(\frac{a}{a'}\right)^2\right) & (a < a') \end{cases} - (a' \leftrightarrow a). \quad (5.37)$$

Now we change variables back from amplitudes to actions as given by EQ 5.33 and substitute the result into EQ 5.26. In addition, we substitute the derivatives of the Haissinski density given by EQ 5.32. To proceed further with EQ 5.26 we have to deal with the double integral over J and J'. One way to handle this integral is to switch to cylindrical coordinates r and θ so that $J = r\sin\theta$ and $J' = r\cos\theta$. In these coordinates the arguments of Hypergeometric functions depend only on θ and the integral over r can be easily calculated. The final result is then expressed in the form

$$\left(\frac{\gamma\omega_0^3 Z_H}{I q_3}\right)^2 \le \frac{2}{9}\Phi, \quad (5.38)$$

$$\Phi \equiv \int_0^1 \left(F_{\frac{3}{2},-\frac{1}{2};1}(p) + \frac{1}{8} F_{\frac{3}{2},\frac{3}{2};3}(p) \right)^2 \frac{p^2 dp}{(1+p)^3} \approx 0.024 , \tag{5.39}$$

where γ is the growth rate of the quadrupole mode, $p \equiv \tan\theta$ and the value in the right hand side of EQ 5.39 was calculated by numerical integration.

All the quantities in the left hand side of EQ 5.38 generally depend on I. At a given intensity the Haissinski solution defines q_3, ω_0, and Z_H, thus EQ 5.38 gives an estimate of the maximum growth rate γ. In addition, since in the linear approximation the instability develops when the growth rate exceeds the radiation damping rate γ_d then EQ 5.38 implicitly gives a lower bound on the instability threshold intensity I_{thrsh}

$$\gamma_d^2 \left(\frac{\omega_0^3 Z_H}{I q_3} \right)^2_{I = I_{thrsh}} \le \frac{2}{9} \Phi \quad . \tag{5.40}$$

For example, for resistive impedance with the Haissinski potential given by EQ 2.72 the frequency $\omega_0 = 1$ and (as can be checked by a direct Taylor expansion) $q_3 = \tanh(I/2)/\sqrt{2\pi}$. When substituted in EQ 5.38 this gives

$$\gamma < \frac{\sqrt{\Phi}}{12\pi^{3/2}} I^2 . \tag{5.41}$$

In this equation we neglected higher order terms of I and used $Z_H = 2\pi$.

Similarly, for the threshold intensity for the resistive impedance we get

$$I_{thrsh} > \sqrt{12\pi^{3/2}\Phi^{-1/2}\gamma_d} . \tag{5.42}$$

To estimate the threshold beam current for the SLC damping rings we use EQ 2.46 and take all the parameters needed including the value of γ_d (for positron ring, normalized to ω_{s0} at nominal RF voltage) from Table 1. Using the experimental value for the effective vacuum chamber resistance R_{eff}=1 kΩ (see Section 1.0 of Chapter 4) we get for the threshold $N_{thrsh} > 4 \times 10^9$ ppb which is a factor of four lower than the observation. Nevertheless we regard such agreement being quite reasonable considered the approximations we made above.

If a more accurate impedance model is available a better approach would be to numerically find the Haissinski solution and from it calculate q_3, ω_0, and Z_H. Repeating this at different intensity values gives the instability threshold according to EQ 5.40. We have done this calculation for the model wake function $W^{\delta}_{DR}(x)$ which, however, has resulted in the same threshold value of $N_{thrsh} > 4 \times 10^9$ ppb indicating once again that the model is fairly resistive.

The fact that the threshold estimates obtained are rather conservative is not surprising. Indeed, the equal sign in the Schur inequality EQ 5.25 holds only for anti-symmetric matrices with the diagonal elements all being zero while in our case (EQ 5.24) these are dominated by $\omega(J)$. In this sense our estimate does not include the stabilizing effect of the frequency spread as well a possible stabilizing contribution to $R_{m,m}$ due to the imaginary part of impedance. Another significant approximation is that in EQ 5.34 we replace the impedance with a constant upper bound. This may possibly be improved by using some frequency dependent limiting function that allows analytical integration of $\overline{A}_m$ similar to EQ 5.37. In spite of these limitations we believe that being able to bound the instability threshold based on the Haissinski solution as described above is quite useful and more accurate than relying on empirical criteria.

3.0 Summary of analytical results

In this chapter we have studied several aspects of beam dynamics related to the saw-tooth instability. In Section 1.0 we have looked at previously unexplained observations of asymmetry in the BPM signal spectra from unstable bunches. We have offered a possible explanation of this phenomenon that provided some fairly general insight into the physics of the nonlinear regime of the saw-tooth instability.

In Section 2.0 we have concentrated on the linear theory of microwave instability in the slow blowup regime. This regime, defined in Figure 8, applies to the initial growth period of the saw-tooth instability in the SLC damping rings. As a result, we have arrived at some general conclusions about the onset of the instability. First of all, we have shown that the incoherent frequency dependence on action alone does not define the stability of the system. This conclusion invalidates several empirical criteria for the onset of instability that are often cited in the literature. Second, we have shown that the instability appears due to the real part of the impedance which affects the single particle motion by inducing an asymmetry in the unperturbed potential well. It is interesting that this conclusion is rather general and it applies both to the cases of radial and azimuthal mode coupling.

Finally, towards the end of this chapter we have analytically estimated the lower bound for the threshold of microwave instability. Once again we considered a slow blowup regime and, in addition, we have concentrated on the quadrupole mode. In contrast to the previous results of this chapter this last one is not as general and is expected to provide a relatively tight lower bound only when a few radial modes become unstable, the impedance is relatively resistive and the incoherent frequency shifts are small. Fortunately, all of these is not uncommon in many newer storage rings.

Chapter 6

Summary and outlook

1.0 Experiment

In present thesis we have described our research of the saw-tooth instability in the Stanford Linear Collider damping rings. Our studies have been mostly experimental and continued through several SLC runs. To some extent we were fortunate that the instability was present during routine SLC operations that allowed for systematic studies of its properties either parasitically to the collisions or during the breakdowns in the SLC systems downstream of the damping rings. On the other hand, the ability of the SLC to run with the instability present has clearly indicated that the instability effect on the beam was rather small and its measurements would require sophisticated diagnostics.

Some of these diagnostics have been developed in the course of our studies. It included detectors for special processing of high frequency broad-band BPM signals coming from single bunches. These detectors proved to be useful by themselves, for example for driven response measurements, as well as in a combination with other beam diagnostics. Another example of original hardware developed for this thesis is the apparatus for precise synchronous phase measurement.

Of course, we have also used some commercially available hardware and the most sophisticated of that was the Hamamatsu FESCA-500 streak camera that is capable of resolving the longitudinal beam distribution with sub-picosecond accuracy. A great deal of effort went to adapt this device for our particular needs namely to study the longitudinal phase space of unstable beams.

One of the significant ideas there was to utilize a combined running of the streak camera and the instability signal detector that have conveniently complimented for the disadvantages each had for single beam longitudinal diagnostics. Another major step was to properly interface all the hardware including the streak camera to the SLC control system which provided the possibility of getting large amounts of data and allowed looking at rather small effects covered by a substantial noise component.

Having built the appropriate hardware we were able to carry out many experiments that gave us more understanding of the saw-tooth instability, the initial appearance of which in the new SLC vacuum chambers was a complete mystery. In particular, we were able to answer two important questions i) what exactly was the instability doing to the beam and ii) what was the effect of the instability on the SLC performance. Specifically, on the first question we have established that the instability was creating a quadrupole or a sextupole-like structure in the beam phase space. Moreover, we were able to quantitatively describe this structure in spite of the fact that it usually included only a few percent of beam particles. On the second question, by correlating the instability signal at extraction to the BPM readings downstream of the damping rings we have shown that the instability results in a significant pulse-to-pulse jitter in transverse beam trajectories. This effect is important for the SLC and even more so for the future linear colliders since the transverse jitter effectively decreases the luminosity.

We have also performed some experiments measuring either driven or self excited response of unstable beams. Some of the instability features we uncovered were quite surprising including bursting behavior, mode switching, peculiar shapes in the phase of the driven response to name a few. While some of these features are still not fully understood we have documented them with a hope of a better theoretical explanation yet to come.

Finally, we have also made an effort to characterize the impedance of the vacuum chamber which is crucial for a quantitative explanation of the instability phenomenon. We have performed a synchronous phase measurement that provided a loss factor estimate in agreement with the damping ring wake function model [50]. Using an alternative method, we have estimated some impedance parameters by fitting the low current streak camera beam profiles with a Haissinski solution. This again have agreed quite well with the wake function model.

There are, however, some experiments that we were unable to perform due to lack of hardware, machine time or other resources. Some of these include taking a movie of the instability development with fast dual sweep streak camera. Another one would be performing more detailed measurements of the driven beam response above the instability threshold that would include a bidirectional frequency sweep and possibly parallel streak camera data taking. A more practically oriented experiment would be an attempt to either damp or compensate the instability through some kind of a feedback system. An active element for such a system could be either a damping ring RF cavity [75] or a bunch compressor in the extraction line.

It is our hope that some of these experiments will be performed in future. And we also hope that the original hardware and techniques described in this thesis will be beneficial for some other experiments beyond the SLC.

2.0 Theory and simulations

Several analytical results regarding the instability have been also presented in this thesis. We have offered a possible explanation of the sideband asymmetry seen in the BPM signal spectra from unstable bunches. The idea of the asymmetry being due to the higher Fourier harmonics in particle trajectories is quite simple. However, it has remarkably provided us with a deeper insight on the physics of instability and its possible connection to the broken symmetry problem.

In a separate derivation we have looked at the instability threshold. Based on the linearized Vlasov equation analysis we have shown that many of the frequently mentioned criteria for the onset of instability are in fact flawed and they do not work for every impedance. We have offered an alternative method that (within limits of some approximations) gives a conservative lower bound for the threshold of the microwave instability.

Of course, our analytical results on the instability threshold have only briefly touched the linear theory of the phenomenon. And although there is still some confusion even within the linear theory it is our opinion that the real challenge is to understand the nonlinear aspects of the instability. For example, the questions like why the instability saturates, what defines the saturation level, what is the physics behind the bursting behavior or the mode switching still do not have definitive answers.

On the other hand, the problem is quite interesting and the research on this topic is continuing. There are better techniques today to simulate the instability by direct solving of the Fokker-Planck equation with a self-consistent potential. These techniques are starting to give a quantitative agreement with experiments [76], [77]. In addition, we now understand better how to properly simulate the instability using particle tracking [78], the method which when used during the vacuum chamber design stage has grossly overestimated the instability threshold. Finally, there are new ideas on how to qualitatively explain the physics of the nonlinear stages of the instability phenomenon based on simple models that involve only a few radial modes with tractable dynamics [79]. It is especially important that such methods calculate the instability saturation level and describe the final stage of the beam, the quantities that are the most relevant for practical design of a storage ring. In our opinion another beneficial work in the area of theory and simulations would be a detailed comparison of the results of the different algorithms that are now used to study single beam dynamics, namely numerical solutions of the Fokker-Planck equation, Vlasov equation based techniques, and direct particle tracking.

There is no doubt that such an understanding will come and further theoretical work will continue. Indeed, the problem of single bunch stability in electron rings is quite general and it easily connects to other important problems of beam physics and beyond. It is our hope that this thesis will serve as a useful reference point for future activities in this area.

Appendix A

Single and coupled bunch properties of instability

1.0 Single bunch properties

As it was mentioned many times throughout this thesis we have concluded that the instability is predominantly single bunch. This conclusion is based on the following experimental observations.

1. The instability occurs with either one or two bunches stored in the ring. The instability thresholds and mode frequencies in both cases are close.
2. Instability sidebands as seen by a spectrum analyzer do not alternate in magnitude from even to odd rotation harmonics.
3. Contrary to the single bunch instability signal, the signal derived from two bunches does not correlate with the bunch length or trajectory in the linac downstream.

In addition, there are no obvious mechanisms that would lead to non-trivial coupling between the bunches that significantly affects their internal structure. Damping rings have, of course, some long range wakefields that are mainly due to the RF and Π-mode cavities. However, the frequency contents of these wakes is much lower than the inverse bunch length $\omega_{high\text{-}Q} << c/\sigma$. There is another possible mechanism, specifically bunches interacting through the RF system. Yet, we have looked extensively and found no evidence of instability signals in many parts of the damping ring RF system.

Based on the arguments above we would not expect to see any coupling between the two unstable bunches stored simultaneously in the ring. However, having built diagnostics that separates the instability signals coming from the two bunches, we were tempted to check this experimentally. The results of these experiments were quite surprising, and they will be described in the next section.

2.0 Coupled bunch experiment

For this experiment we used the detector shown in Figure 26 except that we utilized both ports of the RF switch terminating them with identical detector-filter-amplifier circuits. For the most recent version of this experiment (February, 1998) the outputs of the amplifiers (rather two channels of one amplifier) were subsequently connected to the two channels of the Tektronix TDS 460A oscilloscope. The RF switch was gated with a 50% duty cycle gate with its timing adjusted as described in Section 5.3.3 of Chapter 3. In addition to checking with the spectrum analyzer that both ports produce single bunch signal we have also checked that the cross-talk in the amplifier was negligible. Due to the high memory depth of the TDS 460A oscilloscope we were able to record 120,000 point 12 ms long traces of the instability signals for both bunches. This, in turn, allowed comparison of both the envelopes and the relative phases of the instability signals from two bunches stored.

The experiment was performed in the positron ring at V_{RF}=790 kV (SCP readout). The total of 137 traces were recorded with the average current of N~2.5×10^{10} ppb and significant (13%) current jitter. The instability frequency was about 160 kHz.

Samples of the data obtained in this experiment are illustrated in Figure 64. Left and right halves of the figure represent two different injection cycles. The following explanation refers to either injection cycle. The top trace shows the instability signal for the bunch that gets extracted at t~11 ms (the second transient). The middle trace shows the instability signal for the other

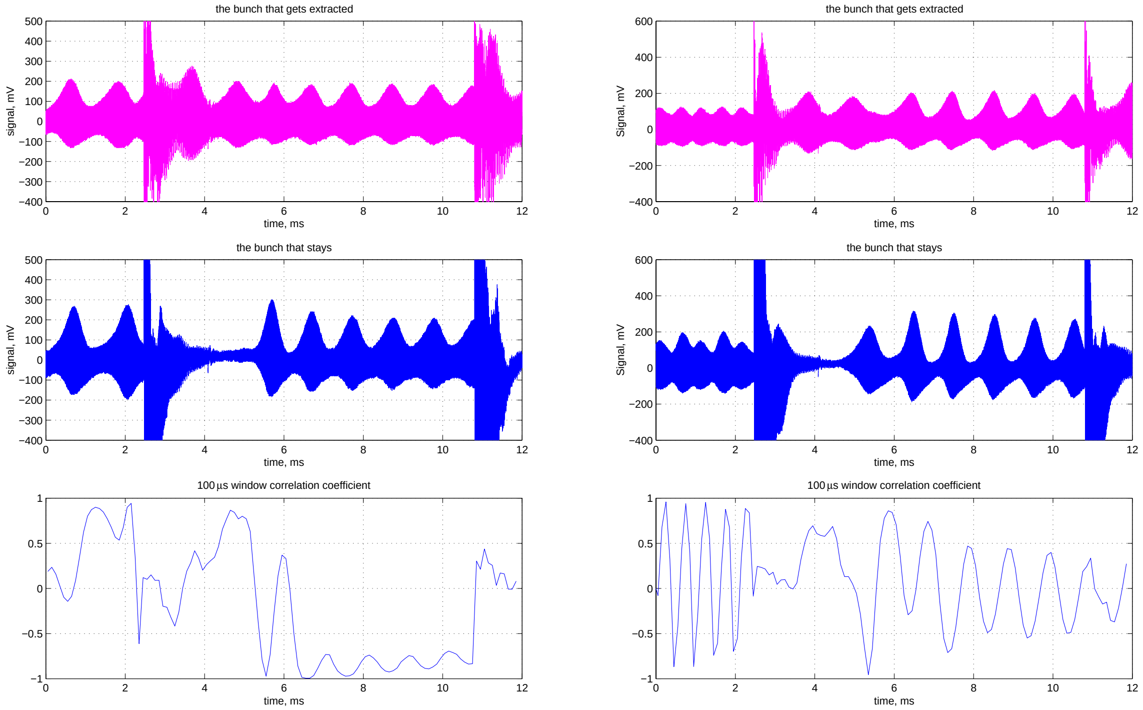

FIGURE 64. Data samples for the coupled bunch experiment.

bunch stored in the ring. That bunch was injected at *t*~2.2 ms (the first transient). In addition, the data shown on all the plots that occur before the first transient or after the second transient belong to previous and subsequent injection cycles respectively.

Several conclusions can be made from the data presented. First of all, the top traces for the two injection cycles seem to indicate that the occurrence of the bursts is not locked to the injection/extraction. Second, the comparison of the top and bottom traces for each store shows some correlation between the instability signal envelopes for the two bunches; they seem to burst at roughly the same time. Finally, to check how the instability signals of the two bunches relate to each other on a finer timescale, we have calculated the linear correlation coefficient between the two signals in a 100 µs sliding window. These correlation coefficients are shown on the bottom plots for both stores. There is a significant difference between the two injection cycles. For the left one the correlation coefficient is large and negative towards the end of the store indicating that the bunches are locked in phase and oscillate π out of phase. For the other store (shown to the right) the correlation coefficient is less significant and it varies between negative and positive values. In this case there is no fixed phase relationship between the bunches. The same is true for the portion of the previous injection cycle (data prior to the first transient on the middle trace in the right part of Figure 64). Note that in that case the envelope shapes are quite different. This is amazing since (due to the way the gate for the RF switch was derived) the signal in the beginning of the middle trace and the one in the center of the top trace correspond to the same bunch.

Of course, two stores do not permit making general conclusions. Looking at all of the stores recorded we have established that roughly one half of them had the envelopes of the two bunches correlated. The other half consisted of either uncorrelated but bursting envelopes or alternatively roughly constant amplitude ones. Within the first half about 60% of the stores had fixed phase relationship between the bunches on a finer timescale and the bunches were oscillating π out of phase. It is interesting that in many cases with no phase relationship between the bunches there was a fraction of a kHz to a few kHz instability frequency difference between the two bunches, presumably due to different charges. However, there were also stores with seemingly the same instability frequency for both bunches and yet they did not have any fine scale correlation.

We should note that the numbers above are approximate and they depend on the definition of correlation used. Furthermore, we have observed somewhat different behavior in the previous and less sophisticated version of this experiment (several hundred stores taken on July 96). For that batch of data there was no significant correlation between the envelopes. However, when the bursts happened to coincide the bunches oscillated mostly in phase, although there were a few cases with π phase shift too.

3.0 Summary

Available evidence about the cross-talk between the bunches is inconclusive. The reasons why the correlation is present in some cases and not in the others are unknown. Nevertheless we can definitely state the following. For significant portion of injection cycles we observed some coupling between the two unstable beams. It showed up in either or both correlated envelopes or the fixed phase relation between the instability signals.

Note, that this statement does not necessarily contradict the single bunch evidence from Section 1.0. Indeed, for example the spectrum analyzer sidebands are averaged over many injection cycles. Since only some of these cycles have the bunches at fixed phase relationship with respect to each other (during some fraction of the store) the alternating sideband pattern washes out. Even simpler consideration applies to the linac correlation experiment. The strongest argument in favor of a single bunch phenomenon is the one about the thresholds being close. But examining our coupled bunch evidence closely we find that all the conclusions about the cross-talk apply when the instability is fully developed. There seems to be little or no cross-talk for the lower current stores when the instability is not bursting. In addition, due to the noise floor of our diagnostics we cannot say whether bunches are related in phase when one of them is just becoming unstable. If they are unrelated than it is not surprising that the threshold depends on the single bunch rather than the total current stored.

To conclude, we believe that the instability is fairly complex especially in its nonlinear stages. Our experimental evidence indicates that the instability is predominantly single bunch, but there is some weak coupling between the bunches that often shows up when the instability is fully developed. At this point the cause of this coupling is unclear but we believe that it is most likely due to some subtle feedback mechanism through the RF system.

Appendix B

Linearized Vlasov equation dispersion relation

In this Appendix we derive the linearized Vlasov equation dispersion relation. In our derivation we mainly follow [47]. For clarity we will consider the stability of the Haissinski solution with the density $\rho_H \equiv \int f_H(x', p')dp'$ which we assume to be normalized to 1. Other distribution functions can be treated similarly. We start with the Vlasov equation in the form

$$\frac{\partial f}{\partial \tau} + \{H(x, p, f), f\} = 0, \tag{B.1}$$

where the Hamiltonian is defined by

$$H(x, p, f) = \frac{p^2}{2} + \frac{x^2}{2} + U_W(x, f) \tag{B.2}$$

and the variables are normalized as given by EQ 2.15.

Wake-related contribution to the potential well is

$$U_W(x, f) = I\int_x dx' S(x - x')\int dp' f(x', p', \tau), \tag{B.3}$$

where I is the intensity and $S(x)$ is the integrated wake defined by EQ 2.30, EQ 2.46 and EQ 2.47.

A distribution function is represented in the form $f = f_H + f_1$, where the perturbation is considered small $f_1 << f_H$. Substituting this into EQ B.1 gives the linearized Vlasov equation

$$\frac{\partial f_1}{\partial \tau} + \{H(x,p,f_H), f_1\} + \{H(x,p,f_1), f_H\} = 0 \tag{B.4}$$

where the Hamiltonians are defined by EQ B.2 and EQ B.3.

Switching to action-angle variables J and φ defined so that the Hamiltonian of the Haissinski solution depends only on action $H_H(x, p, f_H) \equiv H_H(J)$ gives the linearized Vlasov equation in the following form

$$\frac{\partial f_1}{\partial \tau} + \omega(J)\frac{\partial f_1}{\partial \varphi} = \frac{d\rho_H}{dJ}\frac{\partial}{\partial \varphi}U_W(x(J,\varphi), f_1). \tag{B.5}$$

In this equation $\omega(J) \equiv \frac{dH_H}{dJ}$ and, as always, $\dot{\varphi} \equiv \omega(J)$. Note, that in new canonical variables the density ρ_H is still normalized to 1

$$\int \rho_H(J)\, d\varphi\, dJ = 2\pi \int \rho_H(J)\, dJ = 1. \tag{B.6}$$

Looking for harmonically varying solutions of EQ B.5

$$f_1(J,\varphi,\tau) = \sum_m \tilde{f}_m(J) e^{i\Omega\tau - im\varphi} \tag{B.7}$$

and introducing Fourier transform of U_W

$$\tilde{U}_m(J) \equiv \frac{1}{2\pi}\int e^{im\varphi - i\Omega\tau} U_W(x(J,\varphi), f_1(J,\varphi,\tau))\, d\varphi \tag{B.8}$$

we obtain the following relation

$$(\omega(J) - \Omega/m)\tilde{f}_m(J) = \frac{d\rho_H}{dJ}\tilde{U}_m(J). \tag{B.9}$$

Due to EQ B.7 and EQ B.8 the right hand side of EQ B.9 couples all the azimuthal modes together. An infinite system of equations EQ B.9 written for every azimuthal mode constitutes the dispersion relation of the linearized Vlasov equation. As mentioned in Section 5.2.2 of Chapter 2 there are detailed algorithms for truncation and approximate numerical solution of this system (see [38], [41]).

We should note that deriving EQ B.9 we neglected the $m=0$ monopole mode which is usually done in standard Vlasov equation analysis. The physics and potential single bunch instability associated with the monopole mode is covered in [73].

One of the difficulties of dealing with the dispersion relation above is that finding $\tilde{U}_m$ requires calculating double integrals of the type $\int e^{im(\varphi-\varphi')}S(x(J,\varphi)-x(J,\varphi'))d\varphi d\varphi'$ (see EQ B.3). Such integration is difficult to perform numerically let alone to evaluate analytically. To get around this we integrate EQ 2.36 to get the following relation between the integrated wake and impedance (that we have also seen used in [52])

$$S(x) = -\frac{c}{2\pi iA}\int\frac{Z(\omega)}{\omega}e^{i\omega x\sigma_0/c}d\omega, \tag{B.10}$$

where the factor A in the denominator comes from our normalization of integrated wake EQ 2.47. This assumes that the integrand does not have a pole at zero which is consistent with EQ 2.41 and EQ 2.42. Due to the exponential dependence on x EQ B.10 allows factorization of those double integrals in $\tilde{U}_m$.

After some manipulations we can write the dispersion relation of the linearized Vlasov equation in the form

$$\frac{\Omega}{m}\tilde{f}_m(J) = \omega(J)\tilde{f}_m(J) + I\frac{d\rho_H}{dJ}\sum_{n=1}^{\infty}\int R_{m,n}(J,J')\tilde{f}_n(J')dJ', \quad m = 1, 2, \ldots. \tag{B.11}$$

The kernel $R_{m,n}$ is given by

$$R_{m,n}(J,J') \equiv -i\int\frac{Z(\xi)}{\xi}C_m(\xi,J)C_n^*(\xi,J')d\xi, \tag{B.12}$$

where the normalized impedance

$$Z(\xi) \equiv cZ(\omega(\xi))/A \tag{B.13}$$

is defined in terms of dimensionless frequency

$$\xi \equiv \omega\sigma_0/c, \tag{B.14}$$

and the factors C_m are defined by

$$C_m(\xi, J) \equiv \frac{1}{2\pi}\int e^{im\varphi + i\xi x(J,\varphi)} d\varphi . \tag{B.15}$$

Finally, as noted in [47], once the Haissinski solution is found the trajectory *x(J,φ)* (which can be also thought of as a canonical transformation) can be calculated by perturbation theory. Subsequently the coefficients C_m are found analytically provided that the higher harmonics of trajectories are small. Specifically, representing the collective potential as a series

$$U_H(x) = \frac{\omega_0^2 x^2}{2} + \sum_{n=3}^{\infty} \frac{q_n x^n}{n}, \tag{B.16}$$

where $\omega_0 \equiv \omega(0)$ the trajectory can be written in terms of amplitude a and phase (e.g. [72])

$$x(a, \varphi) = a\cos\varphi + \frac{q_3 a^2}{6\omega_0^2}(-3 + \cos 2\varphi) + O(a^3), \tag{B.17}$$

or, equivalently, in terms of J and φ

$$x(J, \varphi) = \sqrt{\frac{2J}{\omega_0}}\cos\varphi + \frac{q_3}{\omega_0^3}\left(-1 + \frac{1}{3}\cos 2\varphi\right)J + O(J^{3/2}). \tag{B.18}$$

Note, that x is now defined with respect to the intensity dependent minimum of the potential well rather than the center of the RF bucket.

It is clear that substituting this trajectory EQ B.18 into EQ B.15 and Taylor expanding with respect to the terms containing q_3 allows writing C_m as a sum of Bessel functions with the argument $\xi\sqrt{2J/\omega_0}$.

Bibliography

[1] M. Sands, "The Physics of Electron Storage Rings: an Introduction", SLAC-0121, 1970.

[2] H. Bruck, "Accélérateurs Circulaires des Particules", Presses Universitaires de France, Paris, 1966. Also in Los Alamos Report, LA-TR-72-10 (English translation).

[3] A. Chao, "Physics of Collective Beam Instabilities in High Energy Accelerators", Wiley, 1993.

[4] H. Wiedemann, "Particle Accelerator Physics I: Basic Principles and Linear Beam Dynamics", 2nd ed., Springer-Verlag, 1998.
H. Wiedemann, "Particle Accelerator Physics II: Nonlinear and Higher Order Beam Dynamics", Springer-Verlag, 1995.

[5] J. Seeman, Talk given at the SLAC Beam-Beam Interaction Workshop, 1998.
S. Heifets and G. Sabbi, "Single Bunch Stability in LER of PEP-II", SLAC-AP-104, 1996.

[6] R. Holtzapple, "Longitudinal Dynamics at the Stanford Linear Collider", Ph.D. Thesis, Stanford University, 1996. Also in SLAC-Report-487, 1996.

[7] SLC Design Handbook, SLAC, 1984.

[8] N. Phinney et al, "The SLC", Manuscript in preparation, 1999.

[9] T. Limberg et al, "Calculations of Emittance and Damping Time Effects in the SLC Damping Rings", Proceedings of EPAC-92, 682, 1992. Also in SLAC-PUB-5789, 1992.

[10] M. Minty and R. Siemann, "Heavy Beam Loading in Storage Ring Radio Frequency Systems", Nucl. Instrum. and Meth. 376, 301, 1996.

[11] R. Siemann, "Bunched Beam Diagnostics", Batavia 1987/Ithaca 1988, Proceedings, Physics of Particle Accelerators, 430, 1987.

[12] F. Caspers, "Instrumentation - Pick-ups and Diagnostics", Proceedings of the 1994 Joint US-CERN-Japan International School, World Scientific, 460, 1996.

[13] M. Minty et al, "Using a Fast Gated Camera for Measurements of Transverse Beam Distributions and Damping Times", Proceedings of Berkeley 1992 Accelerator Workshop, 158, 1992. Also in SLAC-PUB-5993, 1992.

[14] M. Ross et al, "Wire Scanners for Beam Size and Emittance Measurements at the SLC", Proceedings of PAC-91, 1201, 1991. Also in SLAC-PUB-5556, 1991.

[15] Hamamatsu Photonics, Hamamatsu Instruction Manuals for 1) Streak Camera C3735l, 2) Input Optics A1974 3) Cooled CCD Camera C3640-60/61, 1994.

[16] L. Landau and E. Lifshitz, "The Classical Theory of Fields", Pergamon Press, 1979. (Course of Theoretical Physics, v. 2.)

[17] B. Zotter and S. Kheifets, "Impedances and Wakes in High Energy Particle Accelerators", World Scientific, 1997.

[18] K. Bane and M. Sands, "The Short-Range Resistive Wall Wake Fields", in Micro-Bunches Workshop at BNL, 131, 1995.

[19] T. Weiland, "On the Computation of Electromagnetic Fields Excited by Relativistic Bunches of Charged Particles in Accelerating Structures", CERN/ISR-TH/80-07, 1980.

[20] Yu. Klimontovich, "The Statistical Theory of Non-equilibrium Processes in a Plasma", Cambridge, Mass., M.I.T. Press, 1967.

[21] A. Akhiezer and S. Peletminskii, "Methods of Statistical Physics", 1st ed., Pergamon Press, 1981.

[22] A. Vlasov, "On the Kinetic Theory of an Assembly of Particles with Collective Interaction", J. Phys. USSR, 9, 25, 1945.

[23] H. Risken, "The Fokker - Planck Equation: Methods of Solution and Applications", 2nd ed., Springer-Verlag, 1996.

[24] J. Haissinski, "Exact Longitudinal Equilibrium Distribution of Stored Electrons in the Presence of Self-Fields", Nuovo Cimento 18B, 72, 1973.

[25] F. Chen, "Introduction to Plasma Physics and Controlled Fusion", Plenum Press, 1984.

[26] N. Dikanskii and D. Pestrikov, "The Physics of Intense Beams and Storage Rings", Amer. Inst. Phys., 1994.

[27] F. Sacherer, "Bunch Lengthening and Microwave Instability.", CERN-PS-BR-77-5, 1977. Also in IEEE Trans. Nucl. Sci. 24, 1393, 1977.

[28] A. Ruggiero, "Theory of Longitudinal Instability for Bunched Electron and Proton Beams", IEEE Trans. Nucl. Sci. 24, 1205, 1977.

[29] K. Bane et al, "Bunch Length and Impedance Measurements in SPEAR", Proceedings of EPAC-88, 0878, 1988. Also in SLAC-PUB-4620, 1988.

[30] B. Zotter, "Short is Beautiful", Proceedings of the 4th Advanced ICFA Beam Dynamics Workshop, 1, 1990. Also in KEK Report 90-121, 1990.

[31] P. Krejcik et al, "High Intensity Bunch Length Instabilities in the SLC Damping Rings", Proceedings of PAC-93, 3240, 1993.

[32] K. Bane and K. Oide, "Simulations of the Longitudinal Instability in the SLC Damping Rings", Proceedings of PAC-93, 3339, 1993. Also in SLAC-PUB-6216, 1993.

[33] K. Bane et al, "High Intensity Single Bunch Instability Behavior in the New SLC Damping Ring Vacuum Chamber", Proceedings of PAC-95, 3109, 1995.

[34] D. Boussard, CERN Div Report MPS/DL-75/5, 1975.

[35] E. Keil and W. Schnell, CERN/ISR Div Report 69-48, 1969.

[36] S. Krinsky and J. Wang, "Longitudinal Instabilities of Bunched Beams Subject to a Non-Harmonic RF Potential", Part.Accel.17, 109, 1985.

[37] S. Zhang, "Microwave Instability Thresholds", Proceedings PAC-97, 1584, 1997.

[38] K. Oide and K. Yokoya, "Longitudinal Single Bunch Instability in Electron Storage Rings", KEK-Report-90-10, 1990.

[39] G. Besnier, "Contribution à la Théorie de la Stabilité des Oscillations Longitudinales d'un Faisceau Accelère en Régime de Charge d'Espace", Ph.D. thesis, Université de Rennes, France, 1978.

[40] This criterion by P. Wilson is mentioned in K. Bane and K. Oide, "Simulations of the Longitudinal Instability in the SLC Damping Rings", Proceedings of PAC-93, 3339, 1993.

[41] M. D'yachkov and R. Baartman, "Method for Finding Bunched Beam Instability Thresholds", Proceedings of EPAC-94, 1075, 1994.
M. D'yachkov, "Longitudinal Instabilities of Bunched Beams Caused by Short-Range Wake Fields", Ph.D. thesis, The University of British Columbia, 1995.

[42] K. Oide, "A Mechanism of Longitudinal Single Bunch Instability in Storage Rings", KEK-Report-94-138, 1994. Also in Part. Accel. 51, 43, 1995.

[43] A. Galeev and R. Sagdeev, "Wave-Particle Interaction", Basic Plasma Physics Selected Chapters, North-Holland, 389, 1989.

[44] R. Meller, "Thermodynamic Mechanism for Bunch Lengthening", Proceedings of PAC-87, 1155, 1987.
R. Meller, "Statistical Method for Nonequilibrium Systems with Application to Accelerator Beam Dynamics", Ph.D. thesis, Cornell University, 1986.

[45] J. Schonfeld, "Theories of Statistical Equilibrium in Electron - Positron Colliding Beam Storage Rings", Ann. Phys. 160, 149, 1985.

[46] Y. Chin and K. Yokoya, "Analytical Approach to the Overshoot Phenomenon for a Coasting Beam in Particle Accelerators", Phys. Rev. D 28, 2141, 1983

[47] S. Heifets, "Microwave Instability Beyond Threshold", Phys. Rev. E 54, 2889, 1996.

[48] G. Stupakov, B. Breizman and M. Pekker, "Nonlinear Dynamics of Microwave Instability in Accelerators", Phys. Rev. E 55, 5976, 1997.

[49] R. Baartman and M. D'yachkov, "Simulations of Sawtooth Instability", Proceedings of PAC-95, 3119, 1995.

[50] K. Bane and K. Oide, "Simulations of the Longitudinal Instability in the New SLC Damping Rings", Proceedings of PAC-95, 3105, 1995.

[51] K. Bane and C. Ng, "Impedance Calculations for the Improved SLC Damping Rings", Proceedings of PAC-93, 3432, 1993. Also in SLAC-PUB-6254, 1993.

[52] S. Fang et al, "Microwave Instabilities in Electron Rings with Negative Momentum Compaction Factor", KEK-Report-94-190, 1994.

[53] L. Hendrickson, N. Phinney and L. Sanchez-Chopiteal, "Correlation Plot Facility in the SLC Control System", Proceedings of PAC-91, 1317, 1991. Also in SLAC-PUB-5685, 1991.

[54] N. Phinney and H. Shoaee, "The SLC Control System: Status and Development", Proceedings of PAC-87, 0789, 1987. Also in SLAC-PUB-4215, 1987.

[55] Learning this technique I have benefited from discussions and help by C. Adolphsen, T. Dean, A. Gromme, D. McCormick, M. Seidel and G. White.

[56] B. Podobedov and R. Siemann, "New Apparatus for Precise Synchronous Phase Shift Measurements in Storage Rings", Phys. Rev. ST Accel. and Beams 1, 072801, 1998.

[57] L. Rivkin et al, "Accelerator Physics Measurements at the Damping Ring", IEEE Trans. Nucl. Sci. NS-32, No 5, 2626, 1985. Also in SLAC-PUB-3690, 1985.

[58] M. Allen et al, "Beam Energy Loss to Parasitic Modes in SPEAR II", Proceedings of the Ninth International Conference on High Energy Accelerators, 352, 1975. Also in SLAC-PUB-1571, 1975.

[59] W. Anders, P. Kuske, and T. Westphall, "The Longitudinal Impedance of BESSY Determinated by Measurements of the Synchronous Phase Shift", Proceedings of High energy accelerators, Hamburg, v. 2, 1121, 1992.

[60] Hewlett-Packard, HP 8508A Vector Voltmeter Operating and Service Manual, 1988.

[61] R. Siemann, "W-Band Vector Network Analyzer Based on an Audio Lock-in Amplifier", SLAC-PUB-7884, 1998.

[62] M. Minty and F. Zimmerman, "Longitudinal Beam Transfer Function Measurements at the SLC Damping Rings", Proceedings of PAC-97, 1741, 1997.
F. Zimmerman and M. Minty, "Measurements of Single-Bunch Longitudinal Beam Transfer Functions in the SLC Damping Rings", SLAC-CN-412, 1996.

[63] J. Byrd, W. Cheng and F. Zimmermann, "Nonlinear Effects of Phase Modulation in an Electron Storage Ring", Phys. Rev. E 57, 4706, 1998.

[64] B. Podobedov and R. Siemann, "Signals from Microwave Unstable Beams in the SLC Damping Rings", Proceedings of PAC-99, 146, 1999.

[65] B. Podobedov and R. Siemann, "Saw-Tooth Instability Studies in the Stanford Linear Collider Damping Rings", Proceedings of PAC-97, 1629, 1997.

[66] R. Holtzapple et al, "Single Bunch Longitudinal Measurements at the Cornell Electron-Positron Storage Ring", CBN 98-23, Cornell, 1998.

[67] E. Babenko et al, "Length Monitor for 1-mm SLC Bunches", Proceedings PAC-93, 2423, 1993.

[68] R. Assmann and F. Zimmermann, "Possible Sources of Pulse-to-Pulse Orbit Variation in the SLAC Linac", Proceedings of 18th International Linac Conference (Linac 96), 473, 1996.

[69] F.-J. Decker et al, "Higher Order Beam Jitter in the SLC Linac", Proceedings of 18th International Linac Conference (Linac 96), 143, 1996.

[70] The NLC Design Group, "Zeroth-Order Design Report for the Next Linear Collider", SLAC-Report-474, 1996.

[71] D. McCormick, private communication, 1998.

[72] L. Landau and E. Lifshitz, "Mechanics", 3rd ed., Pergamon Press, 1976. (Course of theoretical physics, v. 1.)

[73] S. Heifets and B. Podobedov, "Single Bunch Stability to Monopole Excitation", Phys. Rev. ST Accel. and Beams 2, 044402, 1999.

[74] I. Gradshteyn and I. Ryzhik, "Table of Integrals, Series, and Products", 5th ed., Academic Press, 1994.

[75] A simple form of compensation for the instability (the so-called premuncher) was proposed by M. Minty and is briefly described in [69]. What we have in mind is something similar to our BTF measurement setup, where the phase of the pickup is inverted and fed back into the RF system. Another way would be to sample the instability signal before extraction and feedforward onto the bunch compressor.

[76] A. Novokhatski, Proceedings ICAP-98, 1998.
A. Novokhatski, private communication, 1999.

[77] R. Warnock, manuscript in preparation, 1999.

[78] K. Bane, private communication, 1999.

[79] S. Heifets, "Non-linear Mode Coupling and Saw-Tooth Instability”, To be published in Proceedings of Workshop on Instabilities at High Intensity Hadron Beams in Rings, Brookhaven, 1999.